

Improving the resolution of ground-based telescopes

Michael C. Roggemann

*Department of Engineering Physics, Graduate School of Engineering,
Air Force Institute of Technology, Wright-Patterson AFB, Ohio 45433-7765*

Byron M. Welsh

*Department of Electrical and Computer Engineering, Graduate School of Engineering,
Air Force Institute of Technology, Wright-Patterson AFB, Ohio 45433-7765*

Robert Q. Fugate

*Starfire Optical Range, US Air Force Phillips Laboratory, Kirtland Air Force Base,
New Mexico 87117*

Atmospheric turbulence profoundly limits the angular resolution of astronomical telescopes working at visible and near-infrared wavelengths. In fact, the angular resolution for conventional imaging through turbulence is on the order of 5–20 % of the diffraction-limited resolution at the best observatories in the world. The origin of these performance degradations is random turbulence-induced fluctuations in the index of refraction of the atmosphere. Random index-of-refraction fluctuations producing the optical path length of the atmosphere to be random in both space and time, producing random aberrations in the telescope pupil that degrade imaging performance. Over the past several years significant advances have been made in developing both hardware and image-processing-based techniques for improving the resolution of astronomical telescopes. Hardware-oriented correction techniques are based on wave-front sensing and adaptive optics. Image-processing-based methods include speckle-imaging techniques and hybrid imaging techniques that use elements of adaptive-optics systems and image reconstruction. Analysis techniques for predicting the performance of these imaging methods have been developed, and the comparative performance of these imaging techniques has been examined. This paper discusses turbulence and image-detection statistics, describes the fundamentals of methods for overcoming turbulence effects, and provides representative performance results. [S0034-6861(97)00102-5]

CONTENTS

		of the deformable mirror, and finite system temporal response	458
	B.	Adaptive optical system components	459
	1.	Deformable mirrors	460
	a.	Segmented and continuous deformable mirrors	460
	b.	Influence functions and modeling	460
	c.	Tilt-compensation mirrors	461
	2.	Wave-front sensors	461
	a.	The Hartmann wave-front sensor	461
	b.	The shearing interferometer	462
	c.	Curvature sensing	463
	3.	Controllers	464
	a.	Maximum <i>a posteriori</i> controller	465
	b.	Least-squares controller	465
	c.	Minimum-variance controller	465
	4.	Bandwidth requirements	466
	a.	Tilt compensation	466
	b.	Higher-order compensation	466
	C.	Adaptive optical imaging system performance	466
	1.	Mean-square residual phase error $\langle \epsilon^2 \rangle$	467
	2.	Average optical transfer function and point-spread function	468
	D.	Example of an adaptive optical imaging system	469
	1.	Optics	469
	2.	Full-aperture tilt control	470
	3.	Deformable mirror	470
	4.	Laser injection and wave-front sensors	471
	5.	Data-processing algorithms	472
	6.	Electronics	473
	7.	Scientific and engineering cameras	473
	8.	Examples of engineering data	473
I.	Introduction		438
II.	Statistical Preliminaries		440
A.	Statistics of index-of-refraction fluctuations		441
B.	Wave propagation through random media		444
1.	Derivation of the pupil-field spatial correlation function		445
a.	Plane-wave propagation		445
b.	Spherical-wave propagation		446
2.	Temporal and anisoplanatic effects		446
a.	Temporal effects on the pupil-field correlation function		447
b.	Anisoplanatic effects on the pupil-field correlation function		448
C.	Imaging performance		448
1.	Thin-screen turbulence model		448
2.	Long-exposure imaging		449
3.	Long-exposure atmospheric transfer function		449
4.	Short-exposure imaging		450
D.	Image-detection models		451
1.	Poisson random processes and image estimation		452
2.	Spatial-frequency-domain signal-to-noise ratio		453
3.	Doubly stochastic Poisson random processes		454
III.	Adaptive Optical Imaging Systems		454
A.	Factors that degrade adaptive optical imaging system performance		455
1.	Wave-front sensor light levels and anisoplanatism		456
2.	Finite pupil sampling of the wave-front sensor, limited number of degrees of freedom		

9. Scientific images	475
IV. Speckle Imaging	477
A. Overview of speckle imaging	477
B. Speckle interferometry	479
1. Speckle transfer function	479
2. Signal-to-noise-ratio considerations	479
C. Fourier phase estimation techniques	481
1. Knox-Thompson, or cross-spectrum, technique	482
a. Unbiased estimator for the cross spectrum	482
b. Cross-spectrum transfer function	482
c. Phase-spectrum reconstruction from the cross spectrum	484
2. Bispectrum technique	484
a. Unbiased estimator for the bispectrum	485
b. Phase-spectrum reconstruction from the bispectrum	485
D. Image reconstruction for speckle imaging	486
E. Conclusion	487
V. Deconvolution from Wave Front Sensing	487
A. DWFS estimators	489
B. Evaluation of the DWFS transfer function	489
C. Signal-to-noise-ratio considerations	490
VI. Deconvolution of Compensated Images	492
VII. Compensated Speckle Imaging	499
VIII. Conclusion	499
References	501

I. INTRODUCTION

Atmospheric turbulence profoundly limits the angular resolution of conventional ground-based astronomical imaging systems (Roddier, 1981; Goodman, 1985; Aleksoff *et al.*, 1993; Beckers, 1993). The physical origin of the optical effects of atmospheric turbulence is random index-of-refraction fluctuations in the atmosphere. Since the index-of-refraction of air is highly sensitive to temperature, the random distribution of air temperatures gives rise to a random index-of-refraction distribution in the atmosphere. The energy source for turbulent air motion is differential heating of the surface of the earth by the sun. Large pockets of air warmed by the sun and the surface of the earth are continually and randomly dissipated into ever smaller pockets of air, each having a unique temperature. These small pockets of air are commonly referred to as *turbulent eddies*. Random index-of-refraction variations cause the optical path length of the atmosphere to be random in both space and time. As a consequence of the random optical path length, a plane wave entering the atmosphere from a distant source, such as a star, is corrupted by propagation through the atmosphere. The surface of constant phase is no longer planar when the light is intercepted by a telescope. The nonplanar nature of the wave entering the telescope is physically manifested as an optical aberration that degrades the performance of the telescope.

A useful parameter for characterizing the effect of turbulence on the resolution of conventional imaging systems is the so-called Fried parameter r_0 (Fried, 1966b). The Fried parameter describes the telescope diameter for which nearly diffraction-limited resolution is

obtained using conventional imaging through the atmosphere. The term *conventional imaging* is used here to describe the case in which an image measurement is made using exposure times that are long compared to the rate of change of the turbulence, and no effort is made to compensate for turbulence effects. The angular resolution of a telescope with diameter D , where $D \gg r_0$, that is looking through the atmosphere, is approximately given by λ/r_0 , while the diffraction-limited resolution of the telescope is approximately λ/D . The latest generation of astronomical telescopes have diameters ranging from 4 to 8 m, while at visible wavelengths r_0 ranges from 10 to 20 cm at the best observatories. Thus the resolution of astronomical telescopes is greatly reduced by atmospheric turbulence. Note that the light-gathering capability of large telescopes is not significantly affected by turbulence. Hence, 4- to 8-m-diameter telescopes are able to see very dim objects in the conventional imaging paradigm, but the resolution achieved could be obtained from much smaller, r_0 -sized telescopes. These realizations have provided the motivation for the large body of research on techniques for overcoming turbulence effects.

Examples of the profound effects that turbulence have on imaging systems are shown in Fig. 1. In Fig. 1 simulated images of a star for the case $D/r_0=10$ are shown for three different imaging conditions. Figure 1(a) illustrates a short-exposure image of the star, Fig. 1(b) illustrates a long-exposure image of the star, and Fig. 1(c) illustrates the diffraction-limited image of the star. The logarithm of the diffraction-limited image is displayed in Fig. 1(c) to allow the diffraction effects (i.e., the so-called Airy rings) to be easily seen. The term *short exposure* used to describe Fig. 1(a) means that the image measurement time was sufficiently short to “freeze” the turbulence during the image measurement time. The term *long exposure*, associated with Fig. 1(b), describes the case in which the image measurement time was long enough to integrate over many realizations of the turbulence-induced aberration. Because the input object for Fig. 1 was an unresolved point, the images shown in Fig. 1 represent different manifestations of the point-spread function. Clearly, for a short exposure the effects of turbulence are to broaden the point-spread function compared to the diffraction-limited case and to cause the point-spread function to be highly and randomly structured. For a long exposure the point-spread function consists of the integrated effects of many realizations of the turbulence. As a result, the long-exposure image is much broader than the diffraction-limited point-spread function and is much smoother than a short-exposure image. In either the long- or short-exposure case the effect of turbulence is to degrade the resolution of the imaging system.

Though Isaac Newton (1952) was aware that turbulence affected the performance of optical telescopes, little progress was made in the scientific understanding of turbulence effects until the 1950s and 1960s (Roddier,

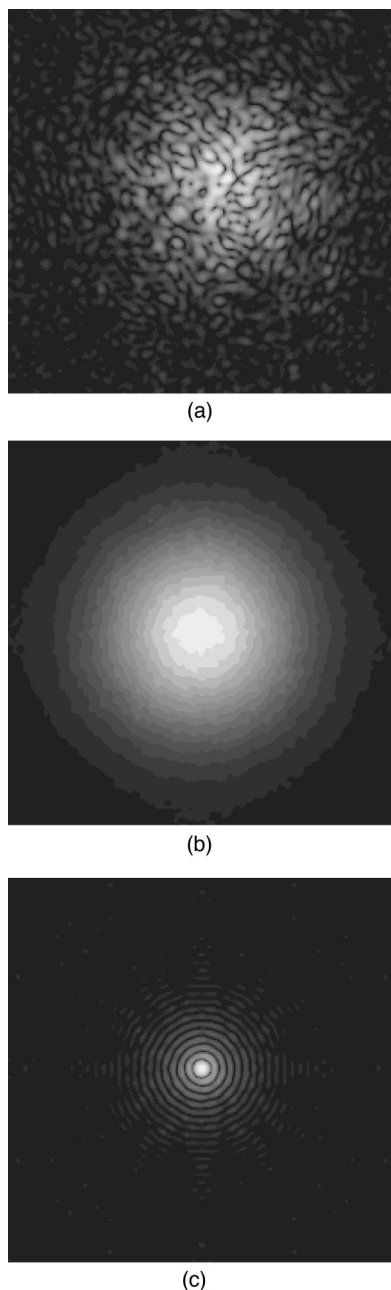


FIG. 1. Simulated star images: (a) short-exposure image; (b) long-exposure image; (c) diffraction-limited image. For these results the telescope diameter is $D=1$ meter, the atmospheric-turbulence conditions represent average seeing at a good observatory site (i.e., the atmospheric coherence diameter $r_0=10$ centimeters), and the mean wavelength is $\lambda=550$ nanometers.

1981). Since that time a large amount of research has been conducted on techniques to overcome turbulence effects on imaging systems. Three broad classes of techniques for overcoming turbulence effects have been developed: (1) pure post-detection image-processing techniques, which are generally referred to as speckle-imaging techniques, (2) adaptive-optics techniques,

which use real-time sensing and correction of the aberrated wave front to overcome turbulence effects, and (3) hybrid techniques that combine elements of both adaptive optics and image post processing to overcome turbulence effects.

Speckle-imaging techniques (Labeyrie, 1970; Knox, 1976; Lohmann *et al.*, 1983) were among the first techniques developed for overcoming the effects of turbulence. These techniques are based on post-detection processing of a large data set of short-exposure images using Fourier-domain methods. Fourier-domain analysis is used in speckle imaging because it can be shown that certain specialized moments of the Fourier transform of a short-exposure image contain diffraction-limited information about the objects of interest (Korff, 1973; Knox, 1976; Lohmann *et al.*, 1983). Hence in speckle imaging the object is estimated by first estimating its Fourier transform and then inverting this Fourier-domain data into an estimate of the object. Speckle imaging is an attractive technique because the only hardware requirements are a camera that has a shuttering mechanism fast enough to freeze the effects of turbulence during the exposure time and a digital computer suitable for processing the measured image data. Unfortunately, the signal-to-noise ratios of the speckle-imaging estimators are strongly degraded by noise arising from both random turbulence effects and the random arrival times and locations of photo events in the detection system.

Adaptive optics, originally proposed by Babcock (1953), are a family of techniques for sensing and correcting for the turbulence-induced aberration in real time *before* an image is measured (Hudgin, 1977b; Wallner, 1983; Welsh and Gardner, 1989; Ellerbroek, 1994). There are three key elements in an adaptive-optics system: (1) the wave-front sensor, which measures quantities related to the instantaneous aberration in the telescope pupil; (2) the deformable mirror, which responds to applied voltages to change its shape to adjust in real time to the changing turbulence-induced aberration; and (3) a controller, which converts wave-front sensor measurements into deformable-mirror commands and maintains the stability of the system. Adaptive optics have an advantage over speckle-imaging techniques of providing narrower instantaneous point-spread functions and hence higher inherent resolution, but there are several fundamental problems associated with adaptive optics.

For example, a beacon of sufficient brightness is required to provide a signal to the wave-front sensing system. At visible wavelengths the shortage of natural beacons is a serious limitation to the utility of adaptive optics. This limitation has given rise to efforts to create artificial beacons by scattering laser light from various molecular and atomic species in the atmosphere (Foy and Labeyrie, 1985; Gardner *et al.*, 1990) to provide wave-front sensor signal. At infrared wavelengths the shortage of natural beacons is somewhat relieved, with nearly complete sky coverage being available at wavelengths of $10 \mu\text{m}$ or longer (Beckers, 1993; Rigaut and

Gendron, 1993). However, the angular resolution obtained by the telescope is limited by use of such long wavelengths.

Further, it is impossible for any real adaptive-optics system to correct fully for the turbulence-induced aberration, due to the finite spatial sampling of the wave front by the wave-front sensor, a limited number of degrees of freedom in the deformable mirror, and measurement noise in the wave-front sensor (Beckers, 1993; Roggemann and Welsh, 1996). Hence there will always be residual error on the wave front, which will degrade imaging performance. Anisoplanatism, which arises from the fact that light from the wave-front sensor beacon and the object of interest must often pass through different columns of air, limits the correctable field of view of the adaptive-optics system to a few tens of microradians at visible wavelengths.

Finally, so-called fully compensated adaptive-optics systems, capable of maximally correcting for turbulence effects, will in the near term be very expensive and "one-of-a kind" systems developed by individual research groups. The expense and complexity of adaptive-optics systems impose a serious barrier to telescope sites seeking to improve resolution beyond the limits imposed by turbulence. The noise limitations of speckle imaging and the complexity and expense of fully compensated adaptive-optics systems have provided the motivation for investigating a number of techniques that combine elements of adaptive optics and post-detection processing, referred to as hybrid imaging techniques. At least three different hybrid imaging techniques have been developed: (1) partially compensating adaptive-optics systems, which provide a lower degree of correction for turbulence effects than the fully compensated systems just mentioned, combined with image reconstruction (Smithson and Peri, 1989; Roggemann, 1991); (2) partially compensating adaptive-optics systems used in conjunction with speckle-imaging techniques (Nisenson and Barakat, 1987; Roggemann and Matson, 1992) and (3) using wave-front information available from a wave-front sensor, either with or without adaptive optics, in the image reconstruction process. This last technique is referred to as deconvolution from wave-front sensing (Gonglewski *et al.*, 1990; Primot *et al.*, 1990; Roggemann and Meinhardt, 1993). Partially compensated adaptive-optics systems are attractive because they require simpler hardware and hence can be developed and operated at much lower cost and risk than fully compensated systems. The reduction in performance of partially compensated systems compared to fully compensated systems provides a role for post-detection image reconstruction. These post-detection image-processing techniques are attractive because it has been shown that the signal-to-noise ratio of the required estimators is acceptable (Roggemann, 1992).

The goals of this paper are to review turbulence effects on imaging systems, to review techniques for overcoming these effects, and to present analysis techniques for predicting and comparing the performance of these techniques. The literature on the subject of imaging

through turbulence is vast and is increasing rapidly. It would be impossible to review the entire body of literature in any single review paper. Hence we have restricted the scope of this paper to emphasize post-detection processing using speckle-imaging, adaptive-optics, and hybrid imaging techniques. It is not our intent to provide a full historical review of all aspects of atmospheric optics, adaptive optics, and image reconstruction. Rather, in this article we review emerging technologies for imaging space objects. Since many applications for imaging through turbulence require imaging exceedingly dim objects, understanding the effects of noise in the image measurement and the post-detection processing is essential in evaluating the appropriateness of any technique for a specific problem. Hence we place emphasis on reviewing techniques for which the effects of the various noises present have been analyzed. Finally, given the number of techniques available to the researcher for imaging through turbulence and the wide range of hardware available to individual experimenters, the problem of comparing the performance of these techniques is also emphasized.

Some aspects of this paper have been included in previous review articles. We call the readers attention to works by Dainty (1975), Labeyrie (1976, 1978), Bates (1982), Roddier (1988b), and Aleksoff *et al.* (1993), on the subject of speckle imaging, and Aleksoff *et al.* (1993), Beckers (1993), and Tyson and Ulrich (1993) on the subject of adaptive optics. At least two related books have also been published (Tyson, 1991; Roggemann and Welsh, 1996).

The remainder of this paper is organized as follows. Statistical preliminaries are presented in Sec. II, including statistical models for turbulence effects and statistical models for the image detection process. Techniques for overcoming turbulence effects are presented in the subsequent sections. Adaptive optical techniques are discussed in Sec. III, where a real, functional adaptive-optics system is discussed and representative experimental results are presented. The post-detection processing methods referred to as speckle-imaging techniques are then presented in Sec. IV. A discussion of the hybrid imaging technique referred to as deconvolution from wave-front sensing (DWFS) is then provided in Sec. V. The hybrid imaging techniques of deconvolution of compensated images and compensated speckle imaging are presented in Secs. VI and VII, respectively. Conclusions are drawn in Sec. VIII.

II. STATISTICAL PRELIMINARIES

In this section we present a review of statistical topics relevant to understanding turbulence effects on imaging systems. There are two sources of randomness that must be addressed in a system that forms images through atmospheric turbulence: (1) randomness arising from the stochastic nature of electromagnetic-wave propagation through the atmosphere; and (2) measurement noise arising from the quantum nature of the light-detection process and additive noise in the image measurement

and recording process. Statistical models for the index-of-refraction fluctuations are required to obtain specific results for calculations of wave propagation through the atmosphere. The most widely used statistical models for the index-of-refraction fluctuations in the atmosphere are presented in Sec. II.A. The topic of wave propagation through a random index-of-refraction region is presented in Sec. II.B. The results of Secs. II.A and II.B are then used in Sec. II.C to derive the standard measures of performance for uncompensated imaging through turbulence, including the average long- and short-exposure optical transfer functions (OTF) and the Strehl ratio. The performance of image-processing-based techniques for overcoming turbulence effects is limited by randomness arising from both atmospheric turbulence and photon and additive noise in the detector. Statistical models characterizing the image-detection process are presented in Sec. II.D. Expressions for the image-spectrum signal-to-noise ratio (SNR) and the SNR of the power spectral density of the detected image are presented in Sec. II.D.

A. Statistics of index-of-refraction fluctuations

The statistics of the spatial structure of turbulence are of critical importance to modeling the optical effects of atmospheric turbulence. The present understanding of the spatial structure of turbulence arises from the study of fluid motion. When the average velocity v_{avg} of a viscous fluid of characteristic size l is gradually increased from very slow to very fast, two distinct states of fluid motion are observed. At very low v_{avg} the fluid motion is found to be laminar, that is, smooth and regular. However, as v_{avg} is increased past some critical value the flow becomes unstable and random. This random fluid motion is called turbulence (Tatarski, 1967; Ishimaru, 1978). The critical average velocity bounding the region between laminar and turbulent flow is a function of the flow geometry, v_{avg} , l , and the kinematic viscosity of the fluid k_v . These quantities are related through the non-dimensional Reynolds number

$$\text{Re} = \frac{v_{\text{avg}} l}{k_v}. \quad (1)$$

When Re exceeds some critical value, which depends on the geometry of the flow, the fluid motion becomes unstable. The kinematic viscosity of air is $k_v = 1.5 \times 10^{-5}$ m²/s, and, if we assume a scale size of $l = 10$ m and a velocity of $v_{\text{avg}} = 1$ m/s, a Reynolds number of $\text{Re} = 6.7 \times 10^5$ is obtained. This Reynolds number is sufficiently high to ensure that atmospheric air flow is nearly always turbulent (Ishimaru, 1978).

Kolmogorov suggested that the kinetic energy of large-spatial-scale motions of a turbulent flow is transferred to smaller-scale motions (Kolmogorov, 1961). He also assumed that the small-scale turbulent motions are both homogeneous and isotropic. The term homogeneous is analogous to stationarity and implies that the statistical characteristics of the turbulent flow are independent of position within the flow field. The term iso-

tropic is a stronger assumption that implies homogeneity and in addition requires that the second and higher-order statistical moments depend only on the distance between any two points in the field. As the scale size l of the air flow becomes smaller, the Reynolds number associated with that region of air flow is reduced. When the Reynolds number falls below some critical value, turbulent motion stops, and the remaining kinetic energy is dissipated as heat. Kolmogorov's theory provides a mathematical form for the spatial frequency domain statistics of the index-of-refraction variations in the atmosphere (Roddier, 1981).

The physical source of the index-of-refraction variations in the atmosphere is temperature inhomogeneities arising from turbulent air motion. The index of refraction of the atmosphere $n(\vec{r}, t)$ is modeled as the sum of a mean index of refraction n_0 and a randomly fluctuating term $n_1(\vec{r}, t)$:

$$n(\vec{r}, t) = n_0 + n_1(\vec{r}, t), \quad (2)$$

where \vec{r} is a three-dimensional position vector and t is time. The mean index of refraction of air is $n_0 \approx 1$. At optical wavelengths, the dependence of the index of refraction of air upon pressure and temperature is given by (Ishimaru, 1978)

$$n_1 \equiv n - 1 = \frac{77.6P}{T} \times 10^{-6}, \quad (3)$$

where T is the temperature of the air in kelvin and P is the pressure of the air in millibars. Pockets of air that have a uniform index of refraction are generally referred to as *turbulent eddies*. The statistical distribution of the size and number of these turbulent eddies is characterized by the spatial power spectral density of $n_1(\vec{r})$, denoted $\Phi_n(\vec{\kappa})$. The independent variable $\vec{\kappa}$ is the spatial wave-number vector with orthogonal components $(\kappa_x, \kappa_y, \kappa_z)$. $\Phi_n(\vec{\kappa})$ may be considered a measure of the relative abundances of turbulent eddies with scale sizes $l_x = 2\pi/\kappa_x$, $l_y = 2\pi/\kappa_y$, and $l_z = 2\pi/\kappa_z$. Under conditions where homogeneous, isotropic turbulence may be assumed, the power spectral density of the index-of-refraction fluctuations is a function of the scalar wave number, $\kappa = \sqrt{\kappa_x^2 + \kappa_y^2 + \kappa_z^2}$, which is related to the isotropic scale size by $l = 2\pi/\kappa$.

In the Kolmogorov theory the mathematical form of $\Phi_n(\vec{\kappa})$ has three regimes. For very small κ , $\kappa < 2\pi/L_0$, corresponding to large scale sizes, Kolmogorov's theory does not predict a mathematical form for $\Phi_n(\vec{\kappa})$. The quantity L_0 is referred to as the *outer scale* of the turbulence and represents the characteristic dimension of the largest turbulent eddies, which break up following the Kolmogorov theory. In this regime $\Phi_n(\vec{\kappa})$ depends upon local geographical and meteorological conditions (Goodman, 1985). Inhomogeneities with scale sizes greater than L_0 are not believed to be homogeneous. However, the smaller-scale index-of-refraction inhomogeneities affecting optical systems originate with these large-scale inhomogeneities.

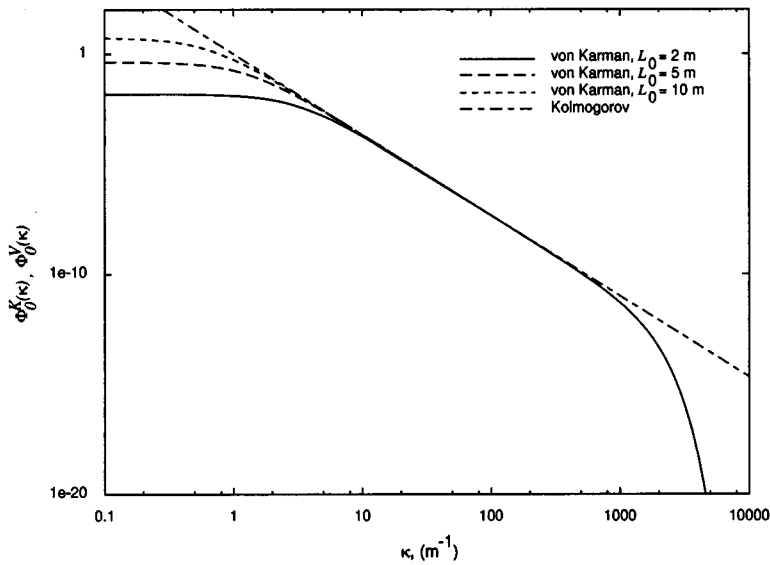


FIG. 2. Normalized Kolmogorov and von Karman turbulence spectra, $\Phi_0^K(\kappa)$ and $\Phi_0^V(\kappa)$. For the von Karman spectra the inner scale is $l_0 = 5$ mm and the outer scale is varied, with $L_0 = 2$ m, 5 m, and 10 m.

For large κ , $\kappa > 2\pi/l_0$, $\Phi_n(\vec{\kappa})$ is also not predicted by the Kolmogorov theory. The quantity l_0 is referred to as the *inner scale* of the turbulence and represents the characteristic dimension of the smallest turbulent eddies. In this regime of scale sizes the turbulent eddies disappear, and the remaining energy in the fluid motion is dissipated as heat. $\Phi_n(\vec{\kappa})$ is known to be quite small in this regime (Goodman, 1985). The inner scale l_0 is on the order of a few millimeters.

When κ is in the range $2\pi/L_0 \leq \kappa \leq 2\pi/l_0$, referred to as the inertial subrange, the form of $\Phi_n(\vec{\kappa})$ is predicted by the Kolmogorov theory (Ishimaru, 1978). Within the inertial subrange the Kolmogorov theory predicts that $\Phi_n(\vec{\kappa})$ takes the form

$$\Phi_n^K(\vec{\kappa}) = 0.033 C_n^2 \kappa^{-11/3}, \quad (4)$$

where the superscript K indicates the Kolmogorov spectrum. The quantity C_n^2 is called the *structure constant* of the index-of-refraction fluctuations and has units of $\text{m}^{-2/3}$. C_n^2 characterizes the strength of the index-of-refraction fluctuations. Since Eq. (4) is a function of the scalar magnitude of $\vec{\kappa}$, the turbulent eddies are isotropic and homogeneous. However, as already noted, eddies with scale size greater than L_0 are not believed to be homogeneous. Thus care must be exercised in interpreting the behavior of $\Phi_n^K(\vec{\kappa})$ in the $\kappa < 2\pi/L_0$ regime. Henceforth we shall discuss only homogeneous, isotropic turbulence statistics, and as such, the scalar wave number will replace the vector wave number in the argument of Φ_n . Experimental evidence that the turbulence-induced wave-front error is well described by Kolmogorov's model was obtained in 1970 for horizontal paths (Bertolotti *et al.*, 1970; Wessely and Bolstad, 1970) and in 1973 for vertical paths (Roddiier and Roddiier, 1973).

Mathematical problems arise when Eq. (4) is used to model the spectrum of the index-of-refraction fluctuations in the $\kappa \rightarrow 0$ regime because of the nonintegrable pole at $\kappa = 0$. To overcome this difficulty an alternate

form for $\Phi_n(\kappa)$, referred to as the von Karman spectrum, has been used (Ishimaru, 1978). The von Karman spectrum is given by

$$\Phi_n^V(\kappa) = \frac{0.033 C_n^2}{(\kappa^2 + \kappa_0^2)^{11/6}} \exp\left\{-\frac{\kappa^2}{\kappa_m^2}\right\}, \quad (5)$$

where $\kappa_0 = 2\pi/L_0$, $\kappa_m = 5.92/l_0$, and the superscript V indicates the von Karman spectrum. A finite value of κ_0 results in a finite value of $\Phi_n^V(0)$, while a finite κ_m has the effect of rapidly rolling off the spectrum for $\kappa > \kappa_m$. It should be noted that even though Eq. (5) is finite for all κ , its form for wave numbers in the range $\kappa < 2\pi/L_0$ should be considered approximate.

The shapes of the normalized Kolmogorov and von Karman spectra are shown in Fig. 2. For the von Karman spectra curves the inner scale is $l_0 = 5$ mm and the outer scale is varied, with $L_0 = 2, 5,$ and 10 m. The roles of the inner and outer scales in the von Karman spectrum are also shown in Fig. 2. The effect of the inner scale is to reduce the value of $\Phi_0^V(\kappa)$ compared to $\Phi_0^K(\kappa)$ for wave numbers in the $\kappa > 2\pi/l_0$ regime. This is consistent with the physical observation that turbulent air motion ceases once scale sizes on the order of l_0 have been attained. The effect of the outer scale is to reduce the the value of $\Phi_0^V(\kappa)$ compared to $\Phi_0^K(\kappa)$ for wave numbers in the $\kappa < 2\pi/L_0$ regime. As L_0 increases the amount of power in the lower-wave-number components of $\Phi_0^V(\kappa)$ increases, and at very low wave numbers $\Phi_0^V(\kappa) \rightarrow \Phi_0^K(\kappa)$ as $L_0 \rightarrow \infty$. However, care must be used in choosing L_0 for use in the von Karman spectrum. Experimental evidence indicates that L_0 is at least several meters in the free atmosphere (Colavita, 1990; Dayton *et al.*, 1992; Tatarskii and Zavorotny, 1993; Haniff *et al.*, 1994).

For many systems of practical interest the strength of the turbulence is a function of distance from the aperture z . This is particularly true for astronomical observing conditions, where it is necessary to view space objects through a vertical column of air. The notation

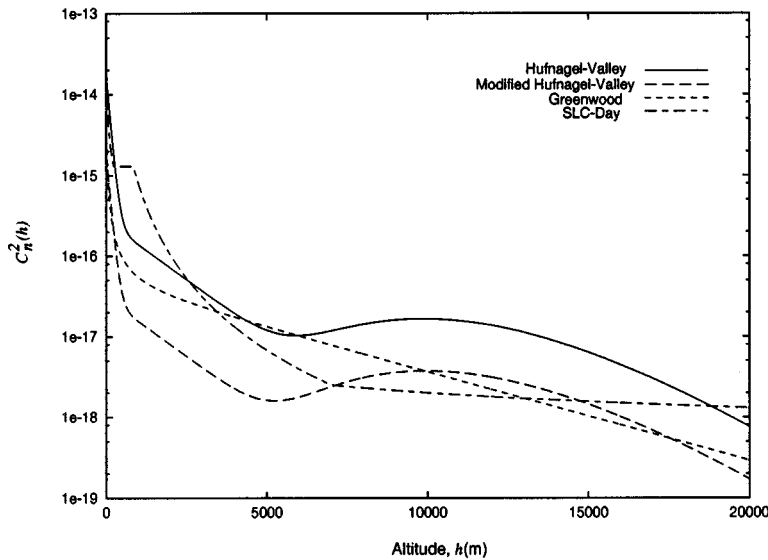


FIG. 3. Some widely used models for turbulence strength $C_n^2(h)$ as a function of altitude h .

$C_n^2(z)$ is used to indicate the dependence of the turbulence strength upon distance in Eqs. (4) and (5), and the general notation $\Phi_n(\kappa, z)$ is used to indicate the distance-dependent power spectral density.

The important role of the turbulence strength, as characterized by C_n^2 , in predicting the optical effects of turbulence has motivated the extensive study of this parameter. C_n^2 has been found to vary as functions of altitude, location, and time of day. Several mathematical models have been developed from experimental measurements of C_n^2 . Some of the commonly used models are discussed by Parenti and Sasiela (1994) and Roggemann and Welsh (1996) and are shown in Fig. 3.

Thus far we have presented only the spectral statistics of the turbulence-induced index-of-refraction fluctuations. These spectral representations have associated spatial representations in the form of spatial correlation functions and spatial structure functions. The spectral and spatial representations are related through the Fourier transform. These relationships are presented in this section and used in the succeeding sections to investigate wave propagation and imaging through turbulence. We shall consider the second-order statistics of the random three-dimensional index-of-refraction fluctuations $n_1(\vec{r})$.

The autocorrelation, $\Gamma_n(\vec{r}) = \langle n_1(\vec{r}_1)n_1(\vec{r}_1 - \vec{r}) \rangle$, and the power spectral density $\Phi_n(\vec{\kappa})$ of $n_1(\vec{r})$ are related by the Wiener-Khinchin theorem (Goodman, 1985):

$$\Gamma_n(\vec{r}) = \int d\vec{\kappa} \Phi_n(\vec{\kappa}) \exp\{-i\vec{\kappa} \cdot \vec{r}\}, \quad (6)$$

where the notation $\langle \cdot \rangle$ is used to represent the statistical expectation operator. The power spectral density is obtained from $\Gamma_n(\vec{r})$ by

$$\Phi_n(\vec{\kappa}) = \frac{1}{(2\pi)^3} \int d\vec{r} \Gamma_n(\vec{r}) \exp\{i\vec{\kappa} \cdot \vec{r}\}. \quad (7)$$

In words, Eqs. (6) and (7) state that the autocorrelation of $n_1(\vec{r})$ and the power spectral density of $n_1(\vec{r})$ form a

three-dimensional Fourier-transform pair. Note that in this section we have adopted Tatarskii's convention for defining the forward and inverse Fourier-transform kernels (Tatarski, 1967). This choice does not affect the results that follow.

It should be noted that both the autocorrelation function and the power spectral density for homogeneous random processes are guaranteed to be even functions (Tatarski, 1967; Papoulis, 1991). The additional assumption that $n_1(\vec{r})$ is an isotropic random process allows the autocorrelation and power spectral density of $n_1(\vec{r})$ to be written in terms of the scalar variables $r = |\vec{r}|$ and $\kappa = |\vec{\kappa}|$ (Tatarski, 1967):

$$\Gamma_n(r) = \frac{4\pi}{r} \int_0^\infty \kappa d\kappa \Phi_n(\kappa) \sin(\kappa r), \quad (8)$$

$$\Phi_n(\kappa) = \frac{1}{2\pi^2 \kappa} \int_0^\infty r dr \Gamma_n(r) \sin(\kappa r). \quad (9)$$

We now introduce the structure function of the random index-of-refraction distribution. The structure function has a special role in the analysis of systems that form images through atmospheric turbulence, since, as shown in Sec. II.C, the structure function of the turbulence-corrupted index of refraction arises naturally in the analysis of the optical transfer function. The structure function of the index-of-refraction fluctuation is defined as

$$D_n(\vec{r}) = \langle [n_1(\vec{r}_1) - n_1(\vec{r}_1 + \vec{r})]^2 \rangle. \quad (10)$$

Equation (6) can be used to express $D_n(\vec{r})$ as a function of the power spectral density by

$$\begin{aligned} D_n(\vec{r}) &= 2 \left[\int d\vec{\kappa} \Phi_n(\vec{\kappa}) - \int d\vec{\kappa} \Phi_n(\vec{\kappa}) e^{-i\vec{\kappa} \cdot \vec{r}} \right] \\ &= 2 \int d\vec{\kappa} [1 - \cos(\vec{\kappa} \cdot \vec{r})] \Phi_n(\vec{\kappa}). \end{aligned} \quad (11)$$

If $n_1(\vec{r})$ is also isotropic, the structure function depends only on the scalar variable $r = |\vec{r}|$, and, if we use the

● Distant Astronomical Source

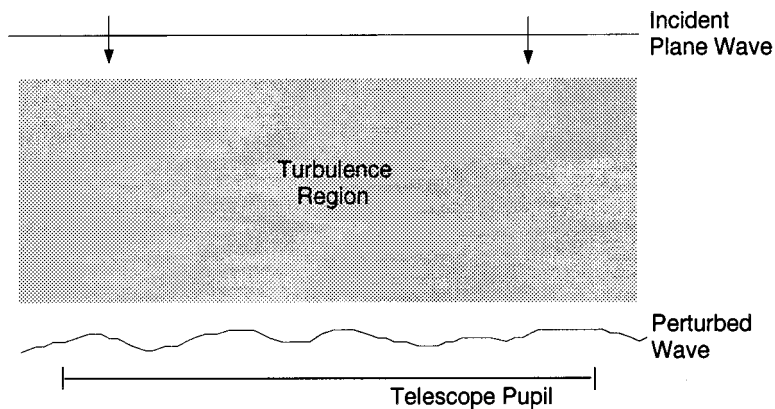


FIG. 4. Astronomical imaging geometry. A distant source gives rise to an incident plane wave. The problem at hand is to find the correlation function describing the atmospheric-induced field perturbations in the pupil.

Kolmogorov power spectrum $\Phi_n^K(\vec{\kappa})$ in a region where C_n^2 is assumed constant, we obtain the result

$$D_n(r) = C_n^2 r^{2/3}. \quad (12)$$

Thus far we have not addressed the temporal evolution of turbulence. However, the temporal behavior of turbulence can be quite important for accurately modeling certain aspects of imaging through turbulence. Examples of problems in which the temporal behavior of turbulence is important include computing the optimal exposure time for speckle imaging (Walker, 1978; O'Donnell and Dainty, 1980; Cochran *et al.*, 1988; Fried and Hench, 1990; Lawrence *et al.*, 1992; Tyler and Matson, 1993; Welsh, 1995) and choosing the optimal closed-loop control bandwidth for an adaptive-optics system (Roddier *et al.*, 1993; Ellerbroek, 1994; Harrington and Welsh, 1994).

The temporal effects of turbulence are generally modeled using Taylor's frozen-flow hypothesis (Ishimaru, 1978; Goodman, 1985). In words, Taylor's frozen-flow hypothesis states that over short-time intervals the index-of-refraction fluctuation remains fixed except for translation with uniform transverse velocity \vec{v} . In this case, the term transverse velocity refers to the component of the wind velocity normal to the line of sight of the imaging system. For a point in space \vec{r} and a single layer of turbulence, the frozen-flow hypothesis means that the index-of-refraction fluctuation at $t_2 > t_1$, $n_1(\vec{r}, t_2)$, is related to the index-of-refraction fluctuation at t_1 , $n_1(\vec{r}, t_1)$, by

$$n_1(\vec{r}, t_2) = n_1(\vec{r} - \vec{v}(t_2 - t_1), t_1). \quad (13)$$

The generalized space-time covariance of the index-of-refraction fluctuation, $\Gamma_n^S(\vec{r}_1, t_1; \vec{r}_2, t_2)$, is defined by

$$\Gamma_n^S(\vec{r}_1, t_1; \vec{r}_2, t_2) = \langle n_1(\vec{r}_1, t_1) n_1(\vec{r}_2, t_2) \rangle, \quad (14)$$

where the times t_1 and t_2 are included in the argument of Γ_n^S to indicate the time dependence, and \vec{r}_1 and \vec{r}_2 indicate different points in space. Using the frozen-flow hypothesis of Eq. (13) in Eq. (14) yields

$$\Gamma_n^S(\vec{r}_1, t_1; \vec{r}_2, t_2) = \langle n_1(\vec{r}_1, t_1) n_1(\vec{r}_2 - \vec{v}(t_2 - t_1), t_1) \rangle. \quad (15)$$

Equation (15) shows that the frozen-flow hypothesis allows time differences to be represented as spatial shifts. This is an extremely important result, which allows analytic simplifications to many problems.

B. Wave propagation through random media

As introduced in Sec. II.A, atmospheric turbulence is characterized by random variations in the index of refraction. As an optical field propagates through a region of turbulence, these variations cause phase perturbations in the wave front. Propagation causes the phase perturbations to evolve into both phase and amplitude perturbations. In the case of astronomical imaging we are interested in the situation in which the optical field propagates from a distant source through the turbulence to the pupil plane of a telescope. A number of authors have presented analyses of the statistical characteristics of the optical field for this geometry (Tatarski, 1967; Lee and Harp, 1969; Roddier, 1981; Goodman, 1985; Roggemann and Welsh, 1996). Figure 4 illustrates the geometry of interest. In this section we show that a second-order statistical description of the index-of-refraction variations is all that is needed to develop a description of the optical-field correlation properties in the pupil. This statistical description of the pupil field is in turn

used to derive the standard measures of performance for uncompensated imaging in Sec. II.C.

To begin we consider the problem of a plane wave propagating through a turbulent region as shown in Fig. 4. The goal is to derive the pupil-field correlation function arising from the turbulence-induced perturbations of the plane wave. This derivation is based on a geometrical-optics approach, which is equivalent to assuming that refraction can be neglected. This assumption is also referred to as the near-field assumption. Near-field conditions are said to exist if the total thickness of the turbulence region ΔZ satisfies (Young, 1974)

$$\Delta Z \leq \frac{r_0^2}{\lambda \pi}, \quad (16)$$

where r_0 is the Fried parameter (Fried, 1966b) and λ is the optical wavelength.

The section is concluded with a presentation of temporal and anisoplanatic effects on the pupil-field correlation properties. Understanding temporal and anisoplanatic effects is important for characterizing the performance of adaptive optical systems as will be discussed in Sec. III.

1. Derivation of the pupil-field spatial correlation function

In Sec. II.A we discussed the distribution of the turbulence strength as a function of altitude. For the derivation given below we break the atmosphere into a finite number of slabs or layers. Each layer is characterized by a turbulence strength that is approximately constant within the layer. The notation $C_{n_i}^2$ is used to designate the structure constant for the i th layer. The notations z_i and Δz_i designate the altitude and thickness of the i th layer.

The problem of calculating the spatial correlation properties of the turbulence-induced field perturbations can be reduced to calculating the correlation properties for propagation through a single turbulence layer and then extending the results to account for all layers. The basic assumption required to use this approach concerns the statistical independence of the index-of-refraction fluctuations between individual layers (Tatarski (1967) and others (Goodman, 1985; Troxel *et al.*, 1994) have investigated this assumption and have argued that individual layers can be treated as being approximately independent if the separation of layer centers is greater than the largest distance between field points in the pupil. The independence condition allows us to characterize the spatial correlation properties of the field perturbations for each layer separately and multiply the results to account for propagation through the entire turbulence region. Mathematically we can write

$$\Gamma_p(\Delta \vec{x}) \equiv \langle u(\vec{x}) u^*(\vec{x} + \Delta \vec{x}) \rangle = \prod_{i=1}^N \Gamma_{p_i}(\Delta \vec{x}), \quad (17)$$

where $u(\vec{x})$ is the complex representation of the optical field in the telescope pupil, $\Gamma_p(\Delta \vec{x})$ is the spatial correlation function of the optical field in the pupil, $\Gamma_{p_i}(\Delta \vec{x})$

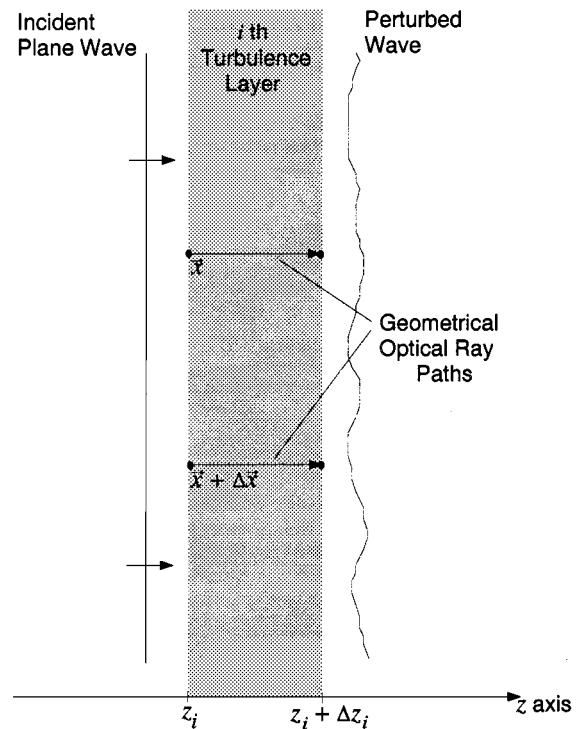


FIG. 5. Plane-wave propagation through a single turbulence layer.

is the spatial correlation function for the field perturbations associated with the i th layer, $\Delta \vec{x}$ is the vector separation of two points in a plane perpendicular to the direction of propagation, and N is the number of layers comprising the turbulence region. The problem now reduces to computing the spatial correlation function for the turbulence-induced perturbations of a single turbulence layer (Troxel *et al.*, 1994).

a. Plane-wave propagation

Consider the geometry of the single turbulent layer shown in Fig. 5. A plane wave is incident from the left. Using geometrical optics, the phase variations caused by propagation along a ray path extending from the left edge to the right edge of the layer is given by

$$\psi_i(\vec{x}) = k \int_{z_i}^{z_i + \Delta z_i} dz n_1(\vec{x}, z), \quad (18)$$

where $\psi_i(\vec{x})$ is the phase perturbation at the transverse-vector location \vec{x} , k is the optical wave number ($2\pi/\lambda$), and $n_1(\vec{x}, z)$ is the index-of-refraction variation as a function of position (\vec{x}, z) . In writing the three-dimensional argument of n_1 we have chosen to show the transverse-vector component \vec{x} and the z component separately. For a unit-amplitude plane wave incident on the left, the transmitted optical field on the right of the i th layer can be expressed as

$$u_i(\vec{x}) = \exp[i\psi_i(\vec{x})]. \quad (19)$$

The spatial correlation function for $u_i(\vec{x})$ is given by $\Gamma_{p_i}(\Delta \vec{x}) = \langle u_i(\vec{x}) u_i^*(\vec{x} + \Delta \vec{x}) \rangle$. In expressing the spatial

correlation function in this way we have implicitly assumed that the turbulence-induced perturbations are homogeneous. Substituting the expression for the field found in Eq. (19) into $\Gamma_{p_i}(\Delta\vec{x})$ gives

$$\Gamma_{p_i}(\Delta\vec{x}) = \left\langle \exp \left[ik \left(\int_{z_i}^{z_i+\Delta z_i} dz [n_1(\vec{x}, z) - n_1(\vec{x} - \Delta\vec{x}, z)] \right) \right] \right\rangle. \tag{20}$$

Without an assumption regarding the statistics of the index-of-refraction fluctuation $n_1(\vec{x}, z)$, further progress is impossible. Using the central-limit theorem it can be argued that $n_1(\vec{x}, z)$ is a Gaussian random process (Fried, 1966b; Tatarski, 1967; Goodman, 1985). This assumption allows us to use well-known properties of characteristic functions for Gaussian random processes (Papoulis, 1991). Using these properties it is easy to show (Roggemann and Welsh, 1996)

$$\Gamma_{p_i}(\Delta\vec{x}) = \exp \left[-\frac{1}{2} D_{\psi_i}(\Delta\vec{x}) \right], \tag{21}$$

where $D_{\psi_i}(\Delta\vec{x})$ is the phase structure function and is defined as

$$D_{\psi_i}(\Delta\vec{x}) = \left\langle k^2 \left(\int_{z_i}^{z_i+\Delta z_i} dz [n_1(\vec{x}, z) - n_1(\vec{x} - \Delta\vec{x}, z)] \right)^2 \right\rangle. \tag{22}$$

The problem of characterizing $\Gamma_{p_i}(\Delta\vec{x})$ now becomes one of calculating the phase structure function $D_{\psi_i}(\Delta\vec{x})$. If we assume Kolmogorov statistics and that the thickness of the turbulent layer is significantly larger than the separation of the two field points, $|\Delta\vec{x}|$, we obtain the result first reported in the literature by Fried (1966b):

$$D_{\psi_i}(\Delta\vec{x}) = 2.91 k^2 \Delta z_i C_{n_i}^2 |\Delta\vec{x}|^{5/3}. \tag{23}$$

With the phase structure function for the i th layer established, we now compute the field correlation function $\Gamma_{p_i}(\Delta\vec{x})$ by substituting Eq. (23) into Eq. (21)

$$\Gamma_{p_i}(\Delta\vec{x}) = \exp \left[-\frac{1}{2} 2.91 k^2 \Delta z_i C_{n_i}^2 |\Delta\vec{x}|^{5/3} \right], \tag{24}$$

which can be substituted into Eq. (17) to obtain the correlation expression for propagation through the entire turbulent region.

Fried expresses the phase structure function as a function of a quantity called the Fried parameter r_0 . The Fried parameter is defined as (Fried, 1966b; Goodman, 1985)

$$r_0 = 0.185 \left[\frac{4\pi^2}{k^2 \sum_{i=1}^N C_{n_i}^2 \Delta z_i} \right]^{3/5}. \tag{25}$$

With this value of r_0 the final expression for $\Gamma_p(\Delta\vec{x})$ becomes

$$\begin{aligned} \Gamma_p(\Delta\vec{x}) &= \exp \left[-\frac{1}{2} 6.88 \left(\frac{|\Delta\vec{x}|}{r_0} \right)^{5/3} \right] \\ &= \exp \left[-\frac{1}{2} D_{\psi}(\Delta\vec{x}) \right], \end{aligned} \tag{26}$$

where D_{ψ} is the structure function for propagation through the entire atmosphere

$$D_{\psi}(\Delta\vec{x}) = 6.88 \left(\frac{|\Delta\vec{x}|}{r_0} \right)^{5/3}. \tag{27}$$

Equations (26) and (27) represent the two main results for plane-wave propagation. These two results show that the structure function $D_{\psi}(\Delta\vec{x})$ is all that is required to characterize the pupil-field correlation function $\Gamma_p(\Delta\vec{x})$.

b. Spherical-wave propagation

In many instances the incident optical field will arise from a source that is close enough that a spherical wave more accurately models the incident field. In this case the phase structure function for spherical-wave propagation is identical to Eq. (27) (Goodman, 1985) but with a Fried parameter for spherical-wave propagation given by

$$r_0 = 0.185 \left[\frac{4\pi^2}{k^2 \sum_{i=1}^N \Delta z_i \left(\frac{L-z_i}{L} \right)^{5/3} C_{n_i}^2} \right]^{3/5} \tag{spherical wave}, \tag{28}$$

where L is the propagation distance from the source to the aperture.

2. Temporal and anisoplanatic effects

In Sec. II.A we discussed the temporal correlation properties of the index-of-refraction fluctuations. Understanding how these temporal properties impact the temporal properties of the optical field is important for investigating a number of problems in speckle imaging and adaptive optics.

The correlation properties of the optical fields arising from separate propagation directions are also of interest. In the operation of an adaptive optical imaging (AOI) system the applied wave-front compensation is based on sensing the wave-front phase perturbations arising from a beacon or guide star. The sensed perturbations are used to compensate for the wave-front perturbations associated with a separate observation direction. The observation and beacon directions are generally distinct from each other, and, as a result, the phase perturbations associated with the two directions are different. This difference results in a performance degradation that is referred to as an *anisoplanatic* effect. To fully understand the extent of anisoplanatic effects one needs to know the correlation between the pupil fields arising from the two directions. In the following subsection we present expressions that characterize how

● Distant Astronomical Source

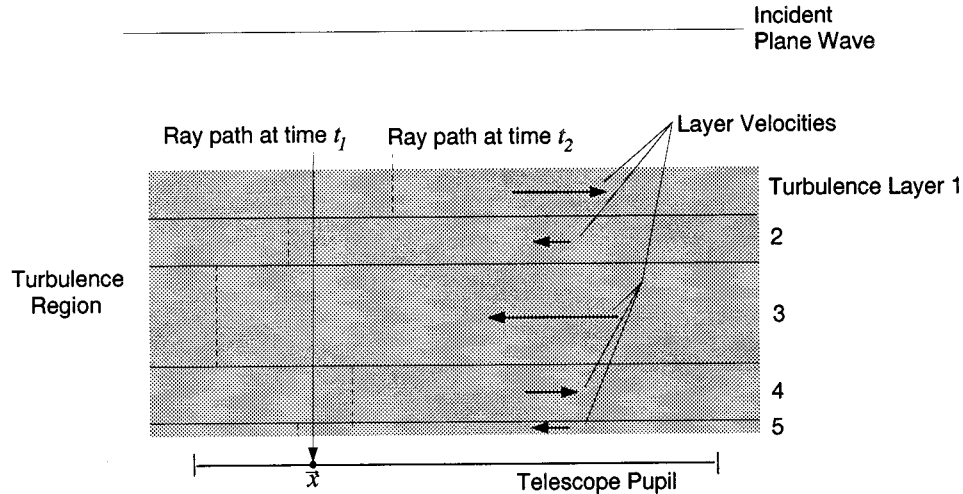


FIG. 6. Geometry for understanding the temporal evolution of the wave-front phase in the pupil of the imaging system. Each turbulence layer has an associated transverse wind velocity \vec{v}_i .

the temporal index-of-refraction fluctuations affect the temporal correlation properties of the pupil field and how anisoplanatism affects the angular correlation properties of the pupil field.

a. Temporal effects on the pupil-field correlation function

To develop the field correlation function describing the effects of temporal changes in the index of refraction, we use Taylor’s frozen-flow hypothesis (Ishimaru, 1978; Goodman, 1985) in combination with a geometrical-optics analysis. Figure 6 shows the geometry used to model the temporal wave-front phase evolution. The i th turbulence layer shown in the figure has an associated transverse wind velocity \vec{v}_i . The straight-ray path shown in Fig. 6 represents the path over which the optical field propagates at time t_1 . To calculate the phase perturbation at time t_2 ($t_2 > t_1$), the translation of the layers must be factored into the computation. Taylor’s

frozen-flow hypothesis calls for translating the i th layer by $\vec{v}_i(t_2 - t_1)$. By accounting for the translations of each of the layers, one obtains the piecewise ray path shown in Fig. 6 (dashed lines) as the resulting ray path at time t_2 . The goal is to compute the space-time correlation function

$$\Gamma_p(\Delta\vec{x}, t_2 - t_1) = \langle u(\vec{x}, t_1) u^*(\vec{x} - \Delta\vec{x}, t_2) \rangle, \quad (29)$$

where $\Delta\vec{x}$ is the spatial separation of two points in the pupil. From a development identical to that used to obtain the plane-wave correlation function given in Eq. (24), it is straightforward to show that the space-time correlation function $\Gamma_p(\Delta\vec{x}, t_2 - t_1)$ has the following familiar form:

$$\Gamma_p(\Delta\vec{x}, t_2 - t_1) = \exp\left[-\frac{1}{2} D_\psi(\Delta\vec{x}, t_2 - t_1)\right], \quad (30)$$

where $D_\psi(\Delta\vec{x}, t_2 - t_1)$ is now interpreted as the space-time phase structure function given by

$$D_\psi(\Delta\vec{x}, t_2 - t_1) = 6.88 \sum_{i=1}^N \Delta z_i \left(\frac{|\Delta\vec{x} + \vec{v}(z_i)(t_2 - t_1)|}{r_0} \right)^{5/3} \tilde{C}_{n_i}^2 \quad (\text{plane-wave result}) \quad (31)$$

and $\tilde{C}_{n_i}^2$ is a normalized version of $C_{n_i}^2$: $\tilde{C}_{n_i}^2 = C_{n_i}^2 / \sum_{i=1}^N \Delta z_i C_{n_i}^2$. The spherical-wave phase structure function is a generalization of Eq. (31):

$$D_\psi(\Delta\vec{x}, t_2 - t_1) = 6.88 \sum_{i=1}^N \Delta z_i \left(\frac{\left| \Delta\vec{x} \frac{L - z_i}{L} + \vec{v}(z_i)(t_2 - t_1) \right|}{r_0} \right)^{5/3} \tilde{C}_{n_i}^2 \quad (\text{spherical-wave result}), \quad (32)$$

where r_0 is given by Eq. (25).

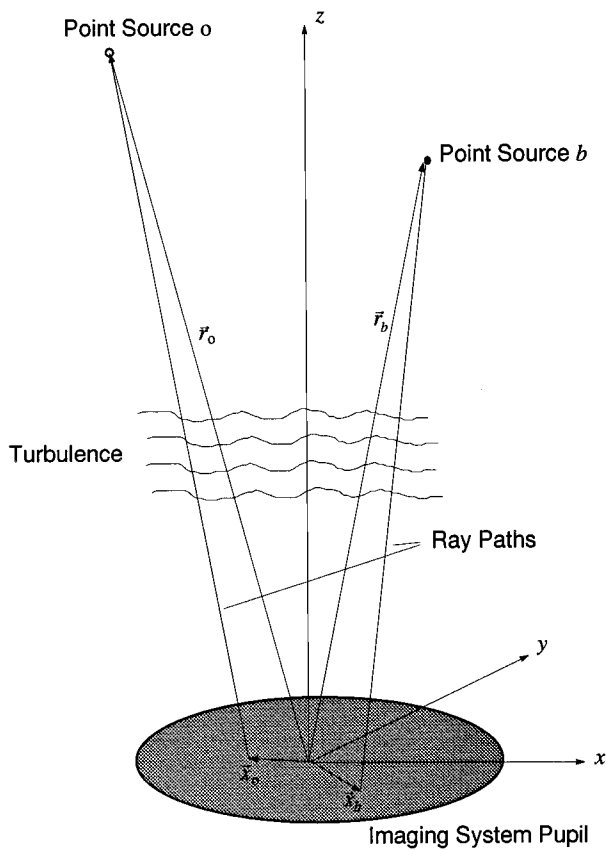


FIG. 7. Geometry for deriving the anisoplanatic effects on the wave-front phase in the pupil of the imaging system.

b. Anisoplanatic effects on the pupil-field correlation function

The method of calculating the pupil-field correlation function for the temporal effects can be extended directly to the anisoplanatic case. Just as in the computation of the temporal correlation function, the quantity that must be obtained is the phase structure function. Here the phase structure function characterizes the statistical correlation properties of the wave-front phase for two optical fields propagating from two distinct directions. In other words we are interested in $D_\psi(\vec{x}_o, \vec{x}_b) = \langle (\psi_o(\vec{x}_o) - \psi_b(\vec{x}_b))^2 \rangle$, where $\psi_o(\vec{x})$ and $\psi_b(\vec{x})$ are the wave-front phases of the two distinct optical fields. Figure 7 shows the geometry under consideration. This figure shows the imaging-system pupil and two optical source points. Ray paths are shown from the source points to two points in the pupil. In the case of adaptive optical imaging, one of the source points models the beacon. The other source point represents the object being imaged. The generalized geometry shown in Fig. 7 can be used to model any beacon-object-pupil geometry that might be encountered in an adaptive optical imaging scenario.

As seen from Fig. 7, the two optical sources are located at the vector positions \vec{r}_o and \vec{r}_b . The z components of these two vectors are designated z_o and z_b , respectively. The vector positions \vec{x}_o and \vec{x}_b designate two field points in the pupil plane. The subscripts o and b are arbitrary but can be related to the object and the

beacon wave-front sources. To calculate the phase structure function, we characterize the transverse distance between the two ray paths as a function of z . The transverse separation of the two ray paths has been shown to be (Welsh and Gardner, 1991)

$$\Delta \vec{p}_{ob}(z) = \vec{x}_o - \vec{x}_b + \frac{z}{z_o}(\vec{r}_o - \vec{x}_o) - \frac{z}{z_b}(\vec{r}_b - \vec{x}_b). \quad (33)$$

Using a geometrical-optics derivation identical to that used to obtain the plane- and spherical-wave phase structure functions of the previous section, Lutomirski and Buser (1973) have shown that the phase structure function for the geometry shown in Fig. 7 is given by

$$D_\psi(\vec{x}_o, \vec{x}_b) = 6.88 \sum_{i=1}^N \Delta z_i \left(\frac{|\Delta \vec{p}_{ob}(z_i)|}{r_0} \right)^{5/3} \bar{C}_{n_i}^2, \quad (34)$$

where $\Delta \vec{p}_{ob}(z)$ is the transverse separation of the object and beacon ray paths. The limitations of Eq. (34) are related to the approximations invoked by Lutomirski and Buser. In particular, the pupil points, \vec{x}_o and \vec{x}_b , and the source points must be close to the z axis relative to the distance to the two sources, z_o and z_b .

C. Imaging performance

Optical-wave propagation through the atmosphere has the effect of altering the spatial coherence of the field in the pupil. The statistical nature of this alteration has been presented in Sec. II.B via the development of the pupil-field correlation function $\Gamma_p(\Delta \vec{x})$ and the wave-front phase structure function $D_\psi(\Delta \vec{x})$. In this section we present an analysis of the turbulence-induced degradations suffered by an incoherent imaging system. A random-screen model for the turbulence is first presented. The random screen is placed in the pupil plane of the imaging system and effectively models the atmospheric-induced field perturbations. The statistical characteristics of the screen are used to characterize imaging performance via the optical transfer function (OTF). The result of incorporating these statistics is a "transfer function" applicable for propagation through the Earth's atmosphere. The imaging performance results are for long-exposure imaging and short-exposure imaging.

1. Thin-screen turbulence model

In order to use the plane- and spherical-wave results of the previous sections it is convenient to cast the turbulence-propagation problem in terms of propagation through an equivalent thin, random screen. The screen takes on the statistical correlation properties

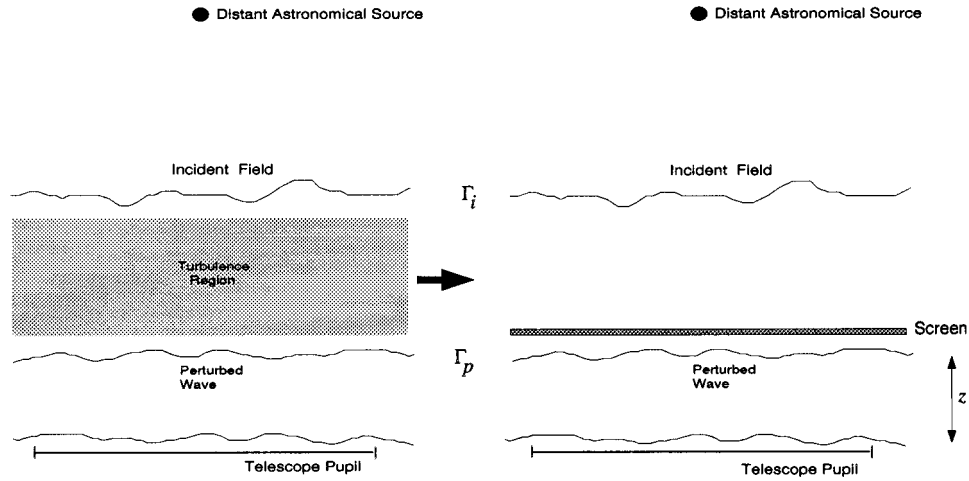


FIG. 8. Geometry for characterizing the relationship between the input and output spatial coherence properties of an optical field for propagation through a homogeneous, isotropic turbulence region. Γ_i represents the correlation function of the field incident on the turbulent region, and Γ_p represents the correlation function after passing through the turbulent region.

found in Sec. II.B and is used to characterize the phase perturbations caused by propagation through the turbulence.

Figure 8 shows the propagation geometry of interest. The figure shows that the screen model is used to effectively replace the turbulence region. The screen perturbs the phase of the incident optical field in the same statistical way that propagation through turbulence does. In mathematical terms the screen relates the incident field $u_i(\vec{x})$ and the pupil field $u_p(\vec{x})$ by

$$u_p(\vec{x}) = u_i(\vec{x})t_s(\vec{x}), \quad (35)$$

where $t_s(\vec{x})$ is the screen transparency function, which describes the random-field perturbation. It is important to note that $t_s(\vec{x})$ in its most general form is complex and, as such, can describe both amplitude and phase perturbations. However, we restrict our attention here to pure phase effects: $t_s(\vec{x}) = \exp[i\psi(\vec{x})]$.

2. Long-exposure imaging

We analyze the performance degradations caused by atmospheric turbulence by starting with the expression for the optical transfer function (OTF) of an incoherent imaging system. The OTF can be related to the imaging-system generalized pupil function $W(\vec{x})$ by

$$\mathcal{H}(\vec{f}) = \frac{W(\vec{f}\lambda d_i) \star W(\vec{f}\lambda d_i)}{W(0) \star W(0)}, \quad (36)$$

where \vec{f} is the spatial frequency variable, λ is the mean optical wavelength, and d_i is the distance from the pupil plane to the image plane. The notation \star is the convolution operator and is defined in the following way for two arbitrary complex functions $f(\vec{x})$ and $g(\vec{x})$,

$$f(\vec{x}) \star g(\vec{x}) = \int d\vec{x}' f(\vec{x}' - \vec{x}) g^*(\vec{x}'). \quad (37)$$

To account for the wave-front phase aberrations caused by atmospheric turbulence, $W(\vec{x})$ is generalized to in-

corporate both the pupil aperture and the pupil-plane aberration. Using the screen model introduced in Sec. II.C.1, we can write the generalized pupil function as

$$W(\vec{x}) = W_p(\vec{x})t_s(\vec{x}), \quad (38)$$

where $W_p(\vec{x})$ is a real-valued function describing the pupil aperture. Substituting Eq. (38) into the expression for the OTF given in Eq. (36) gives the OTF for a realization of the turbulence-induced aberration:

$$\mathcal{H}(\vec{f}) = \frac{(W_p(\vec{f}\lambda d_i)t_s(\vec{f}\lambda d_i)) \star (W_p(\vec{f}\lambda d_i)t_s(\vec{f}\lambda d_i))}{(W(0)t_s(0)) \star (W(0)t_s(0))}. \quad (39)$$

Given the long-exposure assumption, $t_s(\vec{x})$ will evolve through many independent realizations over an exposure time. As a result it is appropriate to consider the average of Eq. (39). Taking the average of both sides of Eq. (39) while at the same time expanding the convolution operator gives

$$\langle \mathcal{H}(\vec{f}) \rangle = \Gamma_s(\lambda d_i \vec{f}) \frac{\int d\vec{x} W_p(\vec{x}) W_p(\vec{x} - \vec{f}\lambda d_i)}{\int d\vec{x} W_p^2(\vec{x})}, \quad (40)$$

where the correlation function $\Gamma_s(\Delta\vec{x}) = \langle t_s(\vec{x}) t_s^*(\vec{x} - \vec{f}\lambda d_i) \rangle$. The first factor in Eq. (40) is the atmospheric transfer function, and the second is the definition of the OTF for an unaberrated imaging system. Using the notation $\mathcal{H}_{LE}(\vec{f})$ for the long-exposure atmospheric transfer function and $\mathcal{H}_o(\vec{f})$ for the diffraction-limited OTF gives

$$\langle \mathcal{H}(\vec{f}) \rangle = \mathcal{H}_{LE}(\vec{f}) \mathcal{H}_o(\vec{f}), \quad (41)$$

where $\mathcal{H}_{LE}(\vec{f}) = \Gamma_s(\lambda d_i \vec{f})$.

3. Long-exposure atmospheric transfer function

To complete this investigation of long-exposure imaging we now make use of the phase structure function

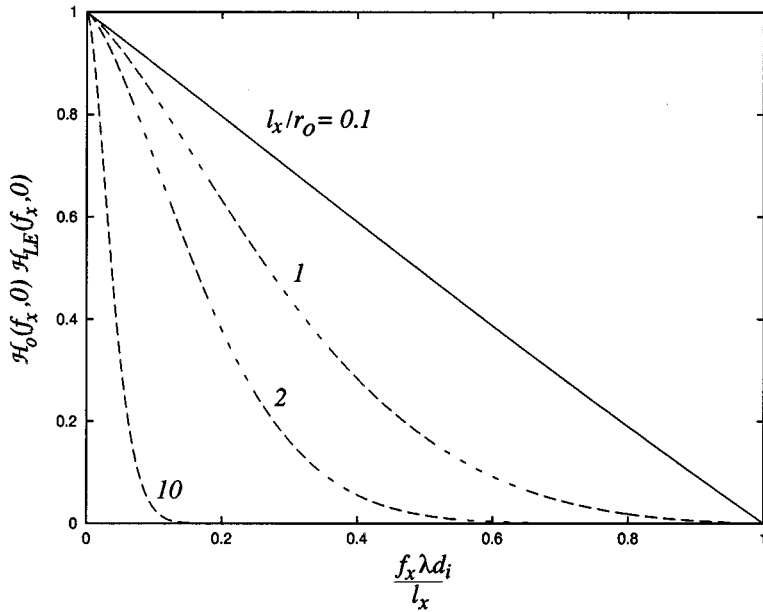


FIG. 9. Family of long-exposure optical transfer functions $\mathcal{H}_o(\vec{f})\mathcal{H}_{LE}(\vec{f})$, plotted vs the normalized spatial frequency $f_x \lambda d_i / l_x$ for a rectangular aperture of dimension $l_x \times l_y$. The ratio l_x / r_0 ranges from 0.1 to 10.

developed for wave propagation through atmospheric turbulence. Equation (27) gives the plane- and spherical-wave structure functions for wave propagation through a locally homogeneous, isotropic medium described with a Kolmogorov index-of-refraction power spectrum. Applying these results yields the well-known OTF expression developed by Fried (1966b):

$$\mathcal{H}_{LE}(\vec{f}) = \exp \left\{ -\frac{1}{2} 6.88 \left(\frac{\bar{\lambda} d_i |\vec{f}|}{r_0} \right)^{5/3} \right\}, \quad (42)$$

where r_0 is given either by the plane- or spherical-wave definitions of Eq. (25) or (28), respectively. Figure 9 shows a family of long-exposure OTF's for a rectangular aperture of dimension $l_x \times l_y$. In this figure the product $\mathcal{H}_o(\vec{f})\mathcal{H}_{LE}(\vec{f})$ is plotted along the f_x axis. The normalized aperture dimension l_x / r_0 ranges from 0.1 to 10. Notice the significant attenuation of spatial frequencies for cases in which $l_x / r_0 > 2$.

4. Short-exposure imaging

The term “short-exposure imaging” refers to the situation in which the exposure time is short enough to freeze the effects of the atmosphere. In the long-exposure discussion of the previous section the approach for analyzing imaging performance was based on the assumption that the imaging system experienced a large number of independent realizations of atmospheric-induced perturbations. In the case of short-exposure imaging the imaging system experiences one realization of atmospheric-induced perturbations. Very early it was recognized that one of the dominant effects of the atmosphere is random wave-front tilt in the pupil. The tilt is described mathematically as the vector slope of the best-fit plane to the wave-front phase $\psi(\vec{x})$. This component of the phase perturbation has the effect of shifting the

location of the image in the image plane. This random shifting of the image accounts for most of the degradations incurred for long-exposure imaging. However, the shift does not distort the short-exposure image. The short-exposure image is distorted because the wave-front tilt component is accompanied by higher-spatial-frequency perturbations. Fried (1965) has shown that tilt accounts for 87% of the power in the phase perturbations, due to the tremendous importance of the low wave numbers in the Kolmogorov spectrum. With this fact in mind, it is natural to consider what performance can be achieved for an imaging system that compensates for the random shift of the image.

The shift compensation can take two forms. In the first, the imaging system measures the wave-front tilt and adjusts, in real time, a tilt-correction mirror. In the second approach the imaging system takes short-exposure images. The short exposures freeze the effects of the turbulence-induced perturbations for each image. Each short-exposure image is subsequently recentroided electronically or processed using techniques that are insensitive to the image shifts, thereby effectively removing the image shift caused by the random tilt. The ensemble of images is then summed. The imaging performance of either one of these systems can be described with a transfer function just as in the long-exposure case. The transfer function for this type of imaging is referred to in the literature with the misnomer “short-exposure OTF.”

In order to analyze a tilt-compensating system we first need a screen model that accounts for tilt removal. We can express the tilt-removed phase screen in the following way:

$$t_s(\vec{x}) = \exp\{i(\psi(\vec{x}) - \vec{a} \cdot \vec{x})\}, \quad (43)$$

where the vector \vec{a} describes the tilt of the wave-front phase over the pupil. With the screen model of Eq. (43)

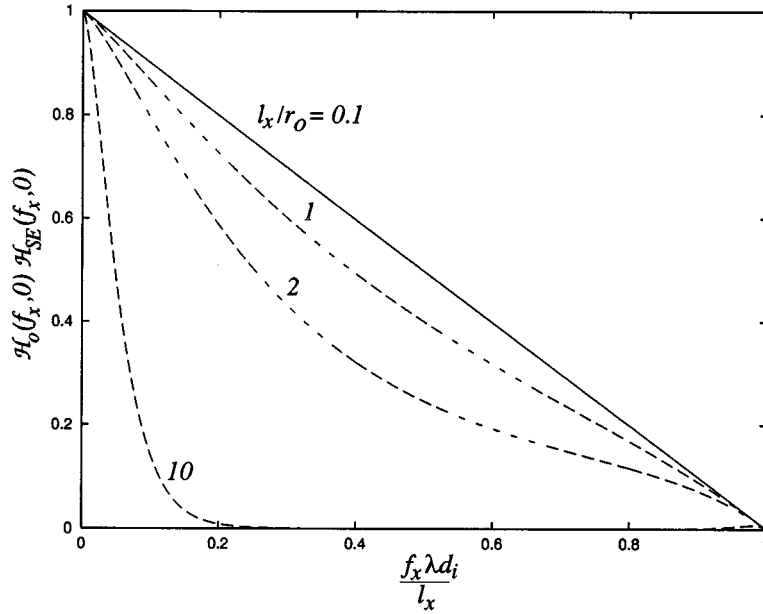


FIG. 10. Family of short-exposure optical transfer functions $\mathcal{H}_o(\vec{f})\mathcal{H}_{SE}(\vec{f})$, plotted vs the normalized spatial frequency $f_x\lambda d_i/l_x$. The ratio l_x/r_o ranges from 0.1 to 10.

we are now able to perform an analysis similar to the long-exposure OTF analysis of the previous subsection. Just as in the long-exposure case the problem reduces to the calculation of $\Gamma_s(\Delta\vec{x})$. Fried (1966b) has performed this calculation and obtained the result

$$\Gamma_s(\Delta\vec{x}) = \exp\left\{-\frac{1}{2}\left(D\psi(\Delta\vec{x}) - \frac{1}{2}|\bar{a}|^2|\Delta\vec{x}|^2\right)\right\}, \quad (44)$$

where $|\bar{a}|^2/2$ is the mean-square wave-front tilt

$$\frac{|\bar{a}|^2}{2} = 6.88r_o^{-5/3}D^{-1/3} \quad (45)$$

and D is the telescope aperture diameter. In order to obtain the result in Eq. (44) Fried assumed the residual phase after tilt removal to be uncorrelated with the tilt \bar{a} . This assumption considerably simplifies the evaluation of $\Gamma_s(\Delta\vec{x})$ but, from a mathematical viewpoint, is not valid. Fried argued on a qualitative level that the excursions of $\psi(\vec{x})$ about the tilted plane are uncorrelated with the tilt, and in reality this correlation is small for pupil sizes large with respect to r_o . Heidbreder (1967) and others (Young, 1974; Roddier, 1981; Goodman, 1985) have discussed this assumption. We use Fried's result, while recognizing that it is an approximation that improves as the aperture size increases. Substituting the expression for $D\psi(\Delta\vec{x})$ found in Eq. (27) and Eq. (45) into Eq. (44) gives the short-exposure OTF (Fried, 1966b)

$$\begin{aligned} \mathcal{H}_{SE}(\vec{f}) &= \Gamma_s(\bar{\lambda} d_i \vec{f}) \\ &= \exp\left\{-\frac{1}{2}6.88\left(\frac{|\bar{\lambda} d_i \vec{f}|}{r_o}\right)^{5/3}\left[1 - \left(\frac{|\bar{\lambda} d_i \vec{f}|}{D}\right)^{1/3}\right]\right\}. \end{aligned} \quad (46)$$

Figure 10 shows a family of short-exposure OTF's for a rectangular aperture of dimension $l_x \times l_y$. In this figure

the product $\mathcal{H}_o(\vec{f})\mathcal{H}_{SE}(\vec{f})$ is plotted along the f_x axis. The normalized aperture dimension l_x/r_o ranges from 0.1 to 10.

D. Image-detection models

In this section we present statistical models for studying the effects of measurement noise and turbulence-induced randomness in an imaging system. We adopt the linear-shift-invariant model for image formation obtained through scalar diffraction theory, as given by Goodman (1968) and Gaskill (1978),

$$i(\vec{x}) = \int d\vec{x}' h(\vec{x} - \vec{x}') o(\vec{x}'), \quad (47)$$

where \vec{x} is an image-plane coordinate, $i(\vec{x})$ is the classical intensity of the noise-free image, $h(\vec{x})$ is the response of the telescope-atmosphere system to a point source, also referred to as the point-spread function, and $o(\vec{x})$ is the image intensity predicted by geometrical optics. It should be noted that $o(\vec{x})$ differs from the intensity of the actual object only by a scaling due to magnification in a diffraction-limited imaging system. Since Eq. (47) is a convolution, we may Fourier-transform both sides to obtain (Goodman, 1968; Gaskill, 1978)

$$I(\vec{f}) = \mathcal{H}(\vec{f})O(\vec{f}), \quad (48)$$

where \vec{f} is a coordinate in the spatial-frequency domain of the image, $I(\vec{f})$ is the noise-free image spectrum, $\mathcal{H}(\vec{f})$ is the Fourier-transform of the point-spread function, also referred to as the OTF, and $O(\vec{f})$ is the object spectrum.

Note that the models given in Eqs. (47) and (48) do not account for the effects of measurement noise. However, the applications of greatest interest for many of the

imaging techniques discussed later in this paper are for exceedingly dim objects. Measurement-noise effects on the image measurement and the image reconstruction estimators are quite important under low-light-level conditions. Hence it is necessary to extend the models given in Eqs. (47) and (48) using statistical techniques to properly account for noise effects.

Photon-matter interactions that occur in light detectors are fundamentally random. Specifically, the exact location and time of a photon-absorption event in a detector cannot be predicted beforehand. This fundamental source of randomness gives rise to noise in imaging systems that is often called photon noise or shot noise. Photon noise imposes limitations on the performance of imaging systems and image reconstruction algorithms that are generally more severe than the limitations imposed by diffraction effects alone, particularly at low-light levels. Photon noise is fundamental to all photoelectric detectors and is a form of signal-dependent noise. Special methods have been developed to treat the signal-dependent nature of photon noise. We adopt the semiclassical model for photoelectric light detection in an imaging detector. The semiclassical model has the key characteristic that all propagation-related phenomena are treated with classical electromagnetic field techniques until the quantized light-matter interaction occurs at the detector surface (Goodman, 1985).

Photoelectric detectors convert an incident flux of photons into a discrete number K of photoelectrons during the measurement time τ . The mean number of photoevents \bar{K} arising during an integration time τ in some area dA of the detector is related to the classical irradiance $i(t)$ by

$$\bar{K} = \frac{\eta dA}{h\nu} \int_t^{t+\tau} dt i(t), \quad (49)$$

where t represents the independent time variable, h is Planck's constant $h = 6.626 \times 10^{-34}$ J sec, c is the speed of light, and ν is the temporal frequency of the light. The best possible detector of light allows for the direct measurement of K and the location \vec{x}_k of each photoevent. Such detectors are referred to as photon-counting or photon-limited detectors.

The random variable K strictly obeys Poisson statistics only for the case in which the image irradiance is deterministic (Kingston, 1978). Photoevents arising from an image irradiance having random variations in space or time are not strictly Poisson random processes, but rather are doubly stochastic Poisson random processes (Goodman, 1985). The random variable K is not strictly Poisson distributed in the doubly stochastic case, but is conditionally Poisson distributed, where the conditioning depends upon the instantaneous irradiance distribution during the integration time τ . Photoevents arising from an image formed with light that has passed through the atmosphere is one example of a doubly stochastic Poisson random process, since the atmosphere causes the point-spread function to be random, thereby causing the image irradiance to be random. It is possible to ob-

tain the moments of K under doubly stochastic conditions (Mandel, 1958), and this is sufficient to compute the signal-to-noise ratios of interest.

1. Poisson random processes and image estimation

In this section we introduce the mathematical properties of Poisson random processes, present a model for the detected image, obtain the Fourier transform of the detected image, and compute the mean and variance of the spectral components of the detected image for the case of a deterministic OTF. Poisson random processes have sample functions that consist of collections of Dirac delta functions. In the study of photodetection processes we associate the location of a Dirac delta function with the location of a photon absorption event. Poisson random processes are governed by a rate function, $\lambda(\vec{x})$, which has the physical interpretation that the mean number of delta functions occurring in an area $d\vec{x}$ is given by $\lambda(\vec{x})d\vec{x}$. The rate function is proportional to the classical image irradiance in an imaging system. The probability density function of the location of the n th event $p(\vec{x}_n)$, is given by

$$p(\vec{x}_n) = \frac{\lambda(\vec{x}_n)}{\int_A d\vec{x} \lambda(\vec{x})}. \quad (50)$$

The mean \bar{K} , the second moment $\overline{K^2}$, and the variance σ_K^2 of the number of delta functions occurring in the area A are given by (Goodman, 1985)

$$\bar{K} = \int_A d\vec{x} \lambda(\vec{x}), \quad (51)$$

$$\overline{K^2} = \bar{K} + (\bar{K})^2, \quad (52)$$

$$\sigma_K^2 = \overline{K^2} - (\bar{K})^2 = \bar{K}, \quad (53)$$

where the overline is also used to indicate the statistical expectation operator.

Mathematically, the detected image $d(\vec{x})$ is defined by

$$d(\vec{x}) = \sum_{n=1}^K \delta(\vec{x} - \vec{x}_n), \quad (54)$$

where \vec{x}_n is the location of the n th photoevent in the image plane and K is the total number of photoevents composing the image. The Fourier transform of $d(\vec{x})$, $D(\vec{f})$, is defined as

$$\begin{aligned} D(\vec{f}) &= \int d\vec{x} d(\vec{x}) \exp\{-i2\pi\vec{f} \cdot \vec{x}\} \\ &= \sum_{n=1}^K \exp\{-i2\pi\vec{f} \cdot \vec{x}_n\}. \end{aligned} \quad (55)$$

We now evaluate the first and second moments of $D(\vec{f})$ and the variance of $D(\vec{f})$ for the case of a fixed image irradiance $i(\vec{x})$. The random quantities in Eq. (55) are K , the total number of photoevents, and \vec{x}_n , the locations of the photoevents. Thus, to compute the first

two moments of $D(\vec{f})$, expectations over the joint distribution of \vec{x}_n and K must be computed. The required expectation for the first moment of $D(\vec{f})$ may thus be written

$$\begin{aligned} \langle D(\vec{f}) \rangle &= \left\langle \sum_{n=1}^K \exp\{-i2\pi\vec{f} \cdot \vec{x}_n\} \right\rangle \\ &= \sum_{K=0}^{\infty} \left\{ \int d\vec{x}_n \left(\sum_{n=1}^K \exp\{-i2\pi\vec{f} \cdot \vec{x}_n\} \right) p(\vec{x}_n|K) \right\} \\ &\quad \times P(K), \end{aligned} \quad (56)$$

where the joint density function of \vec{x}_n and K has been written using $p(\vec{x}_n, K) = p(\vec{x}_n|K)P(K)$. Equation (56) can be evaluated with the result (Roggemann, 1991; Roggemann and Welsh, 1996)

$$\langle D(\vec{f}) \rangle = \bar{K} \mathcal{H}(\vec{f}) O_n(\vec{f}), \quad (57)$$

where \bar{K} is the average image photocount, $\mathcal{H}(\vec{f})$ is the OTF of the optics, and $O_n(\vec{f})$ is the normalized object spectrum $O(\vec{f})/O(0)$. The second moment $\langle |D(\vec{f})|^2 \rangle$ is evaluated using the same method established in Eq. (56) and is given by (Roggemann, 1991; Roggemann and Welsh, 1996)

$$\langle |D(\vec{f})|^2 \rangle = \bar{K} + (\bar{K})^2 |\mathcal{H}(\vec{f}) O_n(\vec{f})|^2. \quad (58)$$

The variance of $D(\vec{f})$, $\text{var}\{D(\vec{f})\}$, is obtained from its first and second moments by

$$\text{var}\{D(\vec{f})\} = \langle |D(\vec{f})|^2 \rangle - \langle |D(\vec{f})| \rangle^2 = \bar{K}. \quad (59)$$

Note that while the first and second moments of $D(\vec{f})$ depend upon $\mathcal{H}(\vec{f})$ and $O_n(\vec{f})$, the variance of $D(\vec{f})$ depends only upon \bar{K} for the case of a deterministic OTF and a fixed object.

2. Spatial-frequency-domain signal-to-noise ratio

In this subsection we define and derive the signal-to-noise ratio (SNR) of $D(\vec{f})$. A model for additive noise is also introduced, and the effects of additive noise on the SNR of $D(\vec{f})$ are analyzed. The SNR of $D(\vec{f})$ is defined (Idell and Webster, 1992) as

$$\text{SNR}_D(\vec{f}) = \frac{|\langle D(\vec{f}) \rangle|}{[\text{var}\{D(\vec{f})\}]^{1/2}} \quad (60)$$

and is referred to as the image-spectrum SNR. The image reconstruction techniques presented later in this paper use spatial-frequency-domain methods to obtain estimates of object irradiance distributions from blurred and noisy images. $\text{SNR}_D(\vec{f})$ is now derived for the case of a fixed OTF and photon-limited detection.

Using the results obtained in Eqs. (57) and (59), one finds the SNR of an image obtained with a deterministic OTF and a photon-limited image detection system,

$$\text{SNR}_D(\vec{f}) = \bar{K}^{1/2} |\mathcal{H}(\vec{f}) O_n(\vec{f})|. \quad (61)$$

The following observations can be made regarding Eq. (61): (1) increasing the mean number of photoevents always improves $\text{SNR}_D(\vec{f})$; (2) $\text{SNR}_D(\vec{f})$ goes to zero at a spatial frequency no higher than the diffraction-limited cutoff of the optics, since $\mathcal{H}(\vec{f})$ goes to zero there; (3) aberrations, which generally broaden the point-spread function of the optics and narrow $\mathcal{H}(\vec{f})$, have the effect of lowering $\text{SNR}_D(\vec{f})$; (4) for irradiance images $\text{SNR}_D(\vec{f})$ takes its maximum value at $\vec{f}=0$ and tends to decrease with increasing spatial frequency because the modulus of the OTF, $|\mathcal{H}(\vec{f})|$, and the modulus of the normalized object spectrum, $|O_n(\vec{f})|$, tend to decrease with increasing $|\vec{f}|$.

Additive noise is present in many imaging detectors used in practice and has the effect of reducing the image-spectrum SNR. Additive noise is distinct from photon noise in that additive noise is statistically independent of the signal, while photon noise is signal dependent. Further, the physical origin of additive noise is generally associated with the detector material and the readout electronics, while the source of photon noise is the quantized nature of light-matter interactions. We now introduce the model for the detected image containing additive noise and analyze the effects of this noise on $\text{SNR}_D(\vec{f})$. The model for a detected image with additive noise is given by

$$d(\vec{x}) = \sum_{n=1}^K \delta(\vec{x} - \vec{x}_n) + \sum_{p=1}^P n_p \delta(\vec{x} - \vec{x}_p), \quad (62)$$

where \vec{x}_p is the location of the p th pixel in the image, n_p is a random variable representing the amount of additive noise at the p th pixel in units of photoevents, and P is the total number of pixels in the image. The first term in Eq. (62) describes the photon-limited image, and the second term describes the additive noise. The random variable n_p is assumed to have the following properties: (1) $\langle n_p \rangle = 0$; (2) $\langle n_p n_{p'} \rangle = 0$ if $p \neq p'$; (3) $\langle n_p n_{p'} \rangle = \sigma_n^2$ if $p = p'$; and (4) n_p is statistically independent of K and \vec{x}_n . For example, the output of widely used charge-coupled-device (CCD) detectors is corrupted with additive noise commonly referred to as read noise. Read noise in CCD's is specified in root-mean-square (rms) electrons per pixel per readout, which is exactly the standard deviation of n_p , σ_n . It is easy to show that additive noise does not affect the mean value of the image spectrum. Hence the expression for $\langle D(\vec{f}) \rangle$ given in Eq. (57) is valid for this case. The additive-noise terms in $D(\vec{f})$ are zero mean, uncorrelated, and statistically independent of the photon-limited detection term. Hence additive noise increases the second moment of $D(\vec{f})$ by the amount

$$\left\langle \left| \sum_{p=1}^P n_p \exp\{-i2\pi\vec{f} \cdot \vec{x}_p\} \right|^2 \right\rangle = P \sigma_n^2. \quad (63)$$

The variance of $D(\vec{f})$ is obtained with reference to Eq. (59) and is given by

$$\text{var}\{D(\vec{f})\} = \bar{K} + P\sigma_n^2, \quad (64)$$

so that the image-spectrum SNR corrupted with additive noise is given by

$$\text{SNR}_D(\vec{f}) = \frac{\bar{K} |\mathcal{H}(\vec{f}) O_n(\vec{f})|}{(\bar{K} + P\sigma_n^2)^{1/2}}. \quad (65)$$

3. Doubly stochastic Poisson random processes

Up to now we have discussed only the effects on the detected-image spectrum of randomness arising from the random locations of photoevents, the random number of photoevents, and additive noise in the image measurement. An additional source of randomness arises from atmospheric turbulence—specifically, the point-spread function, and hence the OTF, is random due to atmospheric-turbulence effects. Poisson random processes that have random rate functions are referred to as doubly stochastic Poisson random processes. In this section we analyze the effects of a random OTF on the mean, second moment, and variance of $D(\vec{f})$.

To evaluate the mean of $D(\vec{f})$ the method of Eq. (56) is extended to account for the randomness of $\mathcal{H}(\vec{f})$ with the addition of an outer expectation over all possible realizations of $\mathcal{H}(\vec{f})$. These expectations can be performed to obtain (Roggemann, 1991)

$$\langle D(\vec{f}) \rangle = \bar{K} \langle \mathcal{H}(\vec{f}) \rangle O_n(\vec{f}). \quad (66)$$

The second moment of $D(\vec{f})$ can also be evaluated with the result

$$\langle |D(\vec{f})|^2 \rangle = \bar{K} + (\bar{K})^2 \langle |\mathcal{H}(\vec{f})|^2 \rangle |O_n(\vec{f})|^2. \quad (67)$$

The variance of $D(\vec{f})$ is determined from the first and second moments of $D(\vec{f})$ to be

$$\begin{aligned} \text{var}\{D(\vec{f})\} &= \langle |D(\vec{f})|^2 \rangle - \langle D(\vec{f}) \rangle^2 \\ &= \bar{K} + (\bar{K})^2 |O_n(\vec{f})|^2 \text{var}\{\mathcal{H}(\vec{f})\}. \end{aligned} \quad (68)$$

The first term in Eq. (68) is due to Poisson noise, and the second term is due to randomness in the OTF. These effects combine to increase the total variance of $D(\vec{f})$ compared to the fixed-OTF case.

The image-spectrum SNR for an image measured under conditions of a doubly stochastic Poisson random process is thus given by

$$\text{SNR}_D(\vec{f}) = \frac{\bar{K} |\langle \mathcal{H}(\vec{f}) \rangle| |O_n(\vec{f})|}{\sqrt{\bar{K} + (\bar{K})^2 |O_n(\vec{f})|^2 \text{var}\{\mathcal{H}(\vec{f})\}}}. \quad (69)$$

If additive noise is present in the image measurement as defined in Eq. (62), then the variance of $D(\vec{f})$ is increased by the amount $P\sigma_n^2$, where P is the number of pixels in the image and σ_n^2 is the additive-noise variance in photoelectrons per pixel per readout. Two observations are in order regarding Eq. (69): (1) the effect of random fluctuations in the OTF lowers the SNR of the image spectrum; and (2) increasing the average number

of photoevents in the image cannot overcome the effects of randomness in the OTF. In fact, the $\bar{K} \rightarrow \infty$ limit of Eq. (69) is

$$\lim_{\bar{K} \rightarrow \infty} \{\text{SNR}_D(\vec{f})\} = \frac{|\langle \mathcal{H}(\vec{f}) \rangle|}{\sqrt{\text{var}\{\mathcal{H}(\vec{f})\}}} = \text{SNR}_{\mathcal{H}}(\vec{f}), \quad (70)$$

where $\text{SNR}_{\mathcal{H}}(\vec{f})$ is referred to as the SNR of the random OTF.

III. ADAPTIVE OPTICAL IMAGING SYSTEMS

It is clear from the discussion presented in Secs. I and II that wave-front field aberrations induced by atmospheric turbulence can severely degrade the performance of an optical imaging system. Atmospheric turbulence so limits ground-based imaging that the best observatories in the world only achieve resolutions associated with diffraction-limited apertures of 10 to 30 cm. Babcock (1953) was the first to propose that imaging-system performance could be improved by flattening the perturbed wave front in the pupil of the imaging system. Babcock's idea is the foundation for all active and adaptive optics used to compensate for atmospheric turbulence. Systems using adaptive optics are commonly called adaptive optical imaging (AOI) systems. AOI systems must perform two main functions: (1) sense the wave-front perturbations and (2) compensate for them in real time.

The components required to perform the two functions are shown in Fig. 11. These components include the deformable mirror (DM), the wave-front sensor (WFS), and an actuator command computer. Aberrated light entering the telescope is first reflected from the deformable mirror. Some of this light is focused to form an image, and some is diverted to the wave-front sensor. The wave-front sensor measures the residual error in the wave front and provides this information to the actuator control computer, which computes the deformable-mirror actuator voltages. The entire process, from the acquisition of a wave-front sensor measurement to the positioning of the surface of the deformable mirror, must be performed at speeds commensurate with the rate of change of the turbulence-induced wave-front phase errors. The goal in the positioning of the deformable-mirror surface is to present an approximation of the conjugate of the turbulence-induced field so that the field reflected from the deformable mirror will more closely approximate the field that would exist in the absence of atmospheric turbulence.

The deformable mirror is a flexible mirror whose surface shape can be modified at high speed in response to applied electrical signals. Its surface is controlled in such a way as to cancel the atmospheric-induced wave-front phase aberration in the pupil. The mirror surface or figure is controlled by a number of actuators that push and pull on the mirror surface to cause it to deform. The wave-front sensor measures the wave-front phase perturbations; however, it does not do so directly. Rather, wave-front sensors are generally sensitive to the wave-

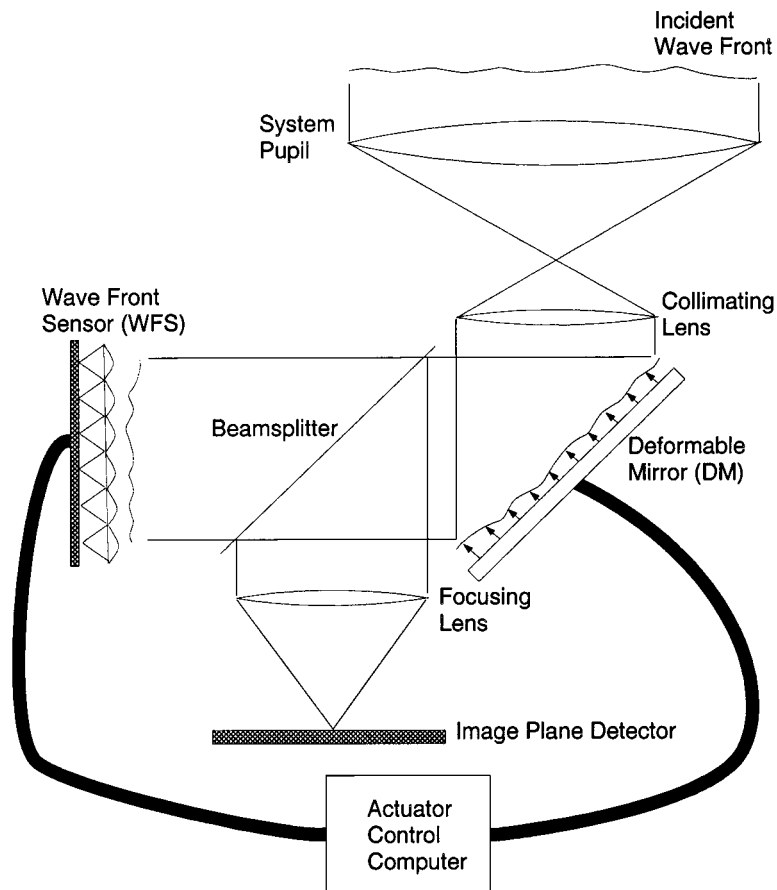


FIG. 11. Simplified optical configuration of an adaptive optical imaging system.

front phase gradient. The wave-front phase is obtained by using the measured wave-front gradient in a phase-reconstruction algorithm. The deformable mirror and wave-front sensor are connected through the actuator command computer. The purpose of the control computer is to take measurements from the wave-front sensor and map them into real-time control signals for the deformable mirror. The command computer basically strives to achieve wave-front reconstruction by controlling the surface of the deformable mirror.

If the adaptive optical concepts discussed above worked perfectly, the adaptive optical imaging system would achieve the ideal performance limit: diffraction-limited imaging. In this case the imaging system would operate as if in an aberration-free environment, and only diffraction effects would limit performance. Theoretical and experimental (Fugate *et al.*, 1994) evidence has shown that true diffraction-limited performance is impossible to achieve. The actual performance of an adaptive optical imaging system may encompass the entire range from nearly no improvement to performance having characteristics of nearly diffraction-limited imagery. Evaluating the expected performance of adaptive optical imaging systems has been the subject of a large amount of research over the past 20 years (Fried, 1966a, 1977, 1982, 1990a, 1994a, 1994b; Noll, 1976; Greenwood, 1977, 1979; Hudgin, 1977a, 1977b; Hardy, 1978; Wang and Markey, 1978; Southwell, 1980; Wallner, 1983; Petersen and Cho, 1986; Gaffard and Boyer, 1987; Nissen and Barakat, 1987; Smithson *et al.*, 1988; Downie

and Goodman, 1989; Smithson and Peri, 1989; Welsh and Gardner, 1989, 1991; Gardner *et al.*, 1990; Roggemann, 1991, 1992; Welsh, 1991, 1992; Herrmann, 1992; Johnston and Welsh, 1982, 1994; Roggemann and Matson, 1992; Roggemann *et al.*, 1992; Beckers, 1993; Rigaut and Gendron, 1993; Roggemann and Meinhardt, 1993; Tyler, 1993, 1994a, 1994b; Demerlé *et al.*, 1994; Ellerbrock, 1994; Ellerbroek *et al.*, 1994; Gavel *et al.*, 1994; Parenti and Sasiela, 1994; Welsh and Roggemann, 1994a).

Before discussing the components and performance analysis of adaptive optical imaging systems we first present, in Sec. III.A, a qualitative discussion of the factors that fundamentally limit adaptive optical imaging system performance. In Sec. III.B we present a brief introduction to the components that make up the typical adaptive optical imaging system. Section III.C. ends with a discussion of a number of fundamental and system-performance results.

A. Factors that degrade adaptive optical imaging system performance

An ideal adaptive optical imaging system is one that perfectly senses and compensates for the atmospherically induced wave-front perturbations. Due to the large number of factors that contribute to the degradation of adaptive optical imaging system, our discussion will be confined to those that represent the most fundamental

and limiting factors in any system. These fundamental factors include finite light levels in the wave-front sensors, differences between the sensed and object wave fronts associated with anisoplanatism, finite spatial sampling of the wave-front sensor, finite number of degrees of freedom available from the deformable mirror, and the finite temporal response of the adaptive optical imaging system.

1. Wave-front sensor light levels and anisoplanatism

The finite amount of light in the wave-front sensor and anisoplanatism may well represent the most severe of all factors that degrade adaptive optical imaging system performance. These two factors are discussed together because they are inextricably tied to each other in the case of telescopes used for astronomical purposes. In most of the adaptive-optics systems built to date, light from either the object being imaged or a nearby “beacon” source is used to provide light for the wave-front sensor. In either case the finite light level available to the wave-front sensor can severely limit the accuracy of the wave-front sensing. Inaccurate wave-front sensing leads to inaccurate wave-front reconstruction, which degrades adaptive optical imaging system performance significantly below the theoretical limit. The problem of obtaining enough light for accurate wave-front sensing has been the most significant factor limiting the application of adaptive-optics technology to ground-based astronomy. Until recently, adaptive optics have generally not been applied to ground-based astronomical telescopes because of the inability to obtain bright beacon sources over any significant portion of the night sky. Only recently have we seen applications of adaptive optics to near-infrared imaging, where bright beacon stars are available. This recent development for near-infrared imaging can be attributed to improved near-infrared cameras and more sensitive wave-front detectors. The problem lies in the fact that in most instances the object being imaged is itself not bright enough to be used by the wave-front sensor. As a result, a nearby beacon source must be found to provide the light for the wave-front sensor. In the case of astronomy, this nearby beacon is generally a nearby bright star, sometimes referred to as a guide star. If finding the closest bright beacon were the only problem to overcome, then adaptive optics would have been successfully used in astronomy years ago. Unfortunately simply finding the nearest bright beacon star is not adequate unless it lies within the isoplanatic angle of the object being imaged.

The isoplanatic angle is qualitatively the maximum angular separation between the object and the beacon such that the turbulence-induced wave-front perturbations for the object and beacon wave fronts are still reasonably similar. In order to understand the implication of the isoplanatic angle, recall that the light from the beacon is used to sense the perturbed wave front and this information is in turn used to compensate for distortions in the object wave front. If the beacon is separated from the object, the two wave fronts propagate through

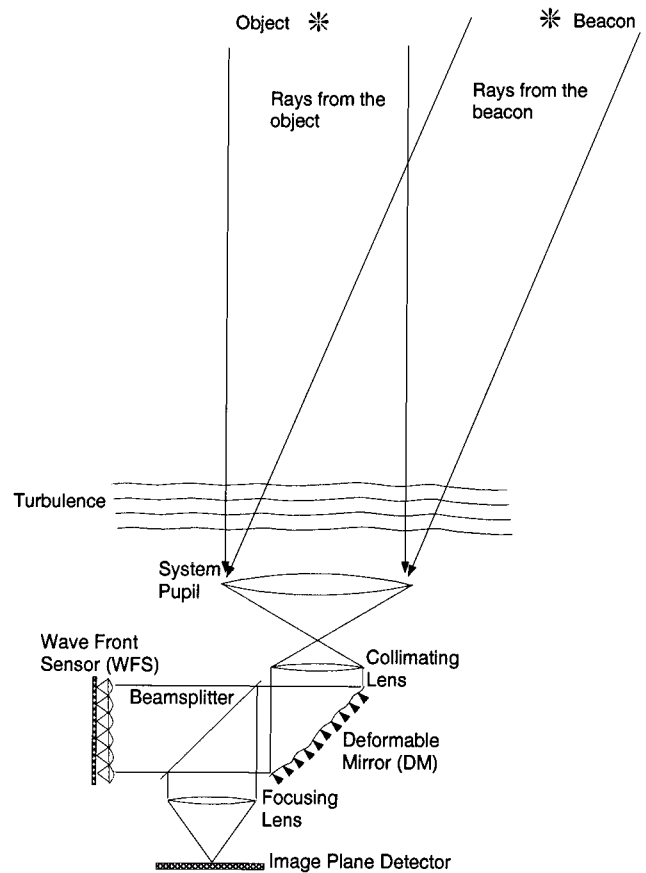


FIG. 12. Angular anisoplanatism.

slightly different regions in the atmosphere, as shown in Fig. 12. This difference in propagation path results in slightly different wave-front perturbations induced on the two wave fronts. This effect is referred to as an anisoplanatic effect. Besides finite light levels in the wave-front sensor, anisoplanatism represents the other major factor that causes an adaptive optical imaging system to perform in a less than ideal way. In fact, as seen in the discussion above, light levels in the wave-front sensor and anisoplanatism are inextricably tied together, since it is anisoplanatism that prevents the adaptive optical imaging system from using nearby bright guide stars.

The isoplanatic angle has been defined quantitatively as the largest angle separation between the object and beacon such that some measure of imaging performance is kept within a specified level. The isoplanatic angle is very small for astronomical observations in the visible wavelength range. At visible wavelengths the object being imaged has to be within 5 to 10 μrad of the beacon. This restriction on the angular separation of the object and beacon implies that the percentage of the night sky accessible using the naturally occurring bright stars is essentially zero (Gardner *et al.*, 1990). The outlook is more optimistic at infrared wavelengths, where the isoplanatic angle is considerably larger (100's of μrad). This trend with respect to wavelength is understood when considering the isoplanatic angle defined by Fried (1982):

$$\theta_0 = 58.1 \times 10^{-3} \left[\frac{\lambda^2}{\int_0^L dz C_n^2(z) z^{5/3}} \right]^{3/5}. \quad (71)$$

In this definition the isoplanatic angle has a wavelength dependence that is identical to the dependence found for the Fried parameter r_0 . The isoplanatic angle and r_0 are proportional to $\lambda^{6/5}$ [see Eq. (25)]. In applications involving long wavelengths (such as infrared astronomy), r_0 and θ_0 increase from the small values they take at visible wavelengths. This increase allows the subapertures of the wave-front sensor to be larger than those required for visible wavelengths. Dimmer beacons can thus be used as the subapertures of the wave-front sensor become larger. This decreasing brightness requirement in combination with an increased isoplanatic angle size gives rise to a situation in which infrared astronomy using natural stars is possible. Studies of the applications of adaptive optics to infrared astronomy have shown that there are enough bright guide stars to access nearly 100% of the night sky. In fact, the first applications of adaptive optics to astronomy have been for infrared systems (Thompson, 1994). The isoplanatic angle defined above is derived for near-field atmospheric conditions. The effects of anisoplanatism have also been investigated for far-field turbulence effects using a more rigorous diffraction analysis (Troxel *et al.*, 1994, 1995).

A possible solution to the problems associated with anisoplanatism is the creation of an artificial beacon using a laser to project a spot in the atmosphere above the telescope (Gardner *et al.*, 1990). Foy and Labeyrie (1985) were the first to suggest in the open literature that it may be possible to create a suitable artificial guide star in the upper atmosphere with a laser. Within the United States' Defense Advanced Research Projects Agency the idea was being considered as early as 1982 (Happer *et al.*, 1994). Artificial guide stars allow access to nearly the entire sky even at visible wavelengths, since the laser can be pointed in any direction. The transmitted laser beam is focused to a spot in the center of the field of view of the telescope at a finite altitude above the telescope. Within the region where the beam is focused, some of the light is scattered from the atmospheric constituents, and some of this scattered light is returned in the direction of the telescope. The backscattered light is used by the wave-front sensor to measure turbulence-induced aberrations. The laser spot is referred to as a laser beacon or artificial guide star. Ideally the use of laser beacons removes the fundamental problem of low light levels in the wave-front sensor since the brightness of the beacon is controlled by the laser power.

The problem associated with the angular anisoplanatic effects discussed above is seemingly solved with the use of laser beacons. The laser beacon can be placed in exactly the same angular direction as the object, thereby forcing the beacon and object wave fronts to arise from the same angular point in the sky. Another anisoplanatic effect arises with the use of laser beacons that is slightly different in nature from the angular

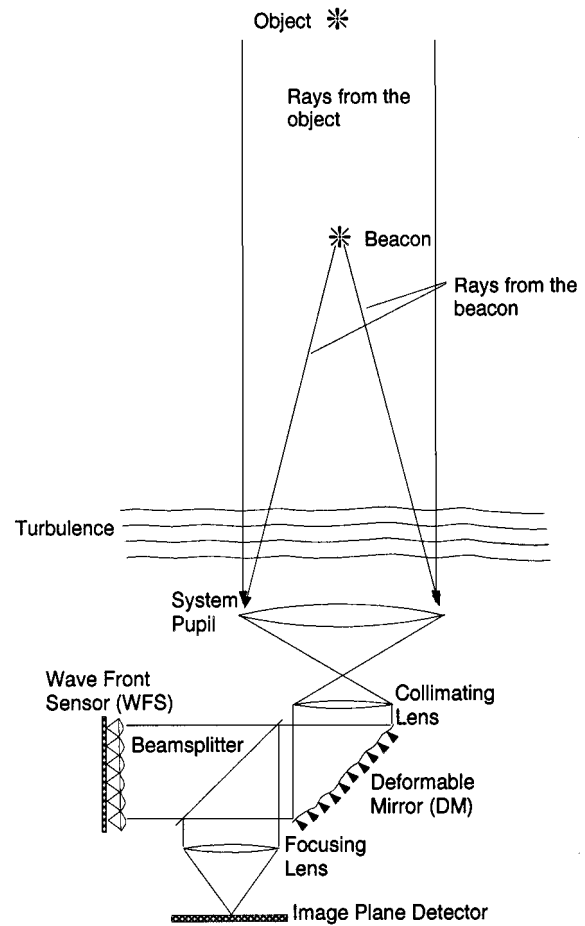


FIG. 13. Cone effect.

anisoplanatism discussed above. With the use of laser beacons the adaptive optical imaging system suffers from a fundamental anisoplanatic effect known as the cone effect (also referred to as focus anisoplanatism). The cone effect arises from the fact that the light emitted from the laser beacon is a spherical wave emitted from a finite-altitude source. Figure 13 shows the geometry of interest. Since the object wave front generally arises from a source a very large distance away (as is the case for celestial bodies), it is well modeled as a plane wave. The difference between plane- and spherical-wave propagation results in an anisoplanatic effect that is again due to the two wave fronts' propagating through different regions of the turbulence as shown in Fig. 13. The difference in the propagation paths increases as the diameter of the telescope increases. So, even with the use of a bright laser beacon, the adaptive optical imaging system will still be fundamentally limited by the cone effect. The cone effect can be lessened by placing the laser beacon at the highest possible altitude. The two main approaches for the generation of laser beacons involve the use of Rayleigh scattering in the stratosphere and the use of resonance fluorescence of sodium (Na) atoms in the mesosphere (Gardner *et al.*, 1990). Beacons employing Rayleigh scattering are called Rayleigh beacons, while guide stars employing Na resonance fluorescence are called Na beacons. The advantage of using a

Rayleigh beacon is that lasers with many of the required characteristics can already be purchased commercially. In particular, the power required to create sufficiently bright Rayleigh guide stars is available with “off-the-shelf” lasers (Gardner *et al.*, 1990; Thompson, 1994). Rayleigh guide stars are most efficiently created at relatively low altitudes, ranging from 10 to 20 km. Na beacons, on the other hand, are formed in a naturally occurring layer of Na in the mesosphere. The Na layer is located at an altitude of approximately 90 km (Gardner, 1989). Since Na beacons are created at a much higher altitude than Rayleigh beacons, the cone effect is much less severe for Na beacons. The cone effect is significant enough that Na laser beacons are the preferred approach, assuming availability of a laser to produce them. However, to date, only expensive special-purpose lasers have succeeded in creating sufficiently bright Na beacons (Collins, 1992; Fugate, 1993).

In addition to the cone effect, an adaptive optical imaging system employing an artificial beacon also suffers from a form of angular anisoplanatism. This fact may seem counterintuitive, since the whole point of creating a laser beacon is that it can be placed at the same angular position as the object, thereby avoiding the angular anisoplanatism discussed earlier. Unfortunately, though, in the upward projection of the laser beacon the exact position of the focused spot cannot be determined. The laser-beacon optical field propagates up through turbulence before being focused into a spot. The upward propagation through the turbulence causes the angular position of the beacon to shift randomly, and the random motion denies the adaptive optical imaging system exact knowledge of the position of the beacon. Without this knowledge the adaptive optical imaging system cannot reliably use the laser beacon to predict the wave-front tilt. Wave-front tilt refers to the portion of the wave-front perturbation that corresponds to the best-fit plane over the aperture of the system. The wave-front tilt induced on the beacon field is caused by both the turbulence for the downward propagation and the motion of the beacon (i.e., the turbulence in the upward propagation). Since the beacon motion is random and unknown, it is impossible to measure the portion of the wave-front tilt induced by downward propagation through the atmosphere. The insensitivity to wave-front tilt for an artificial beacon implies the adaptive optical imaging system must employ another beacon with a fixed location in the sky (i.e., a natural star) for sensing and compensation of overall wave-front tilt.

This last statement may make it appear that we are right back where we started when we introduced the use of laser beacons to solve the angular anisoplanatism problem. Fortunately, the natural star is only needed for sensing the portion of the perturbed wave front associated with wave-front tilt. The isoplanatic angle for sensing and correcting the tilt aberration is much larger than the isoplanatic angle associated with sensing and correcting higher-order perturbations (Gardner *et al.*, 1990). The isoplanatic angle associated with tilt correction is defined in relation to the wave-front error in-

duced by the tilt. In other words, the angular separation between the natural beacon for tilt sensing and the object can be much larger. This angular limit is called the tilt isoplanatic angle. Additionally, the temporal bandwidth requirement for compensating for the tilt is less stringent than compensation of the higher-order wave-front aberrations (Rodier *et al.*, 1993). This fact, along with the larger tilt isoplanatic angle, makes obtaining natural stars for tilt sensing not nearly so severe a limitation as obtaining natural stars for use in compensating the higher-order wave-front perturbations. The effects of tilt anisoplanatism can be decreased by decreasing the angular separation of the natural guide star and the direction to the object. Rigaut and Gendron (1993) have analyzed the sky coverage for adaptive optical imaging systems using natural guide stars for tilt correction and found a 1.0% coverage at visible wavelengths, which increases to nearly 100% coverage at infrared wavelengths (3 μm).

Finally, it is also worth noting that the performance of the overall tilt correction has a profound effect on the performance of the system (Rigaut and Gendron, 1993). Eighty-seven percent of the power in the aperture averaged mean-square wave-front fluctuations is due to the full-aperture wave-front tilt. Since such a large portion of the wave-front aberrations is associated with wave-front tilt, tilt correction is critical for effective adaptive optical imaging system performance. Any correction of these higher-order aberrations will be swamped by uncorrected tilt if the system suffers from poor tilt correction. The brightness and angular separation of the tilt guide star contributes significantly to the limiting performance of an adaptive optical imaging system.

2. Finite pupil sampling of the wave-front sensor, limited number of degrees of freedom of the deformable mirror, and finite system temporal response

The last three performance limitations presented in the list at the beginning of Sec. III.A are grouped together, since they arise from fundamental limitations of the components of the adaptive optical imaging system itself. Both the finite spatial sampling of the wave-front sensor and the finite degrees of freedom of the deformable mirror result in the same general type of system performance degradation. The finite sampling and the finite degrees of freedom can both be viewed as degrading the system's ability to sense and compensate for the high spatial frequencies or higher-order modes of the wave-front perturbations. The inherent finite sampling of wave-front sensors makes them unsuitable for sensing perturbations having spatial frequencies beyond some upper frequency cutoff. The cutoff frequency of the wave-front sensor is inversely proportional to its sample spacing. Aliasing of high-spatial-frequency perturbations into lower frequencies is a fundamental problem encountered with finite sampling. The finite number of degrees of freedom of the deformable mirror acts like a spatial filter that limits the spatial frequency content of the reconstructed wave-front phase. Just as for the

wave-front sensor, the cutoff frequency of the deformable mirror is inversely proportional to the spacing of the actuators that deform the surface of the mirror.

The performance degradation imposed by the deformable mirror and wave-front sensor can be lessened by using wave-front sensors with smaller sample spacing and deformable mirrors with more actuators (i.e., more closely spaced actuators). The general rule of thumb for “good” wave-front compensation is to design the adaptive optical imaging system with subaperture and actuator spacings $\sim r_0$, where r_0 is the previously defined Fried parameter. An adaptive optical imaging system satisfying this condition is generally referred to as a fully compensated system.

Improving upon the performance limitations imposed by the subaperture size of the wave-front sensor and the interactor spacing of the deformable mirror involves using smaller subapertures and smaller interactor spacings. This approach is generally expensive in both hardware complexity and cost. The controller in an adaptive optical imaging system must map many wave-front sensor measurements to many deformable-mirror actuator control signals. Decreasing the subaperture size and actuator spacing increases the complexity and speed requirement of the system controller. The adaptive optical imaging system must sense and compensate for wave-front perturbations at speeds commensurate with the coherence time of the atmosphere. At good observatory sites the coherence time will be on the order of 10 milliseconds (Gardner *et al.*, 1990). The large number of subapertures and deformable-mirror DM actuators for densely sampled pupils may well push the temporal bandwidth limits of a multiple-input/output controller beyond the capability of widely available and affordable technology. In general, large adaptive telescopes, such as 2-m-diameter and larger telescopes, have been designed with subaperture sizes and interactor spacings larger than r_0 .

Adaptive optical systems having subaperture sizes and interactor spacings larger than r_0 are generally referred to as partially compensated systems. These systems have the advantage that they are less expensive and less complex than fully compensated systems, but they suffer in performance due to the sampling issues discussed above. However, it has been shown recently (Roggemann, 1992) that partially compensated adaptive optical imaging systems do not suffer as much in a signal-to-noise ratio (SNR) sense as might be expected. Even though average performance measures, such as the mean-square residual phase fluctuation, degrade for systems employing partial compensation, it has been shown that the image-spectrum SNR does not degrade as rapidly (Roggemann, 1992). This observation has opened up possibilities of using the post-processing image-reconstruction techniques discussed in Secs. VI and VII to achieve close to the same image qualities as a fully compensated adaptive optical imaging system.

Another possible reason for employing a partially compensated adaptive optical imaging system is the effect of finite light levels on the wave-front sensor. For a

fixed photon-flux level there will be an optimal wave-front sensor subaperture size that minimizes the residual wave-front phase fluctuations (Welsh, 1991). Depending on the light level expected for the wave-front sensor, this optimum subaperture size may result in a partially compensated system. The optimum subaperture size exists because of the competing trends in the two main contributions to the wave-front compensation errors. As the subaperture size of the wave-front sensor decreases, the errors associated with finite sampling decrease. On the other hand, the decreasing size causes each subaperture to intercept less light, and as a result the slope measurements become noisier. An alternate approach to adjusting for the optimal subaperture size is the development of an optimal deformable-mirror control algorithm. Deformable-mirror control algorithms can be derived to minimize wave-front error, given statistical knowledge of the wave-front sensor noise and atmospheric wave-front perturbations (Wang and Markey, 1978; Herrmann, 1981; Wallner, 1983; Welsh and Gardner, 1989; Ellerbroek, 1994; Gendron and Lena, 1994; Cannon, 1995; Dai, 1995; Roggemann and Welsh, 1996).

The temporal evolution of the turbulence-induced wave-front perturbations, in combination with the adaptive optical imaging system’s finite temporal response, fundamentally limits performance. In simple terms, the adaptive optical imaging system takes a finite amount of time from wave-front sensing to wave-front correction. This time delay causes a degradation in performance. The atmospheric correlation time τ_c is generally used to characterize the rate at which the wave-front perturbations are changing. The inverse of τ_c is commonly used to specify the required temporal bandwidth of the AOI system. The temporal bandwidth requirement and light levels in the wave-front sensor are inextricably linked from an overall performance perspective. The temporal bandwidth required to keep up with the temporally evolving wave-front perturbations control the rate at which wave-front measurements must be taken. A wave-front sensor measurement rate implies a maximum integration time for each measurement. For a fixed photon flux the integration time controls the average number of photoevents detected per measurement cycle. Just as we saw for the subaperture size, we see that competing trends will result in an optimum control bandwidth. Increasing the system bandwidth will decrease the errors associated with temporally evolving wave fronts. At the same time, increasing bandwidth decreases the number of photoevents detected per wave-front sensor measurement, which results in noisier wave-front slope measurements. Optimal wave-front control algorithms can also be derived to perform temporal wave-front control (Welsh and Gardner, 1989; Ellerbroek *et al.*, 1994; Conan *et al.*, 1995; Wild *et al.*, 1995).

B. Adaptive optical system components

In the following subsections we present an introductory discussion of the three main components of an adaptive optical imaging system: the deformable mirror,

the wave-front sensor, and the controller. The purpose of this introduction is to provide an overall view of the performance issues associated with the components.

1. Deformable mirrors

The deformable mirror is the system component that performs the wave-front correction. The shape of its surface (or figure) is controlled such that perturbations of the incident wave front are cancelled as the optical field reflects from the surface. In an ideal adaptive optical imaging system the figure of the deformable mirror and the perturbed wave front cancel exactly, and the residual wave-front phase is zero. Previously we discussed the factors that prevent adaptive optical imaging systems from achieving ideal performance. The performance of the deformable mirror is limited by the finite degrees of freedom associated with controlling the figure of the mirror and the finite temporal response. The finite degrees of freedom restrict the range of surface shapes that can be placed on the deformable mirror.

The temporal response of the deformable mirror characterizes how its surface responds temporally to an instantaneous command. Both the speed of the response (i.e., how fast the surface moves to the desired shape) and resonances are of interest. The state of current deformable-mirror design is such that these temporal concerns are not major considerations for ground-based imaging up through the atmosphere. Deformable mirrors are being designed to have bandwidths on the order of a kilohertz or greater and resonances well outside the operation range of interest (Hardy, 1978; Ealey and Washeba, 1990). This bandwidth easily meets the requirements associated with the temporal rates required for atmospheric compensation: several hundred Hertz (Hardy, 1978). For more comprehensive discussions of the characteristics and limitations of the various types of deformable mirrors, see Hardy (1978), Tyson (1991), and Ribak (1994).

a. Segmented and continuous deformable mirrors

There are two broad classes of deformable mirrors, categorized by the nature of the mirror surface: segmented or continuous. The surface of a segmented deformable mirror is controlled by positioning a number of independently controlled, closely packed, flat mirror segments, which can be moved individually either by piston only or by piston plus tilt. The advantages associated with segmented deformable mirrors are the modularity and simplicity of the design. Modularity makes it possible to combine rectangular arrays of mirror segments to form larger deformable mirrors. The simplicity allows individual segments to be easily replaced. Another advantage associated with segmented mirrors is the conceptually simple control requirements (Ribak, 1994). Disadvantages include diffraction effects from the individual segment edges and the difficulty of achieving intersegment alignment. An example of an adaptive optical imaging system using a segmented mirror is described by Acton and Smithson (1992).

The disadvantages associated with segmented deformable mirrors are largely addressed by continuous deformable mirrors. The continuous deformable mirror has a single continuous mirror surface, usually called the face plate or face sheet. The shape of the mirror surface is controlled by an array of actuators that push, pull, and bend the face sheet to obtain the desired figure. There are two main types of continuous mirror actuation: piston actuation and bending actuation (Ribak, 1994). For piston actuation the force applied to the mirror surface is applied perpendicular to the nominal (or resting) mirror surface. The actuator pushes or pulls on the mirror surface to deform it into the desired shape. For bending actuation the mirror is placed under a bending force that changes the curvature of the surface. Bimorph mirrors (Kokorowski, 1979; Steinhaus and Lipson, 1979; Halevi, 1983) are an important example of this type of deformable mirror and have the unique feature that they solve the Poisson equation (Roddier, 1988a; Ribak, 1994; Schwartz *et al.*, 1994).

Continuous deformable mirrors provide the advantage of avoiding the diffraction effects associated with segmented deformable mirrors. A disadvantage is the complexity of the algorithm required to control them. The face-sheet deformation associated with a particular actuator is not generally independent of the other actuator's responses. Even if the actuator responses are independent, the face-sheet deformation associated with a particular actuator generally overlaps the response of neighboring actuators. Another disadvantage of the continuous deformable mirror is the practical problem of repairing bad actuators (Ribak, 1994). Examples of continuous deformable-mirror designs are discussed by Hardy (1978), Ealey and Washeba (1990), Hulburd and Sandler (1990), Ealey and Wellman (1991), Ribak (1994), and Schwartz *et al.* (1994).

b. Influence functions and modeling

In order to model the deformable mirror in performance analyses it is necessary to quantify how the signal applied to a particular actuator changes the surface of the mirror. The change in the surface shape due to the application of a signal to an actuator is called the influence function. The influence function for a segmented mirror is localized to the region of the surface defined by a particular mirror segment. The influence function for a continuous deformable mirror is not restricted to a region around the actuator location as in the segmented mirror. In the continuous-mirror case, influence functions have been modeled with polynomials, trigonometric functions, and Gaussian functions (Hudgin, 1977a; Hardy, 1978; Wallner, 1983; Welsh and Gardner, 1989; Moore and Lawrence, 1990). Let the i th influence function be designated $r_i(\vec{x})$, where \vec{x} is a position on the deformable-mirror surface. By assuming linearity of the responses of all the actuators, we can model the surface of the mirror $\tilde{\phi}(\vec{x})$ with the following relationship:

$$\tilde{\phi}(\vec{x}, t) = \sum_i c_i(t) r_i(\vec{x}), \quad (72)$$

where $c_i(t)$ is the control signal applied to the i th actuator at time t . The key assumption affecting the validity of the model presented by Eq. (72) is the linearity of the actuator influence functions.

c. Tilt-compensation mirrors

Before moving on to discuss wave-front sensors, we should note that the first types of deformable mirrors used to compensate for the effects of atmospheric turbulence were tilt mirrors. These mirrors are sometimes called tip-tilt mirrors and represent the simplest type of wave-front control. For tilt compensation the surface is simply a flat mirror that can be adjusted to tilt in two orthogonal directions. Modern adaptive optical imaging systems typically have a tilt-correction mirror as the first stage of wave-front compensation. Performing tilt correction separately from the higher-order corrections lowers the dynamic-range requirements of the deformable mirror.

2. Wave-front sensors

The wave-front sensor provides the means of measuring the perturbed wave-front phase. Wave-front sensors used in adaptive optical imaging systems do not directly measure the wave-front phase $\phi(\vec{x}, t)$, but rather the spatial gradient or Laplacian of $\phi(\vec{x}, t)$. The spatial gradient is commonly referred to as the wave-front slope, while the Laplacian is referred to as the wave-front curvature. An estimate of $\phi(\vec{x}, t)$ is computed from the wave-front derivative, using a phase reconstruction algorithm.

One of the fundamental performance issues associated with the fidelity of phase reconstruction is the accuracy of the measured derivatives, given finite light levels in the wave-front sensor and detector noise. The other fundamental issue affecting phase reconstruction is the wave-front sample spacing. We introduce the basic types of wave-front sensors used in adaptive optical imaging systems.

The first two types of wave-front sensors used in adaptive optical imaging systems are derived from wave-front sensors used in optical testing (Rousset, 1994). Both of these wave-front sensors are sensitive to the slope of the wave-front phase. They both have the advantage of being broadband, or white-light sensors, which is an important consideration for astronomical imaging.

a. The Hartmann wave-front sensor

The Hartmann wave-front sensor (H-WFS) is based on the Hartmann test. A diagram of this sensor is depicted in the left side of Fig. 14. The Hartmann wave-front sensor spatially segments the incident wave front with a lenslet array. Each array element is referred to as a subaperture, and it focuses a spot onto an array of detectors in the lenslet focal plane. The right portion of Fig. 14 shows the centroid location of the spot focused on the detector, \vec{x}_s , is related to the wave-front slope \vec{s} over the subaperture by

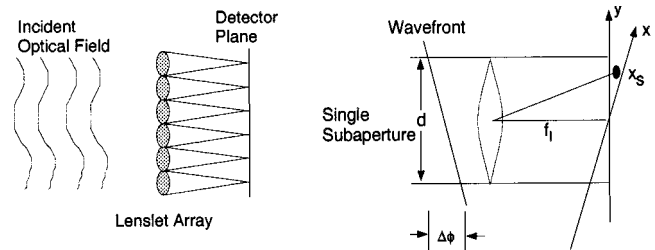


FIG. 14. Diagram of the Hartmann wave-front sensor (H-WFS).

$$\vec{s} = k \frac{|\vec{x}_s|}{f_l}, \quad (73)$$

where $k = 2\pi/\lambda$ and f_l is the focal length of the subaperture lens. One of the most common detector-array configurations is four detectors forming the quadrants of a square detector area, often referred to as a quad cell. A number of authors have investigated the performance of different detector-array configurations and have computed optimal detector-element sizes (Tyler and Fried, 1982; Winnick, 1986; Kane *et al.*, 1989; Witthoft, 1990; Cao and Yu, 1994).

The spot centroid computation associated with the Hartmann wave-front sensor and its relationship to the wave-front slope can be shown to be equivalent to computing the average wave-front phase gradient over the subaperture of the wave-front sensor (Yura and Tavis, 1985). Thus the mathematical model for the Hartmann wave-front measurement is

$$\vec{s}(j) = \int d\vec{x} W_j(\vec{x}) \nabla \phi(\vec{x}, t) + \vec{s}_n(j), \quad (74)$$

where $\vec{s}(j)$ is the vector wave-front slope associated with the j th subaperture, $\nabla \phi(\vec{x}, t)$ is the spatial gradient of $\phi(\vec{x}, t)$, $\vec{s}_n(j)$ is a random vector that accounts for measurement-noise effects, and $W_j(\vec{x})$ is the j th subaperture weighting function. The subaperture function $W_j(\vec{x})$ is normalized to have unit area.

The root-mean-square value of the slope-measurement noise, σ_n , is related to the standard deviation of the spot-location measurement, σ_c . Both shot noise and read noise contribute to the spot-measurement error. In the case of a Hartmann wave-front sensor using a quad cell, the contribution to σ_n due to photon noise has been found to be (Tyler and Fried, 1982; Welsh *et al.*, 1995)

$$\sigma_{ns} = \frac{\sqrt{2} \pi}{d(\bar{K})^{1/2} \int_{-1}^1 df_x I_b(f_x, 0) \mathcal{H}_{tr}(f_x, 0)} \quad (\text{rad/m}), \quad (75)$$

where d is the subaperture dimension and \bar{K} is the total average detected-photon count per subaperture measurement. The subscript ns designates the noise contribution due to shot noise. The function $I_b(f_x, f_y)$ is the Fourier transform of the beacon-intensity distribution projected into the subaperture lens focal plane, and $\mathcal{H}_{tr}(f_x, f_y)$ is the tilt-removed optical transfer function

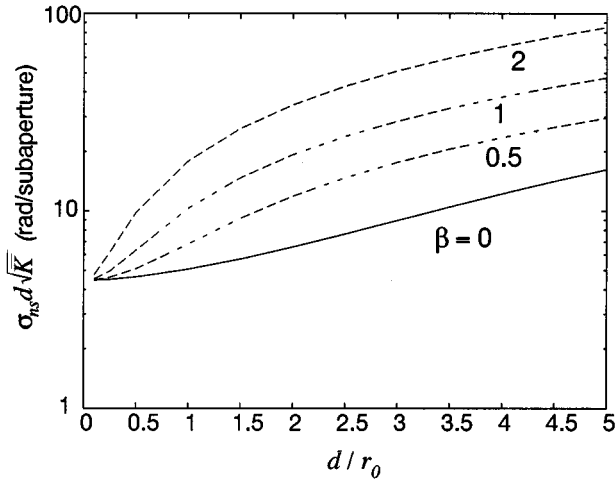


FIG. 15. Plot of σ_{ns} versus d/r_0 for the Hartmann wave-front sensor for β ranging from 0 to 2. The parameter d is the subaperture dimension, \bar{K} is the average detected photon count per measurement, and β is the ratio of the angular beacon size to the angular seeing limit, $\beta = (\sigma_b/z_b)/(\lambda/r_0)$.

(OTF) of the subaperture. The spectrum $I_b(f_x, f_y)$ is normalized such that $I_b(0,0) = 1$. In Eq. (75) the spatial frequency variables f_x and f_y are normalized to the diffraction limit of the subaperture, $d/\lambda f_l$.

The dependency of Eq. (75) on a number of key factors is evident. The finite light level is characterized by the average photon count per measurement \bar{K} . The effect of the beacon size on the accuracy of the measurement is characterized by the beacon spatial spectrum I_b . Finally, the broadening of the beacon spot in the lenslet focal plane due to atmospheric turbulence is characterized by the tilt-removed optical transfer function \mathcal{H}_{tr} . Using a Gaussian beacon-intensity profile and the short-exposure optical transfer function given in Eq. (46), we can numerically evaluate Eq. (75). Figure 15 is a plot of the σ_{ns} versus d/r_0 . The parameter β is the ratio of the rms angular beacon size to the angular seeing limit [i.e., $\beta = (\sigma_b/z_b)/(\lambda/r_0)$, where σ_b is the rms width of the beacon and z_b is the height of the beacon]. It is apparent from Fig. 15 that increasing the beacon size causes a significant worsening of the shot-noise error. A decreasing value of r_0 (or equivalently an increasing value of the ratio d/r_0) is also seen to increase the measurement error.

The other main source of error is the noise added in the process of reading the detector. This noise is referred to as sensor noise or, in the special case of a charge-coupled-device (CCD) detector, as read noise. In the case that $r_0 \geq d$ and $\beta \leq 1$, Parenti and Sasiela (1994) have shown that the contribution to σ_n due to read noise for a quad cell is

$$\sigma_{nr} = \frac{\sqrt{2} \pi}{d \sqrt{\bar{K}^2 / 4 \sigma_e^2}}, \quad (76)$$

where σ_e^2 is the variance of the read or electronic noise

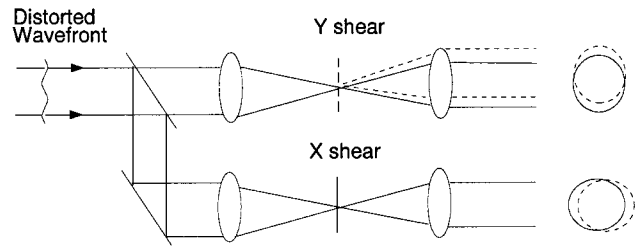


FIG. 16. Simple optical diagram of the shearing-interferometer wave-front sensor (Hardy, 1978).

for each pixel in the detector array, expressed in units of photoelectrons squared. More general expressions for the read-noise contribution to σ_n have been developed by Parenti and Sasiela (1994) for larger detector arrays and for spot broadening due to atmospheric turbulence.

To obtain the total slope-measurement error, the shot-noise and read-noise errors must be combined to give the total measurement error σ_n^2 :

$$\sigma_n^2 = \sigma_{ns}^2 + \sigma_{nr}^2. \quad (77)$$

b. The shearing interferometer

The other common wave-front sensor used in adaptive optical imaging is the lateral shearing interferometer (SI-WFS) (Wyant, 1975), shown in Fig. 16. The shearing interferometer splits the incident field into two optical beams: an x -leg and y -leg beam. Before optical detection the beams are split again and laterally shifted (sheared) with respect to each other. The most common approach used to achieve the shear involves the use of gratings (Wyant, 1974; Horwitz, 1990). Another approach makes use of beam separation by polarization (Hardy and MacGovern, 1987). Regardless of the beam-separation approach, the x - and y -directed wave-front slopes are sensed separately in each leg. Depending on the specific type of shearing interferometer, the optical field in each leg is split a number of times (Sandler *et al.*, 1994). The amount of shear is an adjustable parameter. The sheared beams are superimposed on an optical detector to form an interference pattern. The subapertures are established by the pixels on the detector. The detector plane is conjugated to the pupil plane of the optical system, and each detector element defines a single subaperture.

The particular algorithm used to transform the pixel-irradiance measurements into wave-front slope estimates depends on the type of shearing interferometer. For the ac type, a time-varying phase modulation is applied to one of the sheared beams (Wyant, 1975; Horwitz, 1990). The detected signal in this case is a sinusoidal time-varying signal, whose phase is related to the slope of the incident wave front. In the case of the static three- and four-bin (sometimes referred to as the three- and four-point) shearing-interferometer wave-front sensors, the detected irradiances are constant signals that can be combined together to estimate the phase slope (Sandler *et al.*, 1994).

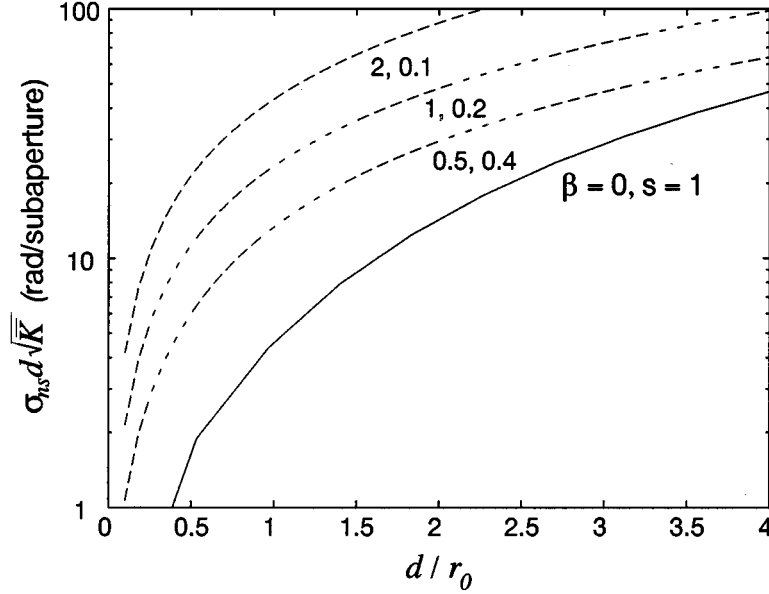


FIG. 17. Plot of σ_{ns} vs d/r_0 for the shearing-interferometer wave-front sensor for β ranging from 0 to 2. The parameter d is the subaperture dimension, \bar{K} is the average detected photon count per measurement, and β is the ratio of the angular beacon size to the angular seeing limit, $\beta = (\sigma_b/z_b)/(\lambda/r_0)$. For each value of β the optimum value of shear was found, and it is this optimum value that is used to compute the shot-noise error presented in the graph.

Regardless of the specific type of shearing interferometer discussed above, for modeling purposes the measured slope signal for the j th subaperture is mathematically modeled by

$$\begin{aligned} \vec{s}_m(j) = \int d\vec{x} W_j(\vec{x}) \left[\frac{\Delta\phi(\vec{x}, \Delta\vec{x}_x)}{|\Delta\vec{x}_x|} \hat{x} + \frac{\Delta\phi(\vec{x}, \Delta\vec{x}_y)}{|\Delta\vec{x}_y|} \hat{y} \right] \\ + \vec{s}_n(j) \quad (\text{shearing interferometer model}), \end{aligned} \quad (78)$$

where $\Delta\phi(\vec{x}, \Delta\vec{x}) = \phi(\vec{x}) - \phi(\vec{x} + \Delta\vec{x})$, \hat{x} and \hat{y} are unit vectors in orthogonal directions in the sensing plane, $\Delta\vec{x}_x$ and $\Delta\vec{x}_y$ are shears in the \hat{x} and \hat{y} directions, and $\vec{s}_n(j)$ again represents the measurement noise. The variance of the measurement-error term \vec{s}_n depends on light level, beacon size, atmospheric effects, and shear distances $\Delta\vec{x}_x$ and $\Delta\vec{x}_y$.

The measurement error due to shot noise for the shearing interferometer has been found to be (Welsh *et al.*, 1995)

$$\sigma_{ns} = \frac{2\sqrt{2}}{r_0(\bar{K})^{1/2} s \mu_a(s) \mu_b(s)} \quad (\text{rad/m}), \quad (79)$$

where \bar{K} is the total average photon count detected per subaperture measurement, $\mu_a(s)$ is the visibility reduction due to atmospheric seeing effects, $\mu_b(s)$ is the visibility reduction due to the size of the beacon, and s is the normalized shear, $s = |\Delta\vec{x}_x|/r_0$ or $|\Delta\vec{x}_y|/r_0$. For the specific case in which the beacon is modeled by a Gaussian irradiance distribution having an rms width of σ_b and an altitude of z_b , we find, through application of the Van Cittert-Zernike theorem (Born and Wolf, 1964), that

$$\mu_b(s) = \exp[-\pi^2 \beta^2 s^2], \quad (80)$$

where β is the angular size of the beacon relative to the seeing-limited angle [$\beta = (\sigma_b/z_b)/(\lambda/r_0)$]. Substituting Eq. (80) into Eq. (79) gives

$$\sigma_{ns} = \frac{2\sqrt{2}}{r_0(\bar{K})^{1/2} s \mu_a(s)} \exp[\pi^2 \beta^2 s^2] \quad (\text{rad/m}). \quad (81)$$

The atmospheric-visibility term $\mu_a(s)$ has been investigated for the case of atmospheric turbulence having the Kolmogorov index-of-refraction power spectral density given in Eq. (5) (Welsh *et al.*, 1995). The error given in Eq. (81) has been evaluated and presented in the graph shown in Fig. 17. Figure 17 is a plot of σ_{ns} versus d/r_0 for β ranging from 0 to 2.

Read noise also contributes to the slope error for the shearing-interferometer wave-front sensor. Sandler *et al.* (1994) have investigated the read-noise contribution to the slope error and found that

$$\sigma_{nr} = \frac{\sqrt{8}\sigma_e}{r_0 \bar{K} s \mu_a(s) \mu_b(s)} \quad (\text{rad/m}) \quad (82)$$

for a four-bin interferometer and

$$\sigma_{nr} = \frac{\sqrt{6}\sigma_e}{r_0 \bar{K} s \mu_a(s) \mu_b(s)} \quad (\text{rad/m}) \quad (83)$$

for a three-bin interferometer. To obtain the total slope-measurement error σ_n , the shot-noise and read-noise errors are combined as in Eq. (77).

c. Curvature sensing

The other type of wave-front sensor that has found use in adaptive optical imaging systems is the curvature sensor (Roddiier, 1988a; Rousset, 1994). The curvature sensor measures a signal proportional to the Laplacian or second derivative of the wave-front phase. The La-

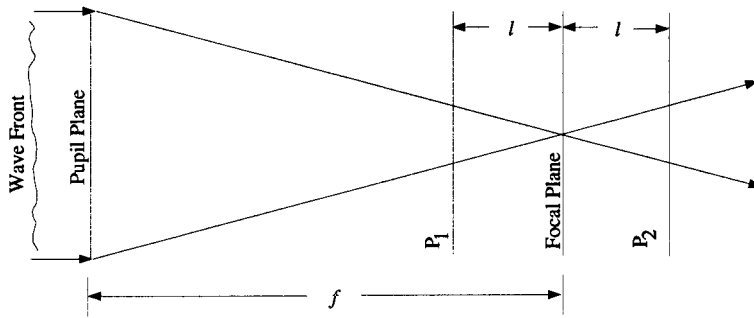


FIG. 18. Schematic of a curvature wave-front sensor. The difference in the irradiance between the planes P_1 and P_2 is proportional to the local wave-front curvature in the pupil. The irradiance difference is also proportional to the radial tilt of the wave front at the edge of the pupil.

placian measurements are combined with wave-front tilt measurements around the edge of the system pupil to reconstruct the wave front by solving the Poisson equation. One of the advantages of using a curvature sensor is that solving the Poisson equation can be accomplished directly by applying the Laplacian measurements to a membrane or bimorph mirror (Roddier, 1988a; Rousset, 1994; Schwartz *et al.*, 1994). Another advantage is that the wave-front curvature is a scalar-field quantity and, as a result, requires only one measurement per pupil sample point. Additionally, if the power spectrum of the wave front follows a $f^{-11/3}$ power law, the power spectrum of the wave-front curvature will follow a $f^{1/3}$ power law (Roddier, 1988a). The $f^{1/3}$ power law is nearly flat and will result in curvature measurements that are nearly uncorrelated, implying that the curvature sensor requires fewer measurements than a gradient wave-front sensor to characterize the wave front.

The curvature-sensing method as first presented by Roddier (1988a) is shown with the conceptual drawing in Fig. 18. The pupil field is incident from the left, and the irradiance of the field is measured in the two planes P_1 and P_2 . These two planes are placed a distance l in front and in back of the telescope focal plane. Note that in practice a beam splitter would be used to divide the light and form two images. A geometrical-optics analysis shows that the irradiance difference is related to the wave-front curvature and the radial tilt of the wave front at the edge of the pupil as follows:

$$\frac{i_1(\vec{x}) - i_2(-\vec{x})}{i_1(\vec{x}) + i_2(-\vec{x})} = \frac{f(f-l)}{l} \left[\nabla^2 \phi \left(\frac{f\vec{x}}{l} \right) - \frac{\partial}{\partial n} \phi \left(\frac{f\vec{x}}{l} \right) \delta_c \right], \quad (84)$$

where $i_1(\vec{x})$ and $i_2(\vec{x})$ are the irradiances measured in the planes P_1 and P_2 as a function of transverse-vector location \vec{x} , $\phi(\vec{x})$ is the pupil wave-front phase, and δ_c is an impulse distribution around the pupil edge, weighted by the derivative of the wave-front phase in the direction normal to the pupil edge, $\partial\phi(\vec{x})/\partial n$.

Roddier *et al.* (1988), Roddier (1991), and Roddier *et al.* (1991) have argued convincingly that curvature sensing has a performance advantage over gradient wave-front sensors when low-order or partial wave-front correction is the goal. This advantage is particularly evident when the deformable mirror inherently corrects the wave-front Laplacian as membrane and bimorph mirrors do. Recently, Roddier (1994) presented the first as-

tronomical images obtained from a low-order adaptive optical imaging system using a curvature sensor.

3. Controllers

In Eq. (72) we introduced a model to characterize how the control signals $c_i(t)$ are mapped into the mirror surface $\hat{\phi}(\vec{x}, t)$. It is intuitively appealing to think of the i th influence function as representing the actual shape of the mirror that results for a unit signal applied to the i th actuator. In this case $c_i(t)$ is associated with the actual control signal sent to the i th actuator as a function of time. The control algorithm derived using this interpretation of $r_i(\vec{x})$ is commonly referred to as zonal controller. This physically motivated interpretation of $r_i(\vec{x})$ is not the only interpretation possible. The function $r_i(\vec{x})$ can also be associated with a member of any set of basis functions or modes. When this modal association is used the resulting wave-front control algorithm is called a modal controller. Normally the modes are chosen to be an orthogonal basis set such as Zernike polynomials (Noll, 1976) or Karhunen-Loève modes (Roddier, 1990; Dai, 1995; Roggemann and Welsh, 1996). In this case $c_i(t)$ is associated with the weighting coefficient of the i th mode as a function of time. To use modal control the individual modes must be related to the physical influence functions of the mirror. This relationship will be an approximation of a particular mode with a linear combination of the deformable-mirror influence functions. The key point to remember is that the functions $r_i(\vec{x})$ can be associated with any set of functions, whether they are deformable-mirror influence functions or wave-front modes.

The problem at hand is finding a mapping from wave-front sensor measurements to control signals that results in the desired system performance. The phrase “desired performance” has different meanings depending on the performance metric being minimized or maximized. Qualitatively the goal is to achieve a mapping that results in $\phi(\vec{x}, t) \approx \hat{\phi}(\vec{x}, t)$. We present two basic results that achieve the mapping of the wave-front sensor measurement to deformable-mirror control signals. In both cases the transformation is a linear mapping. In other words the control matrix M has the following form:

$$c = Ms_m, \quad (85)$$

where c is a column vector of the control signals and s_m is a column vector of the measured subaperture slopes.

The two basic approaches for deriving the control matrix M are distinguished from each other by the quantity that is minimized in the solution process. In the first approach M is derived by minimizing the difference between the measured wave-front slopes and the slopes associated with the the surface of the deformable mirror. This minimization falls within the formalism of “maximum *a posteriori* estimation” and “least-squares” estimation (Melsa and Cohn, 1978). In the second approach, knowledge of both the wave-front statistics and the noise characteristics of the wave-front sensor are used to derive a control matrix that minimizes the aperture average mean-square residual phase error.

a. Maximum *a posteriori* controller

For the maximum *a posteriori* (MAP) estimation development to follow, the slope-measurement model is assumed to take the following form:

$$s_m = s_{dm} + s_n, \quad (86)$$

where s_{dm} is a column vector of the slopes associated with the surface of the deformable mirror and s_n is the column vector of associated noise realizations due to shot and read noise. In the MAP-estimation approach we attempt to minimize $|s_m - s_{dm}|^2$, where the notation $|a|^2 = a^T a$. This approach is well suited for closed-loop adaptive optical systems in which the difference, $s_m - s_{dm}$, is the closed-loop measurement used to update the mirror-control signals. The result of the minimization is found in the work of Melsa and Cohn (1978), who give the optimum control vector as

$$c = (H^T C_n^{-1} H + C_c^{-1})^{-1} H^T C_n^{-1} s, \quad (87)$$

where the matrix H is called the Jacobian matrix, with the j th vector element defined as

$$H_{ji} = \int d\vec{x} W_j(\vec{x}) (\nabla r_i(\vec{x}) \cdot \vec{d}_j), \quad (88)$$

and the matrices C_c and C_n are the covariance matrices for c and s_n :

$$\begin{aligned} C_c &= \langle c c^T \rangle, \\ C_n &= \langle s_n s_n^T \rangle. \end{aligned} \quad (89)$$

The function $W_j(\vec{x})$ is the j th subaperture weighting function, and \vec{d}_j is a unit vector pointing in the direction of the sensitivity of the j slope measurement. The superscript T designates vector transpose.

Matching the terms in Eqs. (85) and (87), we see that the maximum *a posteriori* control matrix is given by

$$M_{\text{MAP}} = (H^T C_n^{-1} H + C_c^{-1})^{-1} H^T C_n^{-1}. \quad (90)$$

The slope-measurement-noise covariance matrix C_n will in many cases be diagonal, since the photon noise and the read noise are independent for each subaperture measurement. In the case that the noise variance of each subaperture measurement is the same and equal to σ_n^2 , Eq. (90) reduces to

$$M_{\text{MAP}} = (H^T H + \sigma_n^2 C_c^{-1})^{-1} H^T. \quad (91)$$

This control matrix has also been derived by others (Sasiela and Mooney, 1985; Fried, 1994b).

b. Least-squares controller

The maximum *a posteriori* reconstructor given above in Eq. (91) reduces to the well-known least-squares solution as the measurement-noise variance decreases to zero. The least-squares control matrix is the simplest controller to compute because neither the noise nor atmospheric statistics are required. Only the Jacobian matrix H is required, and the elements of this matrix can be obtained by measuring the response of the wave-front sensor to changes of individual actuator control signals. Letting the noise variance go to zero in Eq. (91) gives the least-squares control matrix M_{LS} . We note that M_{LS} corresponds to the Moore-Penrose generalized inverse or pseudo-inverse of H . A great many authors have presented the least-squares development for the control of the deformable mirror in an adaptive optical imaging system (Wallner, 1983; Tyson, 1991; Roggemann, 1992; Fried, 1994b; Rousset, 1994).

c. Minimum-variance controller

An alternative controller is the minimum-variance controller, for which the aperture-averaged residual mean-square phase is minimized. To define the aperture-averaged mean-square residual phase, note that the residual phase is designated $\epsilon(\vec{x})$ and is defined as

$$\epsilon(\vec{x}) = \phi(\vec{x}) - \hat{\phi}(\vec{x}), \quad (92)$$

where $\phi(\vec{x})$ is the piston-removed wave-front phase perturbation and $\hat{\phi}(\vec{x})$ is the piston-removed wave-front phase correction applied by the deformable mirror. The aperture-averaged mean-square residual phase is defined by

$$\langle \epsilon^2 \rangle = \int d\vec{x} W(\vec{x}) \langle \epsilon^2(\vec{x}) \rangle, \quad (93)$$

where $W(\vec{x})$ is the pupil weighting function of the adaptive optical imaging (AOI) system. The minimum-variance controller will result in optimal performance, since its derivation incorporates statistical information concerning the incident wave-front phase $\phi(\vec{x})$ and the noise on the wave-front sensor measurements. Additionally, it has been shown that minimizing $\langle \epsilon^2 \rangle$ is equivalent to maximizing the adaptive optical imaging system's Strehl ratio (Herrmann, 1992). The Strehl ratio is defined as the ratio of the peak of the system's point-spread function to the peak of the point-spread function of an unaberrated system.

Minimizing $\langle \epsilon^2 \rangle$ results in the following minimum-variance control matrix (Roggemann and Welsh, 1996):

$$M_{MV} = R^{-1} A S^{-1}, \quad (94)$$

where the matrices S , R , and A are defined as

$$S = \langle s_m s_m^T \rangle, \quad (95)$$

$$R = [r(\vec{x}), r^T(\vec{x})], \quad (96)$$

$$A = [r(\vec{x}), \langle \phi(\vec{x}) s_m^T \rangle]. \quad (97)$$

The quantity s_m is a column vector composed of the wave-front sensor's subaperture slope measurements, $r(\vec{x})$ is a column vector composed of the influence functions of the deformable-mirror actuator, and the notation $[f(\vec{x}), g(\vec{x})]$ is an inner product defined as

$$[f(\vec{x}), g(\vec{x})] = \int d\vec{x} W(\vec{x}) f(\vec{x}) g(\vec{x}). \quad (98)$$

The minimum-variance control matrix results in a minimum residual mean-square phase error $\langle \epsilon^2 \rangle$ of

$$\langle \epsilon^2 \rangle = [\phi(\vec{x}), \phi(\vec{x})] - \text{tr}(R^{-1} A S^{-1} A^T), \quad (99)$$

where $\text{tr}(C)$ is the trace of the square matrix C .

The practical drawback associated with implementing the minimum-variance controller is accurately characterizing the wave-front phase and sensor noise statistics so that S and A can be computed. In most situations this prior knowledge is not available. If accurate prior knowledge of the required statistics is available, it has been shown that the minimum-variance controller outperforms the least-squares solution (Wallner, 1983; Roggemann, 1992).

4. Bandwidth requirements

a. Tilt compensation

The bandwidth requirement for tilt correction for a circular aperture has been derived by Tyler (1994a). Assuming a first-order controller for tilt compensation, Tyler finds that the residual angular tilt variance after tilt compensation can be expressed as

$$\sigma_{\theta}^2 = \left(\frac{f_T}{f_{3 \text{ dB}}} \right)^2 \left(\frac{\lambda}{D} \right)^2, \quad (100)$$

where $f_{3 \text{ dB}}$ is the temporal frequency at which the tilt-compensator response is down 3 dB from the maximum value, λ is the optical wavelength, D is the diameter of the system pupil, and

$$f_T = 0.368 D^{-1/6} \lambda^{-1} \left[\int dz C_n^2(z) v^2(z) \right]^{1/2}. \quad (101)$$

The parameter $f_{3 \text{ dB}}$ is also referred to as the bandwidth of the tilt compensator. In Eq. (101) $v(z)$ is the path-dependent turbulence velocity profile. In the special case that the velocity profile is constant with respect to z , Eq. (101) can be written in terms of the Fried parameter given in Eq. (25):

$$f_T = 0.0902 \left(\frac{r_0}{D} \right)^{1/6} \left(\frac{v}{r_0} \right). \quad (102)$$

Good tilt correction should result in an angular rms tilt variation that is one-fourth the angular resolution of the diffraction-limited pupil, λ/D (Tyler, 1994a). To obtain this level of tilt correction, the bandwidth of the controller $f_{3 \text{ dB}}$ must be greater than $4f_T$. An aperture diameter of $D = 20r_0$ and a wind velocity of $v = 100r_0/s$ implies that the controller bandwidth must be 22 Hz.

We finally note that a more recent study (Conan *et al.*, 1995) of the bandwidth requirements for wave-front correction has indicated that the tilt-correction portion of an adaptive optical imaging system must have a bandwidth higher than that given above. This conclusion is based on an investigation of bandwidth requirements for tilt and higher-order modal correction. Conan *et al.* (1995) show that, to achieve the same residual wave-front errors as achieved by the higher-order modal correction, the tilt-compensation bandwidth must be higher than the bandwidths for the higher-order modes.

b. Higher-order compensation

The bandwidth requirements for full wave-front compensation have been studied by a number of researchers (Greenwood and Fried, 1976; Greenwood, 1977; Tyler, 1984; Fried, 1990b; Karr, 1991; Welsh, 1992; Harrington and Welsh, 1994). Greenwood (1977) derives the mean-square residual wave-front error (including the tilt-error contribution) as a function of servoloop bandwidth for a first-order controller. This error is given by

$$\sigma_{\epsilon}^2 = \left(\frac{f_G}{f_{3 \text{ dB}}} \right)^{5/3}, \quad (103)$$

where $f_{3 \text{ dB}}$ is the 3-dB bandwidth of the wave-front compensator and f_G is the Greenwood frequency:

$$f_G = \left[0.102 k^2 \int_0^{\infty} dz C_n^2(z) v^{5/3}(z) \right]^{3/5}. \quad (104)$$

In the special case that the velocity profile is constant with respect to z , Eq. (104) can be written in terms of the Fried parameter given in Eq. (25)

$$f_G = \frac{0.426v}{r_0}, \quad (105)$$

where v is the transverse velocity of the turbulence.

C. Adaptive optical imaging system performance

In the following subsection we present a series of representative performance calculations for adaptive optical imaging systems. The analytical results are largely drawn from Welsh (1991). The adaptive optical imaging system considered in the following subsections has the following general characteristics.

Telescope Pupil. The pupil, shown in Fig. 19, is annular with an obscuration ratio of $D_o/D = 0.4$, where D is the pupil diameter and D_o is the diameter of the obscuration. The pupil diameter is assumed to be 3 m.

Wave-Front Sensor. The wave-front sensor is a Hartmann sensor with square subapertures of side length d . The number of subapertures spanning the pupil diameter ranges from 15 to 16. Figure 19 shows the subaperture geometry for the case in which 15 subapertures span the diameter.

Deformable Mirror. The mirror is assumed to be of monolithic design with an actuator spacing equal to the

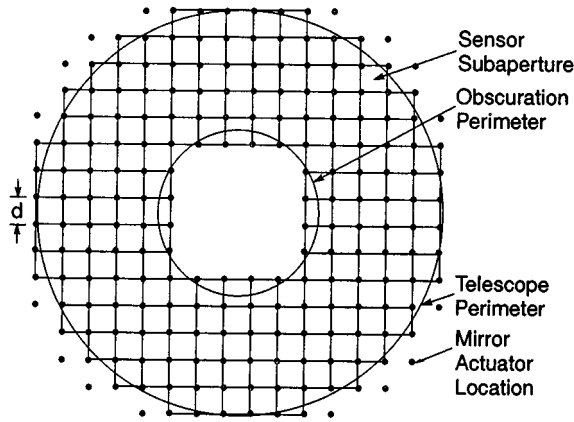


FIG. 19. Telescope pupil, deformable mirror, and wave-front sensor geometry.

subaperture dimensions d . The influence function for the i th actuator, $r_i(\vec{x})$, is modeled by a Gaussian function:

$$r_i(\vec{x}) = \exp\left(\frac{-(\vec{x} - \vec{x}_i)^2}{d_a^2}\right), \quad (106)$$

where \vec{x}_i specifies the location of the i th actuator and d_a is the influence radius. The Gaussian response is often used to model piezoelectric or membrane-deformable mirrors (Welsh and Gardner, 1989). For the results presented here we assume $d_a = d$. Actuator locations are indicated by the large dots in Fig. 19.

Beacon. We consider cases in which the adaptive optical imaging system uses both a finite-altitude laser beacon and a natural guide star. In order to incorporate the effects of anisoplanatism we account for the altitude of the guide star as well as the altitude distribution of the turbulence. When we refer to the effects of anisoplanatism we restrict our attention to the degradation of the on-axis wave-front compensation caused by the difference between the path of the optical ray from

the guide star and that from the celestial object of interest. We also assume that a sufficiently bright, on-axis, natural guide star is used for overall tilt control (i.e., perfect overall tilt compensation is assumed).

C_n^2 Altitude Profile. The turbulence-altitude profile is characterized by the structure constant of the refractive-index fluctuations, C_n^2 . Welsh and Gardner (1991) have presented an analysis of the effects of anisoplanatism on laser-guided telescopes. In this earlier analysis, the authors consider a single-layer model of the turbulence-altitude profile, as well as the more realistic Hufnagel-Valley continuous C_n^2 model (Hufnagel, 1974). For the results presented here we use the simpler, single-layer model. The single layer is assumed to be located at the altitude $z_t \approx 10$ km.

1. Mean-square residual phase error $\langle \epsilon^2 \rangle$

We start by considering the simplest and easiest-to-compute performance metric: the aperture-averaged, residual wave-front phase error $\langle \epsilon^2 \rangle$. Figure 20 is a plot of $\langle \epsilon^2 \rangle^{1/2}$ versus photon flux incident on the wave-front sensor for the case of $z_t/z_b = 0.109$. This particular ratio approximately matches the geometry in which the guide star is located at an altitude of 92 km (nominal height of the mesospheric Na layer) and the turbulence is at a height of 10 km. As expected, $\langle \epsilon^2 \rangle^{1/2}$ decreases with increasing flux. This trend simply indicates that the slope measurements become less noisy as the brightness of the guide star is increased. The asymptotic behavior of each curve as the flux increases is indicative of the limitations imposed on performance by the wave-front sensor and mirror-actuator sampling intervals. Notice that at the higher flux levels $\langle \epsilon^2 \rangle^{1/2}$ decreases with decreasing subaperture and actuator spacing (i.e., decreasing d/r_0). This trend is expected, since decreasing d/r_0 results in smaller sampling intervals in both the wave-front sensor and the deformable mirror, which in turn results in improved sampling and reconstruction of the higher-spatial-frequency phase deformations. Recall that $d/r_0 \leq 1$ falls within the category of an adaptive optical

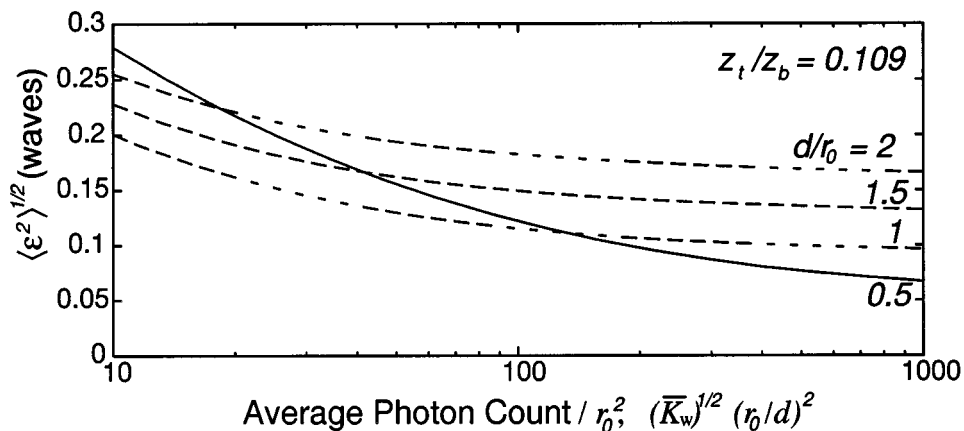


FIG. 20. rms wave-front error $\langle \epsilon^2 \rangle^{1/2}$ plotted vs photon flux for the adaptive optical imaging system described in this section. The ratio of the turbulence altitude to the guide-star altitude is $z_t/z_b = 0.109$. The family of curves are for d/r_0 ranging from 0.5 to 2.

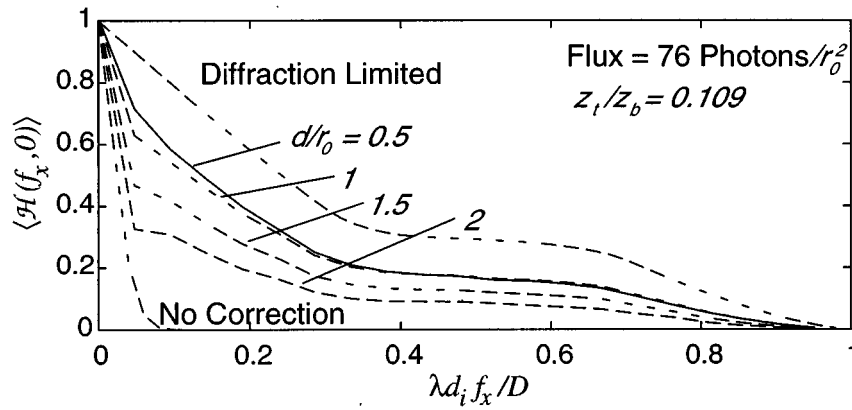


FIG. 21. Ensemble-average optical transfer function $\langle \mathcal{H}(f_x, 0) \rangle$ vs spatial frequency f_x for the adaptive optical imaging system described in this section. Also shown are optical transfer functions for the case of diffraction-limited performance and the case of no wave-front compensation. For each curve the flux is 76 photons/ r_0^2 , and the ratio $z_t/z_b=0.109$.

imaging system that we characterize as a fully compensated system. Figure 20 indicates that even systems labeled as being fully compensated are fundamentally limited by either the light level or the finite sampling of the incident wave-front phase.

In contrast to the trends observed for high light levels, at the lower flux levels we observe that performance can actually be better for larger values of d/r_0 . Systems with $d/r_0 > 1$ are characterized as partially compensated systems. This reversal in performance is explained by realizing that, at the low flux levels, noise is the predominant cause of wave-front error. For a given flux level the measurement-noise effects will increase for decreasing values of d/r_0 . The measurement noise increases because the light collected by each wave-front sensor subaperture is proportional to d^2 . At low flux levels, decreasing values of d/r_0 increase the effect of measurement noise at a faster rate than the beneficial effects expected from smaller subapertures. These two opposing trends indicate that for a given flux level there will exist an optimum value of d/r_0 that minimizes wave-front error.

2. Average optical transfer function and point-spread function

The graph in Fig. 21 shows the average optical transfer function $\langle \mathcal{H}(\vec{f}) \rangle$ plotted versus normalized spatial frequency. The OTF is plotted along the x -directed component of \vec{f} , and the frequency axis is normalized to the diffraction-limited cutoff of the pupil. The wave-front sensor flux is held constant at 76 photons/ r_0^2 . This is the level specified by Gardner *et al.* (1990) in their study of adaptive optical imaging systems employing laser beacons. The OTF curves for the case of no correction and for the case of diffraction-limited seeing are also shown. Between these two limiting cases are the OTF curves for d/r_0 ranging from 0.5 to 2. Notice the significant improvement in the response of the optical transfer function for decreasing values of d/r_0 . This improvement is most noticeable in going from the partially compensated system with $d/r_0=2$ to the fully compensated system with $d/r_0=1$. It is also interesting to notice that for each

of the values of d/r_0 shown, the adaptive optical imaging system preserves spatial frequencies out to the diffraction limit. This is in contrast to the case of no wave-front correction, where the spatial frequencies are cut off at $\sim 10\%$ of the maximum spatial frequency for diffraction-limited imaging.

The graph shown in Fig. 22 illustrates the average point-spread curves $\langle s(\vec{x}) \rangle$, which are derived from the OTF curves shown in Fig. 21. Recall that the point-spread function and the optical transfer function are related by a Fourier transform. The figure shows a cross section of the average point-spread function plotted versus an image-plane coordinate x that is normalized by $\lambda d_i/D$. Note how the peaks of the point-spread function decrease with decreasing levels of wave-front compensation (i.e., increasing d/r_0). We finally note that both the Strehl ratio and the angular resolution of the adaptive optical imaging system can be obtained from point-spread data. The Strehl ratio is the value of the point-spread function at the origin ($x D / \lambda d_i = 0$), normalized by the function's diffraction-limited value at the origin. For the normalization of Fig. 22 the Strehl ratio is obtained directly from the graph by identifying the intersection point of the point-spread function with the vertical axis. The angular resolution is derived from some

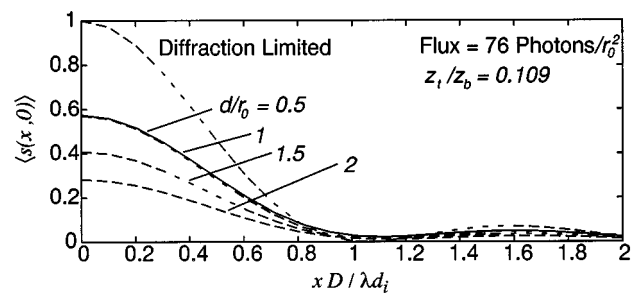


FIG. 22. Ensemble-average point-spread function (PSF), $\langle s(x, 0) \rangle$ vs image-plane coordinate x for the adaptive optical imaging system described in this section. Also shown is the ensemble point-spread function for the case of diffraction-limited performance. For each curve the flux is 76 photons/ r_0^2 , and the ratio $z_t/z_b=0.109$.

TABLE I. Key characteristics of the 1.5-m adaptive optical imaging system.

Parameter	Value
Telescope	1.5-m aperture, elevation over azimuth gimbals with coudé path
Adaptive optics	Configured off-gimbal in a coudé room optically coupled to the telescope by relay imaging optics
Wave-front sensing	Two Shack-Hartmann sensors, one for stars and one with range gating for a Rayleigh laser beacon
Wave-front sensor geometry	Square 9.2-cm subapertures, 16 across the diameter, 208 total inside the pupil
Wave-front sensor camera	Unintensified 64×64 pixel CCD focal-plane array, 4×4 pixels per subaperture
Laser wavelengths	0.5106 and 0.5782 μm , yellow power=twice green power
Pulse format	5000 pulses/sec, 50 ns pulse width
Backscatter range	10 km with 2.4 km range gate
Wave-front sensors	Unintensified CCD array in a Shack-Hartmann configuration
Transmit optical efficiency	0.40
Wave-front receive optical efficiency	0.25
Deformable mirror	Low-voltage lead-magnesium-niobate actuators, continuous facesheet of ULE glass
Number of actuators	241 independent; 201 with slaves
Closed-loop control bandwidth	Typically 100 Hz
Imaging wavelengths	0.7 to 2.2 μm
Camera resolution	Adjusted to $\lambda/2D$ for the wavelength of interest

predefined measure of the width of the point-spread function. The full width at half maximum (FWHM) is a common measure of angular resolution. The interesting point to note from the point-spread data shown in Fig. 22 is that angular resolution as determined by the FWHM metric does not significantly degrade as d/r_0 increases. This observation is typical for adaptive optical imaging systems. It is well known that the performance of adaptive optical imaging systems degrades in such a way that the width of the core remains constant as the point-spread peak decreases. The decrease of the peak (or equivalently the Strehl ratio) causes more light to be spread into a halo outside the central core.

D. Example of an adaptive optical imaging system

This section is a brief description of an operating adaptive-optics system. The system described is installed on a 1.5-m telescope at the U.S. Air Force Phillips Laboratory Starfire Optical Range (SOR) near Albuquerque, NM. It was developed and continues to evolve as a research tool to provide engineering data on the performance of adaptive optics under varying atmospheric conditions and hardware configurations. The 1.5-m telescope is dedicated full time to the development and use of this adaptive-optics system. Consequently, it probably has more operating hours than other systems being tested or developed for astronomy by groups who have limited observing time as visitors to astronomical observatories. For these reasons, the SOR system seems an appropriate example to highlight in this review.

The earliest versions of the Starfire 1.5-m adaptive-optics system have been described by Fugate *et al.* (1994). The current hardware configuration and recent experimental data are presented here. The major features of the system are presented in Table I, and the overall layout of the facility is shown in Fig. 23. This system is fairly complex, and its configuration is changed very frequently to support a variety of experiments. For these reasons, we decided to build up the system in a coudé room where large optics tables are available and where the controlled temperature facilitates the maintenance of optical registration and alignment. Locating the system on the telescope (which may not have been possible in this case due to the bulk of the system and the small size of the telescope) would improve the optical efficiency about one stellar magnitude (a factor of 2.5). Since we are mainly interested in engineering development and understanding factors that limit performance (and getting a complex system to work at all), we decided on the coudé-room approach. In the material that follows we describe the main subsystems and show engineering and scientific data obtained with the system.

1. Optics

The principal optical components are the telescope, relay optics, wave-front sensor optics, track sensor optics, and diagnostic and scientific camera optics. Figure 24 shows the telescope and relay optics located in the vertical support pedestal. The telescope is a classical Cassegrain design with a parabolic primary and hyperbolic secondary, which produces an $f/217$ output beam

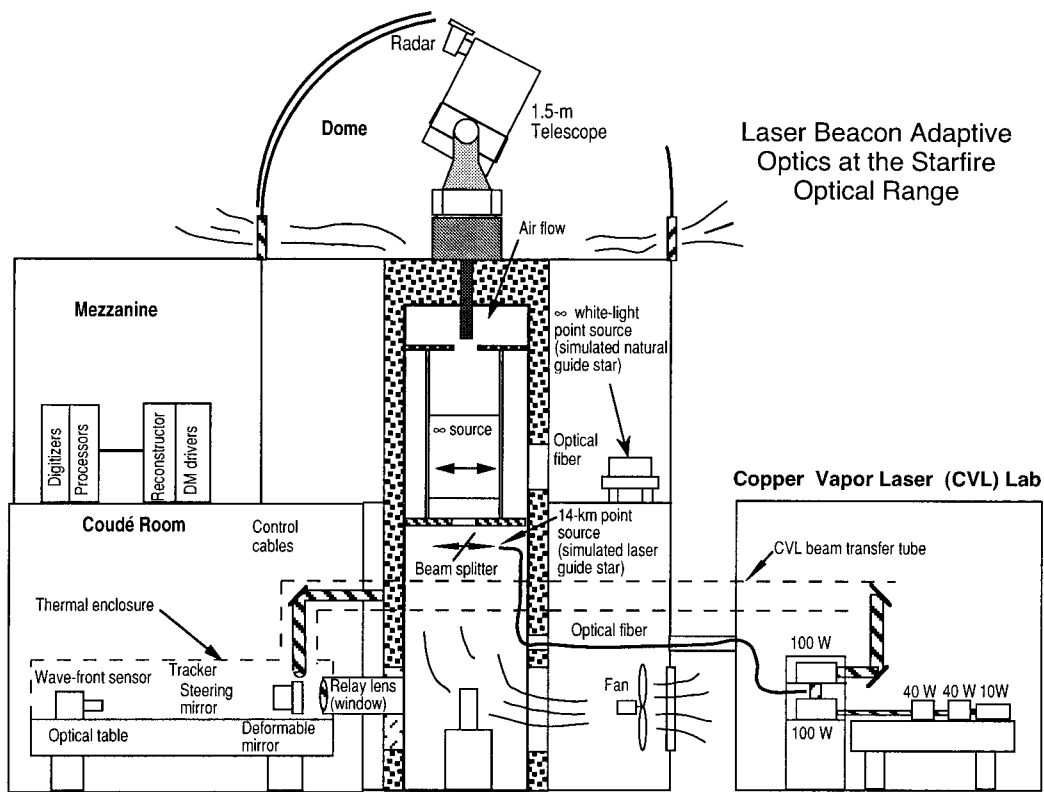


FIG. 23. Overview of the 1.5-m telescope and adaptive-optics facility. The laser and optics are on the ground floor, and the electronics and control center are located on the second floor of the observatory.

of 10 cm diameter. One feature of the relay optics is a spherical mirror that converts the $f/217$ beam to an $f/70$ beam and creates an intermediate focal plane half-way through the support pedestal. A simulated star in the form of a fiber optic on a precision translation stage can be positioned in this focal plane to provide a test source for alignment and adaptive-optics loop checkout prior to nighttime observing. The beam is directed into the coudé room through a fused-silica window by means of a turning flat at the base of the telescope pedestal. As shown in Fig. 23, nighttime air is constantly pulled through the dome, telescope, and pedestal by a large fan located on the ground floor. All large thermal masses are well insulated in this area to minimize convective and radiative heat transfer from the building structures and promote rapid and effective temperature equilibration of the air in the optical path.

Figure 25 shows schematically key features of the coudé-room optics. All of these components are mounted on a large optics table that sits on a foundation mechanically separated from the building's foundation.

2. Full-aperture tilt control

The coarse and fine steering mirrors control full-aperture tilt. The coarse mirror uses voice coil-actuator technology and can move over the full field of the telescope ($300 \mu\text{rad}$ full angle) but with limited speed (it can execute a $10 \mu\text{rad}$ sine wave at 30 Hz). The fine steering mirror uses piezoelectric actuators and has only a 30

μrad full-angle motion but can execute a $2 \mu\text{rad}$ peak-to-peak sine wave at 200 Hz. These mirrors are controlled by a type-I track processor, which computes the centroid of a star image on a fiber-optic-synthesized array of avalanche photodiodes (Fugate *et al.*, 1993). The sampling rate of the track sensor is 30–2000 measurements per second, depending on the signal provided by the object being tracked (Fugate, 1994). Furthermore, the coarse-mirror-control computer also communicates with the telescope-mount-control computer and can automatically update the open-loop mount pointing, if needed, so that the dynamic range of the steering mirrors is never exceeded. The open-loop mount pointing is outstanding for slow-moving objects like stars, and in normal operation the coarse mirror is caged and the fine steering is used for all full-aperture tilt corrections.

3. Deformable mirror

The off-axis parabola OAP1 is the second element in the relay optics, which, in conjunction with the 6.21-m-focal-length spherical mirror under the telescope (see Fig. 24), recollimates the beam and images from the primary mirror onto the plane of the deformable mirror. This means the primary mirror is optically located at the entrance pupil of the telescope, and light from objects in the entire $300\text{-}\mu\text{rad}$ full field of the telescope exactly overlap at the deformable mirror. This approach is not ideal in terms of increasing the effective size of the corrected field if the turbulence is predominantly in a layer

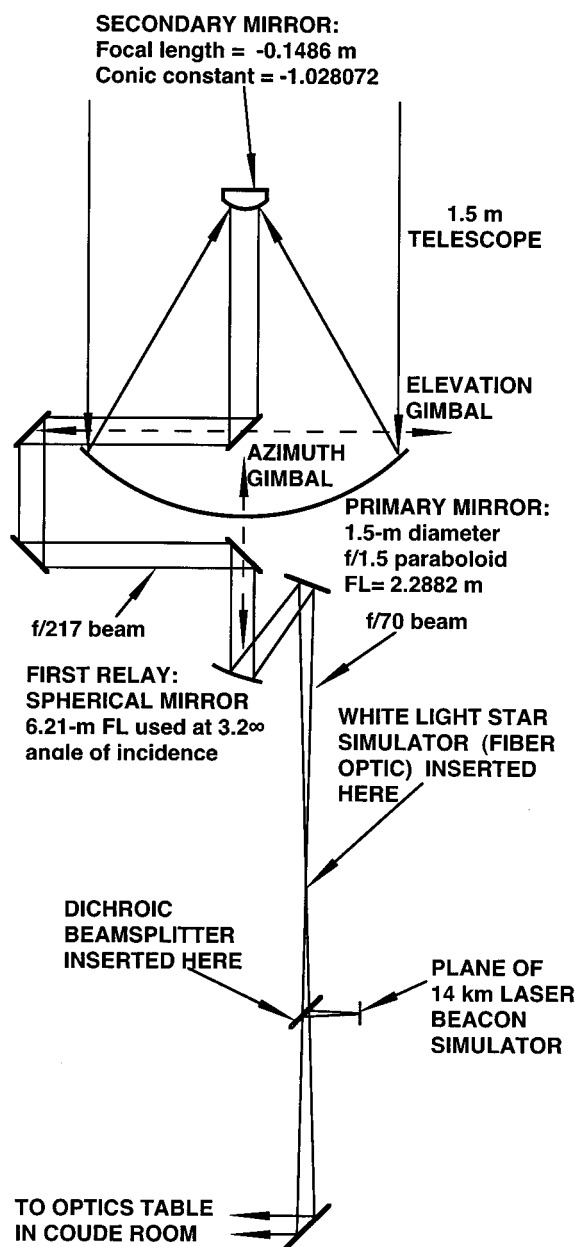


FIG. 24. Telescope and relay optics. The $f/217$ beam out of the telescope is relayed at $f/70$ by a spherical focusing mirror below the telescope. Removable source simulators can be placed in the path at equivalent distances of infinity for natural stars and 10–14 km for artificial laser guide stars. The pedestal area is isolated from the coude room by an optical-quality fused-silica window.

at some altitude above the telescope. However, it is very practical for a first system, since the light does not move around on the deformable mirror with pointing and field object (which would potentially create instabilities in the closed-loop operation). Furthermore, for continental sites, most of the turbulence is in the first few kilometers of the boundary layer, and the mirror is, on average, well placed at the pupil.

The deformable mirror is of the continuous-face-sheet variety. It has 341 actuators, but only 241 of these are

enclosed in the image of the pupil. Since the edge of the face sheet of the deformable mirror is unsupported, the actuators outside the pupil are used as a “guard band” to effect a smooth transition in the shape of the mirror’s surface from the actively controlled region inside the pupil to the region outside, where there is no wave-front measurement. The actuators are on a square 7-mm grid and are made from the electrostrictive material lead-magnesium-niobate (Ealey and Washeba, 1990), which has negligible hysteresis and a total stroke of $\pm 2.5 \mu\text{m}$ for an applied voltage of ± 35 volts. The face sheet is 1.5 mm thick and is made from Corning ULE glass. The structure is very stiff, having a resonant frequency of nearly 25 kHz. This mirror has an rms surface figure of approximately 60 nm when it is unpowered. Using a high-resolution interferometer, we have demonstrated that the mirror can be made flat to better than 6 nm rms over its active area of 112 mm.

4. Laser injection and wave-front sensors

The off-axis parabola OAP2 produces an $f/20$ focus after the deformable mirror. A long-wave-pass dichroic beam splitter is placed in the $f/20$ beam and passes light having wavelengths greater than $1.0 \mu\text{m}$ to scientific cameras or other sensors or instruments that operate in the 1.0- to $2.5\text{-}\mu\text{m}$ wavelength region. The long-wavelength cutoff of $2.5 \mu\text{m}$ is set by the transmission of the fused-silica window that isolates the coude room from the telescope pedestal. Light having wavelengths shorter than $1.0 \mu\text{m}$ is reflected from the long-wave-pass beam splitter and encounters the aperture-sharing optics for the copper-vapor laser beam used to generate artificial guide stars. The aperture-sharing elements for the laser consist of a polarizing beam splitter (PBS in Fig. 25) and a quarter-wave plate. The laser is injected into the PBS linearly polarized so that it is reflected into the coude beam train. It then passes through a quarter-wave plate and becomes circularly polarized and is transmitted out the telescope and through the atmosphere to a focus. Over the past few years, we have adjusted the range at which the laser comes to best focus from 10.5 to 14 km, depending on the sensitivity of our wave-front sensor, power of the laser, and transmission of the optics.

Rayleigh backscattered light retains the circular polarization of the transmitted light. When it passes through the quarter-wave plate on the return trip, it becomes linearly polarized again but orthogonal to the initial direction (P vs S polarization) and passes through the polarizing beam splitter to lens L1 (Fig. 25).

The system has two Shack-Hartmann wave-front sensors, one for natural stars and one for the Rayleigh laser beacon formed by the copper-vapor laser. The system is set up in the so-called Fried geometry with actuators at the corners of the subapertures. The details are shown in Fig. 26.

The lens L1 and off-axis parabola OAP2 form an imaging telescope that, in conjunction with the relay optics in the two wave-front-sensor camera optical trains,

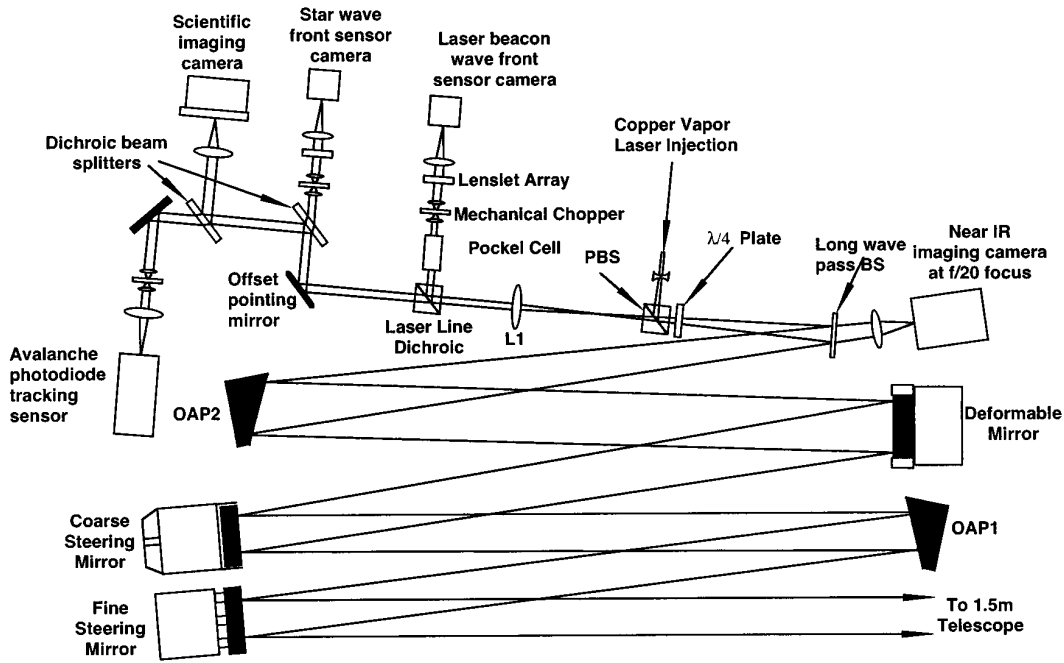


FIG. 25. Schematic diagram of the optics and sensors in the coude room.

forms a 3.2-mm-diameter pupil image on the lenslet array. Each lens in the array is $200\ \mu\text{m}$ square and has a focal ratio of $f/32$. The pixels in the 64×64 charge-coupled-device array are $24\ \mu\text{m}$ square. A subarray of

4×4 pixels are assigned to each subaperture, so that on the CCD array the distance between subapertures is $96\ \mu\text{m}$. Consequently a relay lens with a magnification of $96/200=0.48$ is used between the focal plane of the lenslet array and the CCD array. This relay lens is mounted on a piezoelectric-driven XY stage, which is used to boresight the wave-front sensor (remove full-aperture tilt) with the track sensor so that there is on average no full-aperture tilt on the wave-front sensor.

As shown in Fig. 25, mechanical choppers are used in front of the two wave-front sensors and the avalanche photodiode tracking sensor. These choppers are disks rotating at 384 revolutions per second and have an 80% duty factor. They are carefully synchronized to the laser pulse rate so that scattered light from each laser pulse is mechanically blocked from the three sensors until the pulse is 5 km from the telescope. There is adequate spectral isolation in the star wave-front sensor ($0.7\text{--}0.85\ \mu\text{m}$) and the avalanche photodiodes ($0.85\text{--}1.0\ \mu\text{m}$) to prevent contamination from Rayleigh scattering of the laser beacon (0.510 and $0.578\ \mu\text{m}$) when it is at ranges greater than 5 km. A sharp range gate (resolution of 15 m) is created by the Pockels cell (see Fig. 25).

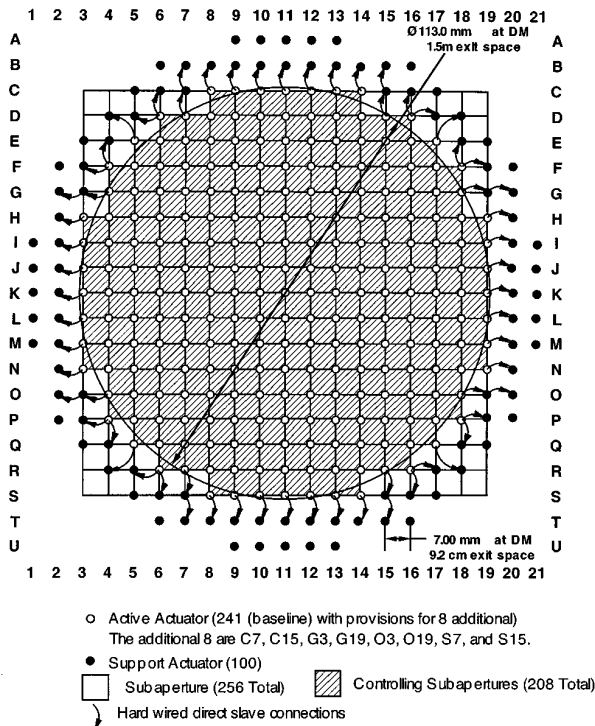


FIG. 26. Relationship of the wave-front sensor subapertures and deformable-mirror actuators.

5. Data-processing algorithms

The real-time processing of the data in this system involves digital manipulation of wave-front sensor data in the wave-front sensor processor, the reconstructor, and the low-pass filter. This is finally converted to analog drive signals for the deformable-mirror actuators. The functions of each step in this flow are (1) compute subaperture gradients, (2) compute phases at the corners of each subaperture, (3) low-pass-filter the com-

puted phases, and (4) provide actuator offsets to compensate for fixed optical-system errors and real-time actuator commands for dynamic wave-front corrections of turbulent distortions.

The wave-front sensor processor performs data formatting, individual pixel calibrations, and comparison of computed real-time wave-front gradients with reference gradients stored in memory. The reference gradients are determined differently for the star and laser-beacon sensors. For the star wave-front sensor, a very high-quality wave front is created by a removable fiber-optic source on the coudé-room optics table. The wave-front generated by this source is the most accurate plane wave we know how to create at the entrance aperture to the star wave-front sensor. The gradients computed by the wave-front processor for this plane wave are stored in the processor's memory so that they can be subtracted from the measured atmospheric data. The difference between the measured and reference gradients represents an error signal that needs to be driven to zero by adjusting the actuators of the deformable mirror.

In the case of the laser-beacon wave-front sensor, it is difficult to create in the laboratory a reference wave front that accurately represents all the geometrical effects associated with the length and breadth and range of the laser beacon as it appears in the atmosphere. The technique that we have developed for making a reference for the laser-beacon wave-front sensor is the following. We first close the adaptive-optics loop on a star using the star wave-front sensor. We then propagate the laser beacon toward the star and collect laser-beacon wave-front data using the laser-beacon wave-front sensor. We typically average several hundred frames of these data to generate a reference for the laser-beacon wave-front sensor. Since the adaptive-optics loop is closed on a natural star during these measurements, the laser-beacon wave-front sensor is viewing the laser-beacon as it would be for the best possible performance of the system. Any focus introduced by the finite range of the beacon is automatically corrected by this technique. Furthermore, edge effects caused by the finite extent of the beacon are measured directly. The laser-beacon reference created by this measurement technique represents the best method we know for maximizing performance of the system. Once the reference is computed, it is loaded into the laser-beacon processor so the loop can be closed using the laser beacon.

6. Electronics

The real-time wave-front reconstructor is based on a previously reported design and uses a parallel array of 256 multiple-accumulator processors. The reconstructor performs a full-matrix multiplication of a 512×256 reconstructor matrix and a (1×512) vector of gradients generated by the wave-front sensor processor. The wave-front sensor measures slopes s over each subaperture. We can easily form a matrix H based on the geometrical relation of the subapertures and deformable-

mirror actuators that relates the vector of measured slopes to the vector of phases ϕ that satisfies the matrix equation

$$s = H\phi. \quad (107)$$

The least-squares estimate of the phase is given by Eq. (91) with the measurement noise σ_n^2 assumed to be zero:

$$\phi = [(H^T H)^{-1} H^T] s = M_{LS} s. \quad (108)$$

The reconstructor matrix M_{LS} is computed well ahead of the time it is needed and down-loaded into the random-access memory of the reconstructor electronics during system initialization.

The output phase data computed from each wave-front sensor measurement by the reconstructor is passed through a digital low-pass filter having programmable gain G and RC time constant τ . The values of G and τ can be adjusted easily by the operator to optimize the performance of the system as the strength and speed of the turbulence changes.

The final mirror-actuator commands are determined by summing the output of the low-pass filter with offset values representing a "system-flat" condition for the deformable mirror. The actuator commands needed for the system flat are determined by iteratively measuring the error signal at the wave-front sensor using the star simulator in the telescope pedestal, computing the wave-front error and applying the actuator commands to eliminate the error, repeating the wave-front measurement to refine the error estimate, updating the actuator commands, and so on until the error is minimized. The resulting actuator commands are saved in the offset file for future use. We have found it necessary to update the static offset commands (to make a new system flat) approximately once per year.

Many diagnostic signals are available for recording while the system is in operation. These include wave-front sensor focal-plane-camera intensity data, computed subaperture gradients, reconstructed phases, low-pass-filter response, and actuator command signals.

7. Scientific and engineering cameras

We have two charge-coupled-device cameras that can be positioned at the output of the adaptive-optics system at plate scales appropriate for the technical objective at hand. One camera is a 64×64 pixel array that can collect data at nearly 2000 frames per second and store it in a computer for 10 seconds (164 Mbytes of data). The exposure time and framing format is readily adjustable by the observer. We also have a 512×512 pixel CCD camera with low-noise readout for long-exposure, high-resolution, scientific images. Both of these cameras are used extensively to obtain engineering data that can be analyzed to assess the performance of the system.

8. Examples of engineering data

Stars make excellent objects by which to assess the engineering performance of the adaptive-optics system. In this section we present example star images, which

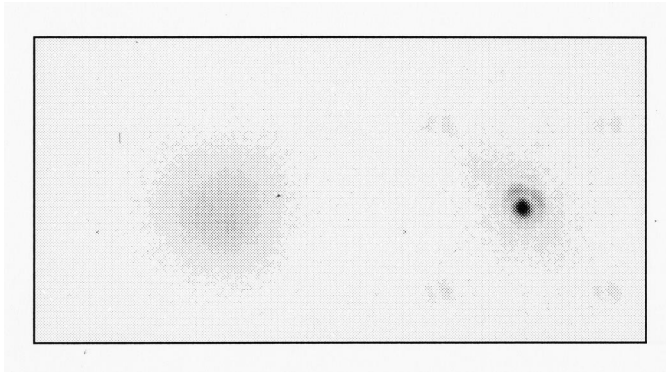


FIG. 27. Uncompensated (left) and compensated (right) images of a bright star made with 20-second exposures of an attenuated CCD camera. Relative intensities are 190 for the uncompensated images and 3120 for the compensated images. The Strehl ratio of the compensated image is 0.62, full width at half maximum is 0.14 arcsec, and the imaging wavelength is 880 nm. The star was used as the beacon (natural-guide-star adaptive optics).

are analyzed and compared with performance predictions based on the system design and atmospheric conditions present when the data were collected.

Figure 27 shows two inverted-gray-scale images of a bright star made with and without adaptive optics. The images are shown logarithmically scaled in order that the uncompensated image on the left be detectable in print. The exposure time was 20 seconds for both images. The peak intensity of the compensated image is 16.4 times brighter than the uncompensated image, and the full-width-at-half-maximum image size of 0.14 arcsec is 6.2 times smaller than the uncompensated image. The imaging wavelength was 880 nm through a 50-nm band-pass filter. The Strehl ratio of the compensated image is 0.62. Figure 28 is a linear surface plot of these same two

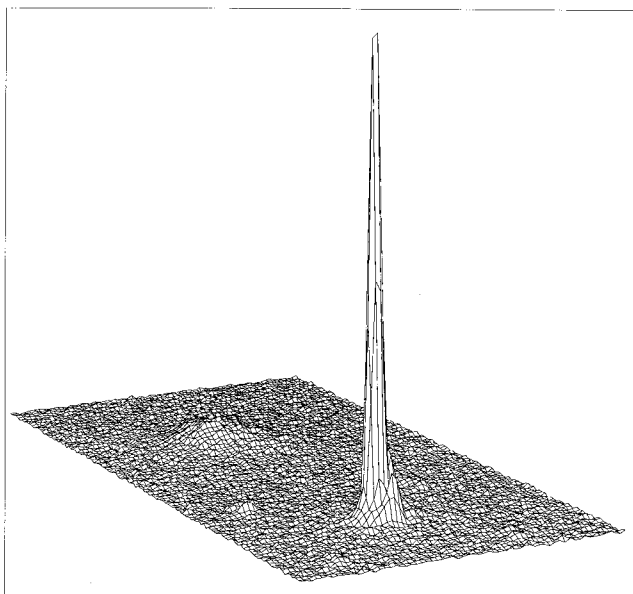


FIG. 28. Surface plot of the images shown in Fig. 27.

images, which shows rather dramatically the improvement in the Strehl ratio made possible with the adaptive optics.

These images were acquired at a zenith angle of 31° , the Greenwood frequency f_G was measured at 47 Hz, and the Fried coherence diameter was 7.9 cm (scaled to 500 nm at zenith). The bandwidth of the higher-order loop was 80 Hz measured at -3 dB error rejection and the closed-loop full-aperture-tilt-correction bandwidth was approximately 150 Hz, producing a one-axis rms error of 90 nrad.

The careful observer will notice four dim spots in a square pattern centered on the compensated image (this is visible in the gray-scale image and the linear three-dimensional plot). These spots are the result of diffraction created by a “waffle” pattern on the deformable mirror. The waffle pattern is created when actuators are alternately up and down relative to the average surface. This mode on the deformable mirror is unsensed by the wave-front sensor due to the fact that the actuator spacing exactly matches the subaperture dimension. Since the mode is unsensed, it is not suppressed by the control loop and can come and go unpredictably. Also the reconstructor matrix mathematically projects waffle mode out of the reconstructed wave front. However, it is only possible to make the net waffle in the reconstructed wave front zero. If there are pockets of waffle all over the mirror that have a change of sign at boundaries, the net waffle can still be zero mathematically, but the diffraction effects will be seen in the image. These effects can be controlled somewhat with careful design of reconstructors. It is also possible to suppress these modes by observing the deformable mirror with a high-resolution local-loop interferometer and using its output to suppress undesired modes by appropriately injecting control signals in the servo loop.

It is interesting and important to compare an estimate of the Strehl ratio with that measured from the two-dimensional modulation transfer function of the compensated image in Fig. 27. We can estimate the Strehl ratio from scaling laws as the product of errors due to fitting, wave-front-measurement noise, control-loop servo lag, and tracking errors. These errors are due, respectively, to the finite number of actuators, finite signal-to-noise ratio in the wave-front measurement, noise propagation in the wave-front reconstruction process, the finite bandwidth of the closed-loop servo due to the finite readout time of the CCD in the wave-front sensor and processor delays, and imperfect correction of full-aperture tilt.

Expressions for the variances of these errors are well known and summarized as follows. The fitting error is given as

$$\sigma_{fit}^2 = 0.28 \left(\frac{d}{r_0} \right)^{5/3} = 0.28 \left(\frac{0.092}{0.127} \right)^{5/3} = 0.164 \text{ rad}^2, \quad (109)$$

where d is the subaperture diameter. The servo-lag error was previously given in Eq. (103) and is 0.184 rad^2 for $f_G = 29$ Hz and $f_{3 \text{ dB}} = 80$ Hz. The wave-front variance due to wave-front measurement noise is negligible in

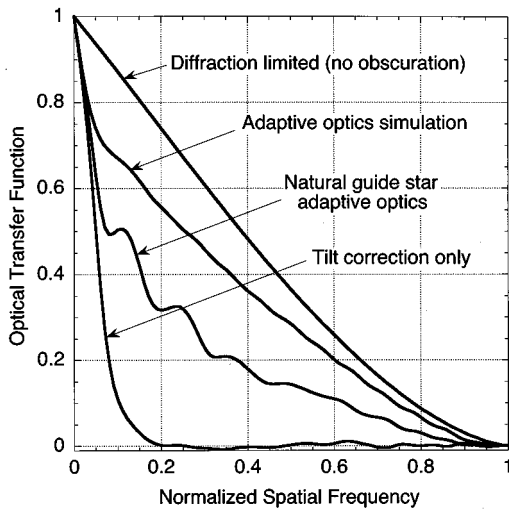


FIG. 29. Modulation transfer functions. Diffraction-limited aperture, simulated adaptive-optics system, experimentally measured adaptive-optics system, and tilt-only correction.

this case, since we were using a very bright star. The Strehl ratio due to tracking errors is given by

$$\begin{aligned}
 S_{\text{track}} &= \left[1 + \frac{\pi^2}{2} \left(\frac{\sigma_{\theta} D}{\lambda} \right)^2 \right]^{-1} \\
 &= \left[1 + \frac{\pi^2}{2} \left(\frac{90 \times 10^{-9} \times 1.5}{0.88 \times 10^{-6}} \right)^2 \right]^{-1} \\
 &= 0.89,
 \end{aligned} \tag{110}$$

where σ_{θ} is the one-axis rms full-aperture tracking error, D is the full-aperture diameter, and λ is the imaging wavelength. In these formulas, the values of f_G and r_0 have been scaled to the imaging wavelength of 880 nm.

The resultant Strehl ratio is given by

$$S_{\text{total}} = \exp[-(0.164 + 0.184)] \times 0.89 = 0.63. \tag{111}$$

This is remarkably (fortuitously?) close to the measured value of 0.62.

Figure 29 is the modulation transfer function (MTF), computed from two-dimensional Fourier transforms of the images shown in Fig. 27. Also shown in Fig. 29 are the unobscured-aperture diffraction-limited MTF and the MTF computed from a simulation of the adaptive-optics system [similar to that described by Ellerbroek (1994)]. Considering the complexity of these systems and the uncertainty in the measurement of atmospheric parameters, the agreement between the simulation and the measured data is reasonable. It is also important to note that some response exists even at the highest spatial frequencies. If the signal-to-noise ratio in the image is high enough, post-signal processing techniques, discussed later in Secs. VI and VII in this review, are likely to be successful in recovering a high-contrast diffraction-limited image.

As discussed in Sec. III.A.1, we expect focus anisoplanatism associated with laser beacons to degrade the performance of the adaptive optics obtained with

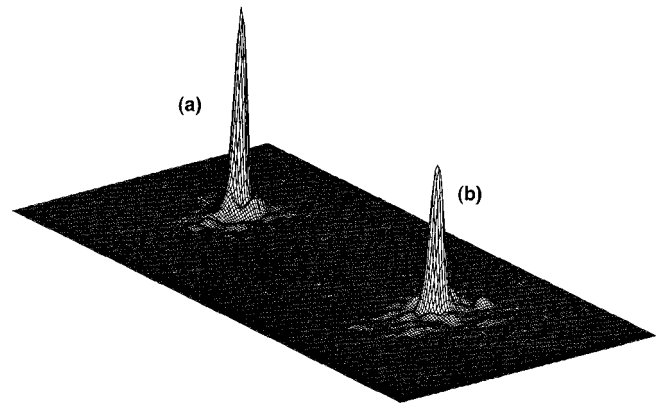


FIG. 30. Short-exposure images obtained with natural guide star (a) and laser guide star (b).

natural guide stars. Figure 30 shows three-dimensional intensity profiles of two short-exposure images of a star obtained by using the star itself as the beacon for the adaptive optics [image labeled (a)] and using the copper-vapor laser beacon [image labeled (b)]. These images are 10-ms exposures at a wavelength of 880 nm. The image (a) has a Strehl ratio of 0.59 and a full-width-at-half-maximum intensity of 0.13 arcsec. The image (b) has a Strehl ratio of 0.48 and a full-width-at-half-maximum intensity of 0.13 arcsec. Note the differences in the peak intensities and the distribution of light in the halo region surrounding the peak. The relative performance of natural-guide-star vs laser-guide-star compensation depends critically on the upper-atmospheric turbulence conditions present and the height of the laser beacon.

The performance of the laser-beacon adaptive-optics system is illustrated in Fig. 31, which contains images of the binary star β -Del. These are one-minute exposures. The track loop was closed during both exposures, so the left image does include tilt compensation. The laser-beacon adaptive optics provided higher-order compensation in the right image. The angular separation of the two stars is 0.199 arcsec when this image was made (Sept. 1993), and the full-width-at-half-maximum intensity for each star is 0.14 arcsec. The peak intensity is 384 counts for the uncompensated image and 3260 for the laser-beacon-compensated image. These are raw-data images—no post processing of any kind has been done.

9. Scientific images

We conclude this section with two examples of images that have been used to obtain new science. The first is of the Trapezium region in the Orion nebula. Figure 32 shows three views of the Trapezium—a region known for young-star formation. The left two images were made through a 656.3-nm hydrogen-alpha filter (light generated by ionized hydrogen) and the right image through a continuum filter at 647.0 nm. The increased detail in the morphology of this region is immediately

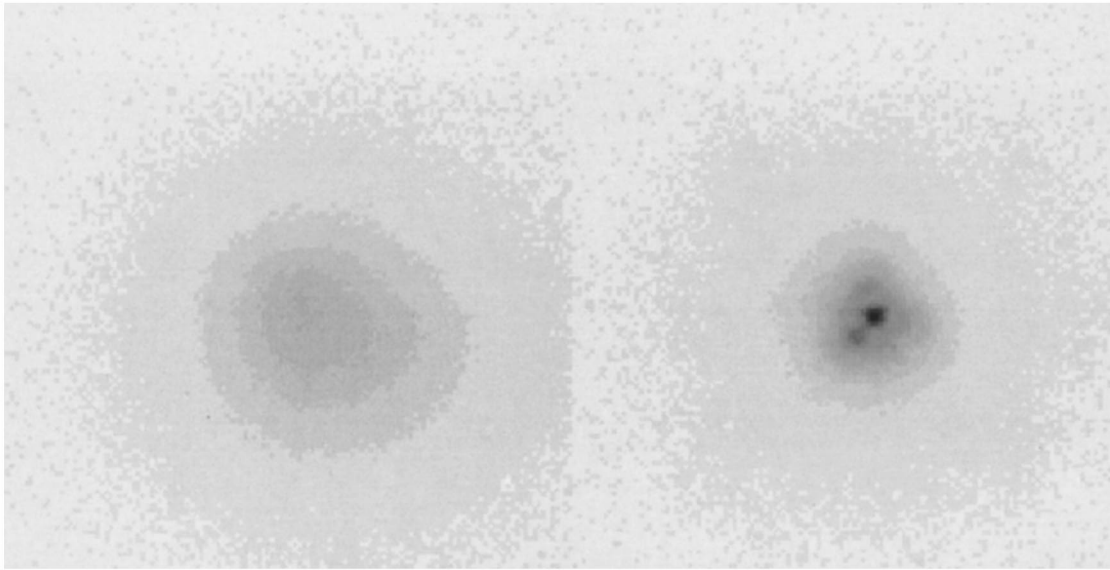


FIG. 31. Images of the binary star β -Delphinius obtained with laser-beacon adaptive optics. The uncompensated image is on the left, and the image obtained with the laser-beacon adaptive optics is on the right. Details are discussed in the text.

apparent when comparing the left two images. The use of the hydrogen-alpha filter shows immediately the presence of ionized hydrogen. Everything that is visible in the center image but not in the right image is basically ionized hydrogen. The source of the ionization is most likely the bright O star in the center of the image, designated θ^1 C Ori. On closer examination, one can see cometlike structure in the objects in the center image. The tails of the “comets” point away from the center star, indicating a strong stellar wind being generated by θ^1 C. The objects seen in the center image but not in the right image are new stars being formed from gravitational collapse of hydrogen in the nebula. However, there is a competing process, since the wind from θ^1 C is also ripping these hydrogen clouds apart. Additional details of these images and significant scientific conclusions are reported by McCullough *et al.* (1995).

Another example is shown in Fig. 33. This is an image of Saturn obtained July 23, 1994 at 10:35 UTC (Universal Time Convention). A specialized near-infrared imaging correlation tracker was used for full-aperture tilt compensation, and the laser-beacon adaptive optics was used for higher-order correction. The laser propagation direction was centered on the planet. The image encompasses a wide spectral band from 0.65 to 0.95 μm and was a three-second exposure. When displayed on the computer, the fine structure in the rings is striking and clearly shows the crepe inner ring, the Cassini and Encke divisions at the outer edge. The polar caps are also quite visible in the atmosphere as are several bands. Some image processing hints at an atmospheric storm near the equator (not visible in this unprocessed image). The moon Rhea is visible under the rings to the lower left, and its shadow cast on the lower right edge of the

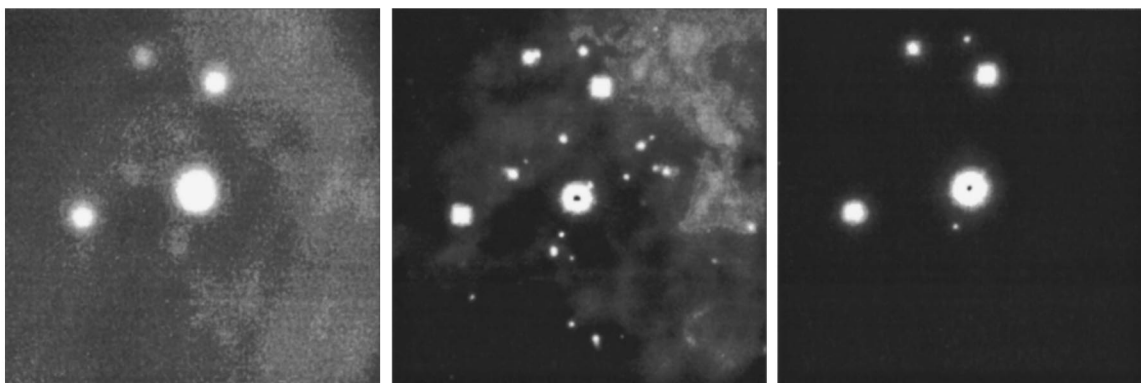


FIG. 32. Images of the Trapezium new-star forming region in the Orion nebula. The left two images were made through a hydrogen-alpha filter (656.3 nm) and the right image through a continuum filter (647.0 nm). The right two images were compensated with laser-beacon adaptive optics. The exposures were 4 minutes each and the field is 40 arcsec square. The scientific content is discussed in the text.

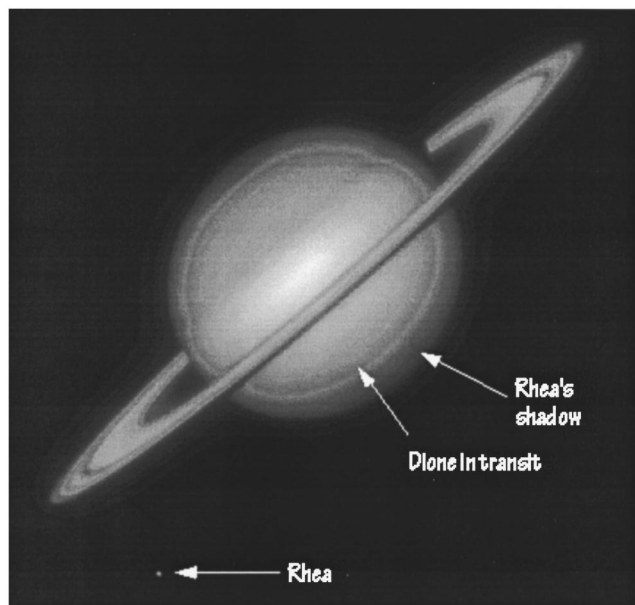


FIG. 33. Image of the planet Saturn obtained with laser-beacon adaptive optics. The laser was directed to the center of the planet. Tracking was provided by an imaging correlation tracker operating in the near infrared. Note the detail in the ring structure, the atmosphere, and the shadow cast on the lower-right surface of the planet by the small moon Rhea, visible to the left of the planet.

planet is also quite visible. The moon Dione is also seen in front of the planet during transit. Additional information on the engineering and scientific aspects of Saturn images can be found in the work of Fugate *et al.* (1996).

This technique was also used with a tunable very narrow spectral filter operated by the NASA Goddard Space Flight Center to investigate the impact of the Shoemaker-Levy comet on Jupiter and to measure the surface features of Titan through its hazy atmosphere. Data analysis is still underway from those observations.

IV. SPECKLE IMAGING

The first efforts to overcome the effects of atmospheric turbulence relied purely on post-detection processing of short-exposure images measured through turbulence. Pure post-processing techniques are now referred to as *speckle-imaging* methods, in reference to the speckled appearance of the measured images. In speckle imaging a high-resolution image of the object is not measured directly. Rather, an estimate of the Fourier transform of the object is computed, and an image is obtained by the inverse-Fourier-transform operation. Speckle imaging is not a single technique, but rather a collection of post-processing techniques for recovering an estimate of both the modulus and the phase of the Fourier transform of the object. An estimate of the object is then obtained by applying the inverse Fourier transform to the spectral data. Topics related to speckle imaging have been reviewed by Dainty (1975); Labeyrie

(1976, 1978); Bates (1982); Roddier (1988b); Aleksoff *et al.* (1993); Beckers (1993).

All of the techniques used in speckle imaging arise from Labeyrie's observation that the speckles in short-exposure images contain more high-spatial-frequency information about the object than long-exposure images (Labeyrie, 1970). In his seminal paper Labeyrie proposed a method for estimating the modulus of the Fourier transform of an object, also referred to as the modulus spectrum of the object. Labeyrie's technique is today referred to as speckle interferometry. However, the phase of the Fourier transform of an object, often referred to as the phase spectrum of the object, is needed for applications where an image is required. The two most widely used methods for estimating the phase spectrum of an object are referred to as the Knox-Thompson or cross-spectrum method (Knox and Thompson, 1974) and the bispectrum method (Lohmann *et al.*, 1983). Neither the Knox-Thompson nor the bispectrum method can provide a direct estimate of the phase spectrum of the object. Rather they provide quantities which contain linear combinations of the elements of the phase spectrum of the object. A distinct operation is required to reconstruct the object phase spectrum from the cross spectrum or bispectrum.

A. Overview of speckle imaging

In this section we qualitatively describe speckle imaging and provide the foundation for the algorithms presented in the succeeding sections. The speckle-imaging technique is shown in block diagram form in Fig. 34. Two sets of image data are required to perform speckle imaging: (1) a set of N short-exposure images of the object of interest, with the n th image of the object denoted by $i_n(\vec{x})$, and (2) a set of M short-exposure images of a bright nearby reference star, with the m th image of the reference star denoted by $r_m(\vec{x})$. The size of the data sets is generally driven by signal-to-noise-ratio considerations, with typical values of N and M on the order of a several tens to a few thousand. Exposure times on the order of a few milliseconds to a few tens of milliseconds are commonly used with the goal of freezing a single realization of the turbulence during the exposure time. All correction for turbulence effects is accomplished by the speckle-imaging estimators. In practice, the brightest possible reference star is used, to insure that the signal-to-noise ratio of the reference data be much higher than the signal-to-noise ratio of the object data. It is also good practice to measure the reference-star data immediately before or after the object data is measured to maximize the likelihood that the atmospheric statistics for the object and the reference-star data are the same.

The first step in post processing is to compute the Fourier transform of the images $i(\vec{x})$, denoted by $I(\vec{f})$. The Fourier transform is, in general, a complex quantity, which has modulus $|I(\vec{f})|$ and phase $\phi_i(\vec{f})$ given by

$$I(\vec{f}) = |I(\vec{f})| \exp[i\phi_i(\vec{f})]. \quad (112)$$

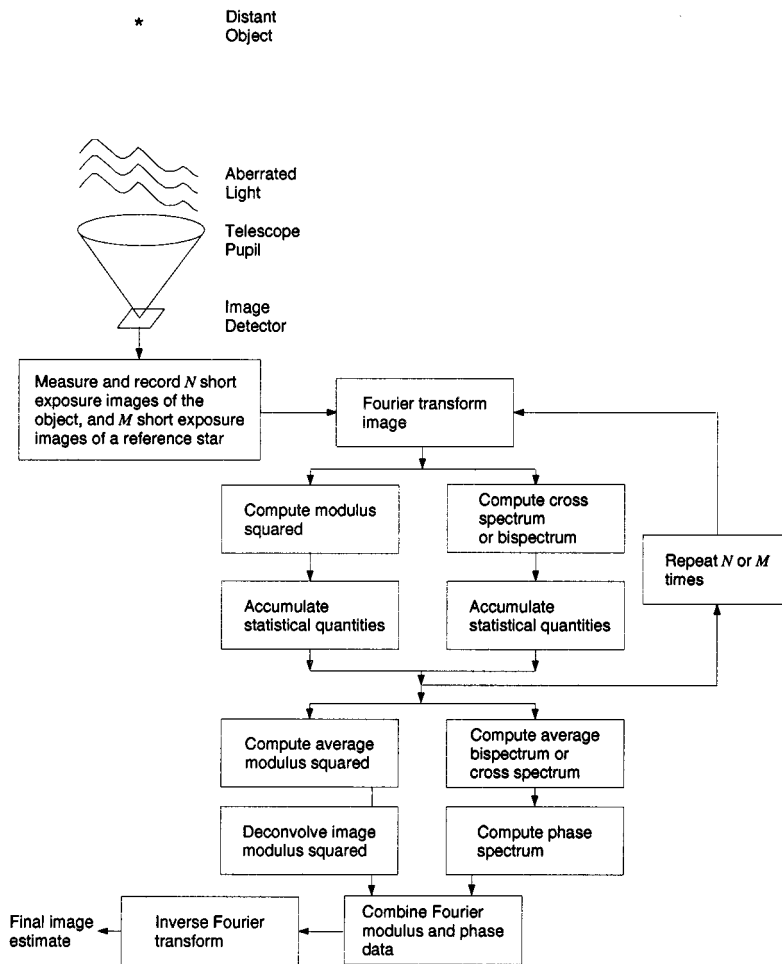


FIG. 34. Block diagram for speckle imaging.

Two processing steps are performed on the Fourier-transformed images. One step is to estimate the average modulus squared, or second moment of the Fourier transform of the object data and the reference-star data. These quantities are denoted by $\langle |I(\vec{f})|^2 \rangle$ for the object data and $\langle |R(\vec{f})|^2 \rangle$ for the reference-star data. The second moment of the image spectrum is of interest in speckle imaging. The spectrum of the object irradiance distribution $O(\vec{f})$ is constant, while $I(\vec{f})$ is random due to turbulence-induced random fluctuations in the optical transfer function $\mathcal{H}(\vec{f})$. Computing the average modulus squared of $I(\vec{f})$ yields the following relationship:

$$\langle |I(\vec{f})|^2 \rangle = |O(\vec{f})|^2 \langle |\mathcal{H}(\vec{f})|^2 \rangle. \quad (113)$$

As shown later, the second moment of the OTF is finite out to the diffraction-limited cutoff frequency of the telescope, $D/\lambda d_i$ (Korff, 1973). Hence, if $|O(\vec{f})|^2$ is greater than zero for frequencies approaching the cutoff frequency of the telescope, then the second moment of the image spectrum will contain diffraction-limited information. $\langle |\mathcal{H}(\vec{f})|^2 \rangle$ is referred to as the speckle transfer function. Note that the phase spectrum of the object is lost in computing the second moment of the image. Hence an image cannot be obtained directly from $\langle |I(\vec{f})|^2 \rangle$.

We now consider the requirement for imagery of a reference star. Note that in general $|O(\vec{f})|^2$ is not a constant function of spatial frequency. Rather, $|O(\vec{f})|^2$ takes its maximum value at $|\vec{f}|=0$ and generally diminishes with increasing $|\vec{f}|$. The spectral components of $\langle |I(\vec{f})|^2 \rangle$ are further attenuated by multiplication with $\langle |\mathcal{H}(\vec{f})|^2 \rangle$. An image obtained by inverse-Fourier-transforming such strongly attenuated spectral data would appear badly blurred, even if the spectral data was *perfectly known*. Now consider the case of an unresolved source, such as a distant star, which has an irradiance distribution $r(\vec{x})$ that is proportional to a delta function. The Fourier transform of the reference-star irradiance distribution is, in this case, a constant function of \vec{f} , say C_R . Hence the average modulus squared of the reference-star image spectrum, $\langle |R(\vec{f})|^2 \rangle$, is given by

$$\langle |R(\vec{f})|^2 \rangle = C_R^2 \langle |\mathcal{H}(\vec{f})|^2 \rangle. \quad (114)$$

$\langle |R(\vec{f})|^2 \rangle$ can be normalized to take the value of unity at $|\vec{f}|=0$ to obtain an estimate of the second moment of the OTF, $\langle |\mathcal{H}(\vec{f})|^2 \rangle$. If the ratio of $\langle |I(\vec{f})|^2 \rangle$ and the normalized version of $\langle |R(\vec{f})|^2 \rangle$ is now formed, we obtain

$$\frac{\langle |I(\vec{f})|^2 \rangle}{C_R^{-2} \langle |R(\vec{f})|^2 \rangle} = \frac{|O(\vec{f})|^2 \langle |\mathcal{H}(\vec{f})|^2 \rangle}{\langle |\mathcal{H}(\vec{f})|^2 \rangle} = |O(\vec{f})|^2, \quad (115)$$

which is the modulus squared of the object spectrum, the desired quantity. Thus the purpose of collecting and processing reference-star data is to provide a means of calibrating the average modulus squared of the object image spectrum for the effects of the second moment of the transfer function of the combined atmosphere-telescope system. Equation (115) is the essence of Labeurie's speckle-interferometry technique.

The phase spectrum of the object is estimated by computing either the average cross spectrum or the average bispectrum of the images. The cross spectrum and the bispectrum encode the phase of the object spectrum as phase differences. In either case the object phase spectrum must be reconstructed from these phase differences.

B. Speckle interferometry

As discussed in Sec. IV.A, speckle interferometry is a technique for estimating the modulus of the Fourier transform of an object from a set of speckled images of the object. In this section we establish two key points required to understand speckle interferometry: (1) the atmosphere-telescope system allows diffraction-limited

information to be present in the second moment of the image spectrum, and (2) the signal-to-noise-ratio considerations make speckle interferometry a practical technique.

1. Speckle transfer function

As indicated in Eq. (113), the average performance of speckle interferometry depends critically upon the speckle transfer function, $\langle |\mathcal{H}(\vec{f})|^2 \rangle$. In this subsection $\langle |\mathcal{H}(\vec{f})|^2 \rangle$ is shown to have finite value at high spatial frequencies. The analysis presented here is based on the geometrical-optics model for wave propagation through the atmosphere. This model for wave-front propagation was discussed in Sec. II.B. The phase fluctuation in the aperture plane arising from propagation through the atmosphere is denoted by $\psi(\vec{x})$. The second moment of the optical transfer function may be written as

$$\langle |\mathcal{H}(\vec{f})|^2 \rangle = N_F^{-2} \left\langle \left| \int d\vec{x} W(\vec{x}) W(\vec{x} - \vec{f}\lambda d_i) \times \exp\{i[\psi(\vec{x}) - \psi(\vec{x} - \vec{f}\lambda d_i)]\} \right|^2 \right\rangle, \quad (116)$$

where N_F is a normalizing constant given by $N_F = \int d\vec{x} |W(\vec{x})|^2$. The expression in Eq. (116) can be evaluated analytically (Korff, 1973; Goodman, 1985; Roggemann and Welsh, 1996) with the result

$$\langle |\mathcal{H}(\vec{f})|^2 \rangle = N_F^{-2} \int d\vec{x} \int d\vec{x}' W(\vec{x}) W(\vec{x} - \vec{f}\lambda d_i) W(\vec{x}') W(\vec{x}' - \vec{f}\lambda d_i) \times \exp \left\{ -D_\psi(|\vec{f}\lambda d_i|) - D_\psi(|\vec{x} - \vec{x}'|) + \frac{1}{2} D_\psi(|\vec{x} - \vec{x}' + \vec{f}\lambda d_i|) + \frac{1}{2} D_\psi(|\vec{x} - \vec{x}' - \vec{f}\lambda d_i|) \right\}. \quad (117)$$

The results of a numerical evaluation of Eq. (117) for a circular aperture are presented in Fig. 35 for $D/r_0 = 2, 5, 10,$ and 15 . The horizontal axis of Fig. 35 is expressed in terms of the normalized spatial frequency, $(f_x \lambda d_i / D)$, where f_x is one orthogonal component of the spatial frequency vector \vec{f} . Note that $\langle |\mathcal{H}(\vec{f})|^2 \rangle$ is greater than 10^{-3} out to normalized spatial frequencies of greater than 0.7 for $D/r_0 = 10$. This result can be compared to the normalized spatial frequency at which the mean optical transfer function $\langle \mathcal{H}(\vec{f}) \rangle$ essentially goes to zero. Inspection of Fig. 9 shows that, for $D/r_0 = 10$, $\langle \mathcal{H}(\vec{f}) \rangle$ goes to zero at a normalized spatial frequency of less than 0.15 . Thus we conclude that speckle-interferometry measurements will provide higher-spatial-frequency information than conventional long-exposure imaging through turbulence.

The discussion in this subsection demonstrates that the speckle-interferometry method can, on average, provide high-spatial-frequency information about objects imaged through turbulence. However, the analysis pre-

sented thus far does not address the *fidelity* of the data. A detailed analysis of the effects of randomness arising from both turbulence and measurement noise, leading to an expression for the signal-to-noise ratio for speckle interferometry, is required. In the next subsection this analysis is presented.

2. Signal-to-noise-ratio considerations

Since speckle interferometry is a frequency-domain technique, the signal-to-noise-ratio analysis has been conducted in the Fourier-transform domain of the measured images. Two fundamental sources of randomness are present in the measured images: (1) turbulence-induced randomness in the OTF, or, equivalently, in the point-spread function, and (2) randomness due to the random locations and arrival times of photoevents in the image plane, referred to as photon noise. Because of photon noise, the second moment of the measured image spectrum is not directly proportional to the modulus

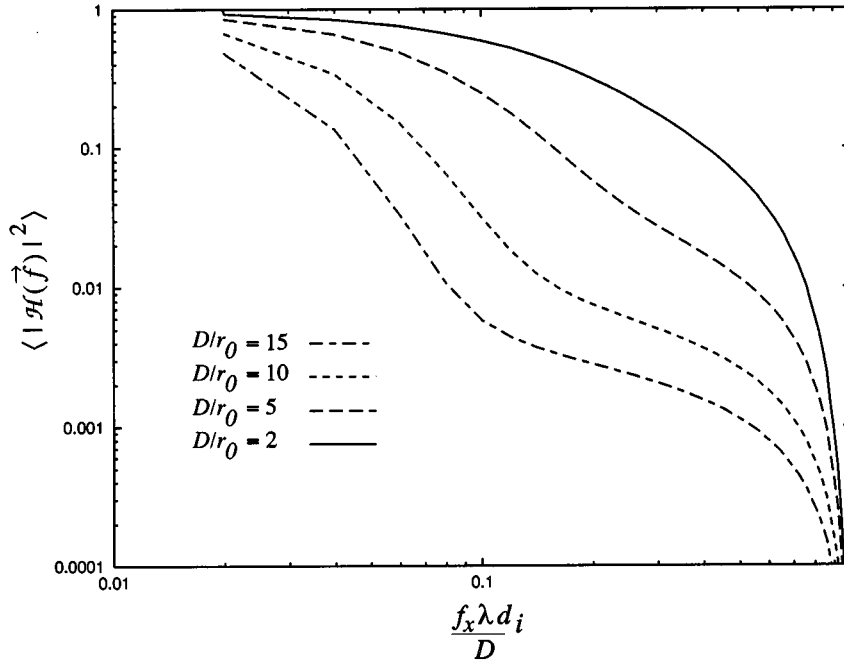


FIG. 35. Second moment of optical transfer function for various values of D/r_0 . The horizontal axis is normalized to the diffraction-limited cutoff frequency $D/\lambda d_i$.

squared of the object spectrum, $|O(\vec{f})|^2$. Rather, a photon-noise bias is present, which must be removed in the data processing.

The bias-removal approach most widely used was proposed by Dainty and Greenaway (1979). An alternative bias-removal approach (Goodman and Belsher, 1977; Goodman, 1985) was shown to have lower signal-to-noise ratio than Dainty's technique. The unbiased speckle-interferometry estimator of Dainty and Greenaway, $Q(\vec{f})$, is given by

$$Q(\vec{f}) = |D(\vec{f})|^2 - K, \quad (118)$$

where K is the actual number of photoevents detected per image, and the notation $D(\vec{f})$ is the photon-noise-corrupted detected spectrum of the image as defined in Eq. (55). The mean of $Q(\vec{f})$ is given by

$$\langle Q(\vec{f}) \rangle = (\bar{K})^2 \langle |\mathcal{H}(\vec{f})|^2 \rangle |O_n(\vec{f})|^2. \quad (119)$$

The relevant signal-to-noise ratio for speckle interferometry is thus the signal-to-noise ratio of $Q(\vec{f})$, given by

$$\text{SNR}_{Q(\vec{f})} = \frac{\langle Q(\vec{f}) \rangle}{\text{var}\{Q(\vec{f})\}^{1/2}}. \quad (120)$$

The variance of $Q(\vec{f})$ has been evaluated with the result (Dainty and Greenaway, 1979; Roggemann and Welsh, 1996)

$$\begin{aligned} \text{var}\{Q(\vec{f})\} &= (\bar{K})^2 + (\bar{K})^2 |O_n(2\vec{f})|^2 \langle |\mathcal{H}(2\vec{f})|^2 \rangle \\ &\quad + 2(\bar{K})^3 |O_n(\vec{f})|^2 \langle |\mathcal{H}(\vec{f})|^2 \rangle \\ &\quad + (\bar{K})^4 |O_n(\vec{f})|^4 [\langle |\mathcal{H}(\vec{f})|^4 \rangle - \langle |\mathcal{H}(\vec{f})|^2 \rangle^2]. \end{aligned} \quad (121)$$

If additive zero-mean Gaussian noise is present, such as might arise in a charge-coupled-device camera, then $\text{var}\{Q(\vec{f})\}$ is increased by the amount $(P\sigma_n^2)^2$, where P is the number of pixels in the image and σ_n^2 is the variance of the additive noise expressed in photoelectrons. Monte Carlo simulations of imaging through turbulence are often used to evaluate $\langle |\mathcal{H}(\vec{f})|^4 \rangle$ when adaptive optics are present. Such simulations have been used to evaluate these statistics for both uncompensated (that is, no adaptive optics) imaging and compensated imaging using adaptive optics (Roggemann and Matson, 1992).

In the case of uncompensated imaging through turbulence, a simple expression can be obtained for $\langle |\mathcal{H}(\vec{f})|^4 \rangle$. For spatial frequencies, $|\vec{f}| > r_0/\lambda d_i$, the mean optical transfer function is essentially zero. Further, the real and imaginary parts of the OTF are known to be Gaussian-distributed random variables with equal variances for $|\vec{f}| > r_0/\lambda d_i$, so that the Gaussian-moment theorem may be used to write (Papoulos, 1991)

$$\langle |\mathcal{H}(\vec{f})|^4 \rangle = 2 \langle |\mathcal{H}(\vec{f})|^2 \rangle^2, \quad |\vec{f}| > \frac{r_0}{\lambda d_i}. \quad (122)$$

It is shown by Korff (1973) and Dainty and Greenaway (1979) that a simple expression for $\langle |\mathcal{H}(\vec{f})|^2 \rangle$ can be obtained in terms of the telescope diameter D and the Fried seeing parameter r_0 , for frequencies in the range $|\vec{f}| > r_0/\lambda d_i$. This expression is given by

$$\langle |\mathcal{H}(\vec{f})|^2 \rangle = 0.435 \mathcal{H}_0(\vec{f}) \left(\frac{r_0}{D} \right)^2, \quad (123)$$

where $\mathcal{H}_0(\vec{f})$ is the diffraction-limited OTF of the telescope. If attention is limited to frequencies greater than $0.5D/\lambda d_i$, the second term of Eq. (121) is eliminated,

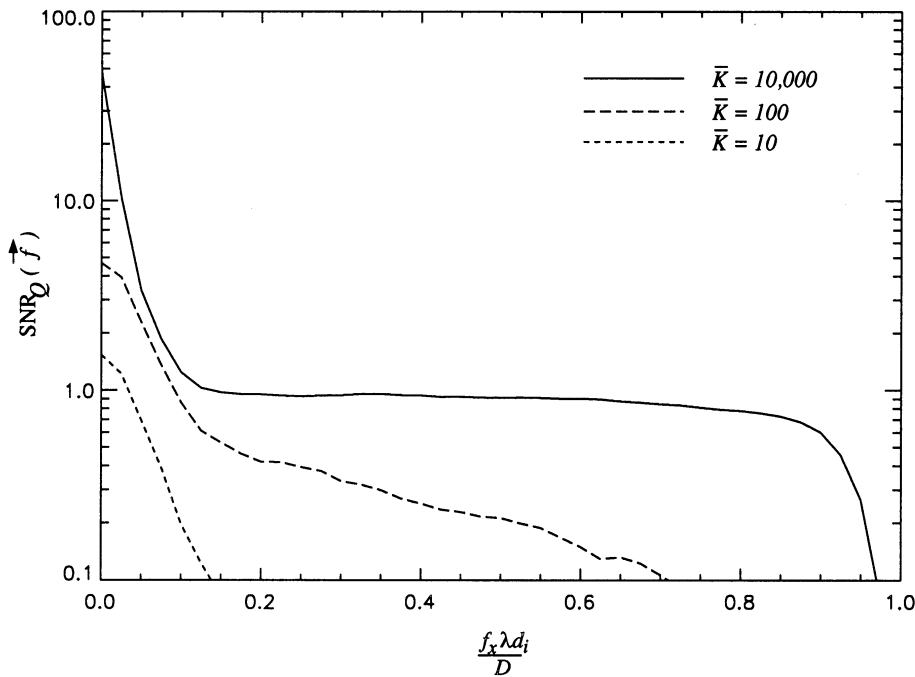


FIG. 36. Signal-to-noise ratio $\text{SNR}_Q(\vec{f})$ for $\bar{K} = 10\,000$, 100, and 10, for the fixed value of $D/r_0 = 10$. The object is an unresolved star, and the horizontal axis is normalized to the diffraction-limited cutoff frequency.

since the speckle transfer function is zero at frequencies greater than the diffraction-limited cutoff. This yields the result

$$\begin{aligned} \text{var}\{Q(\vec{f})\} = & (\bar{K})^2 + 2(\bar{K})^3 |O_n(\vec{f})|^2 \langle |\mathcal{H}(\vec{f})|^2 \rangle \\ & + (\bar{K})^4 |O_n(\vec{f})|^4 \langle |\mathcal{H}(\vec{f})|^2 \rangle^2. \end{aligned} \quad (124)$$

The square root of Eq. (124) can now easily be taken and included in the expression for $\text{SNR}_Q(\vec{f})$ to obtain (Dainty and Greenaway, 1979; Goodman, 1985)

$$\text{SNR}_Q(\vec{f}) = \frac{\bar{K} |O_n(\vec{f})|^2 \langle |\mathcal{H}(\vec{f})|^2 \rangle}{1 + \bar{K} |O_n(\vec{f})|^2 \langle |\mathcal{H}(\vec{f})|^2 \rangle}, \quad |\vec{f}| > \frac{0.5D}{\lambda d_i}. \quad (125)$$

Note that $\text{SNR}_Q(\vec{f})$ is bounded from above by unity. Hence, even for infinitely bright objects, characterized by $\bar{K} \rightarrow \infty$, the maximum possible $\text{SNR}_Q(\vec{f})$ is unity. For objects with finite \bar{K} , and for extended objects, which have $|O_n(\vec{f})| \ll 1$ at mid and high spatial frequencies, $\text{SNR}_Q(\vec{f})$ is substantially less than one. This is a considerable practical impediment to performing speckle interferometry. To boost $\text{SNR}_Q(\vec{f})$, many independent realizations of $Q(\vec{f})$ must be averaged. Such averaging boosts $\text{SNR}_Q(\vec{f})$ according to

$$\text{SNR}_Q^N(\vec{f}) = \sqrt{N} \text{SNR}_Q(\vec{f}), \quad (126)$$

where N is the number of independent realizations averaged and the notation $\text{SNR}_Q^N(\vec{f})$ is used to represent the signal-to-noise ratio of the averaged $Q(\vec{f})$. Practical values of N range from a few hundred to several thousand.

Examples of the behavior of $\text{SNR}_Q(\vec{f})$ obtained using simulations described by Roggemann and Welsh (1996) are shown in Figs. 36 and 37. Note that the simulation was used to provide an estimate of $\text{SNR}_Q(\vec{f})$ to generate Figs. 36 and 37. In both figures the object of interest is an unresolved star. In Fig. 36 $\text{SNR}_Q(\vec{f})$ is plotted for $\bar{K} = 10\,000$, 100, and 10, for the fixed value $D/r_0 = 10$. In Fig. 37 $\text{SNR}_Q(\vec{f})$ is plotted for $D/r_0 = 5, 10$, and 20 for the fixed value $\bar{K} = 1000$. Examining the $\bar{K} = 100$ curve in Fig. 36 shows that $\text{SNR}_Q(\vec{f})$ at a normalized spatial frequency of 0.5 is approximately 0.2. Thus to obtain an $\text{SNR}_Q(\vec{f})$ of unity at this frequency would require averaging approximately 25 independent frames.

C. Fourier phase estimation techniques

As discussed in the previous section, speckle interferometry provides only the modulus of the Fourier transform of an object. The phase of the Fourier transform is required to construct an image of the object. The Knox-Thompson, or cross-spectrum, method and the bispectrum method are post-detection image-processing techniques for reconstructing the phase spectrum of an object viewed through turbulence. In this section an analysis of the cross-spectrum and bispectrum phase reconstruction techniques is presented.

Two key points must be addressed to understand phase-spectrum estimation using either the cross-spectrum or the bispectrum technique. The first issue is to demonstrate that high-spatial-frequency information related to the object's phase spectrum is present in these specialized moments of the image Fourier transform. The second key issue is phase-spectrum reconstruction.

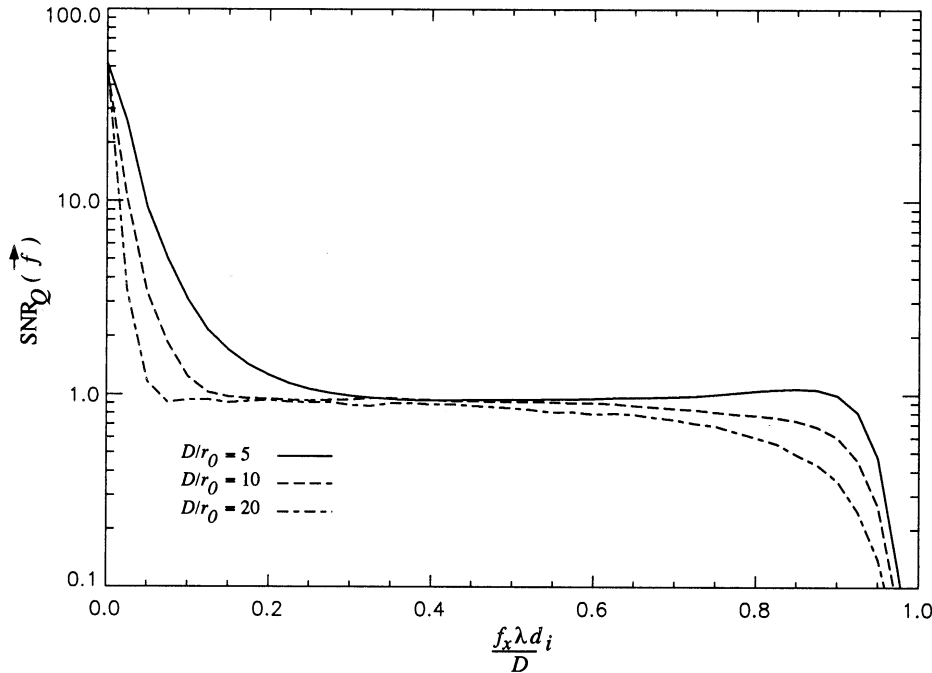


FIG. 37. Signal-to-noise ratio $\text{SNR}_Q(\vec{f})$ for $D/r_0=5, 10,$ and 20 , with the fixed photon-flux level, $\bar{K}=1000$. The object is an unresolved star, and the horizontal axis is normalized to the diffraction-limited cutoff frequency.

Neither the cross spectrum nor the bispectrum approach provides object phase-spectrum information directly. A separate processing step is required to reconstruct the object phase spectrum.

1. Knox-Thompson, or cross-spectrum, technique

The cross spectrum of a single image, $C(\vec{f}, \Delta\vec{f})$, is defined as (Knox and Thompson, 1974)

$$C(\vec{f}, \Delta\vec{f}) = I(\vec{f}) I^*(\vec{f} + \Delta\vec{f}), \quad (127)$$

where $\Delta\vec{f}$ is a small, constant-offset spatial frequency. A single realization of the cross spectrum is given by

$$\begin{aligned} C(\vec{f}, \Delta\vec{f}) = & |O(\vec{f})| |O(\vec{f} + \Delta\vec{f})| |\mathcal{H}(\vec{f})| |\mathcal{H}(\vec{f} + \Delta\vec{f})| \\ & \times \exp\{i[\phi_o(\vec{f}) - \phi_o(\vec{f} + \Delta\vec{f}) + \phi_{\mathcal{H}}(\vec{f}) \\ & - \phi_{\mathcal{H}}(\vec{f} + \Delta\vec{f})]\}. \end{aligned} \quad (128)$$

Phase-difference information, that is, the difference in phase between points in the object phase spectrum, is encoded in the $\exp\{i[\phi_o(\vec{f}) - \phi_o(\vec{f} + \Delta\vec{f})]\}$ term in Eq. (128). However, in a single image realization this object phase-difference information is corrupted by random phase differences due to the atmosphere-telescope OTF contained in the $\exp\{i[\phi_{\mathcal{H}}(\vec{f}) - \phi_{\mathcal{H}}(\vec{f} + \Delta\vec{f})]\}$ term in Eq. (128).

Corruption of the object-spectrum phase-difference information by phase differences due to the OTF is overcome by averaging. Consider the average cross spectrum defined by

$$\begin{aligned} \langle C(\vec{f}, \Delta\vec{f}) \rangle = & |O(\vec{f})| |O(\vec{f} + \Delta\vec{f})| \\ & \times \exp\{i[\phi_o(\vec{f}) - \phi_o(\vec{f} + \Delta\vec{f})]\} \\ & \times \langle \mathcal{H}(\vec{f}) \mathcal{H}^*(\vec{f} + \Delta\vec{f}) \rangle. \end{aligned} \quad (129)$$

The specialized moment of the optical transfer function, $\langle \mathcal{H}(\vec{f}) \mathcal{H}^*(\vec{f} + \Delta\vec{f}) \rangle$, is referred to as the cross-spectrum transfer function. It is shown later that the cross-spectrum transfer function is real valued. Hence the phase of the average cross spectrum, $\phi_C(\vec{f}, \Delta\vec{f})$, is given by

$$\phi_C(\vec{f}, \Delta\vec{f}) = \phi_o(\vec{f}) - \phi_o(\vec{f} + \Delta\vec{f}), \quad (130)$$

which clearly encodes the object phase spectrum.

a. Unbiased estimator for the cross spectrum

When the cross spectrum is computed directly from photon-limited images, a bias arises similar to the photon-noise bias present in speckle interferometry (Ayers *et al.*, 1988). The unbiased estimator for the cross spectrum for photon-limited images, $C_U(\vec{f}, \Delta\vec{f})$, is (Ayers *et al.*, 1988; Beletic, 1989)

$$C_U(\vec{f}, \Delta\vec{f}) = D(\vec{f}) D^*(\vec{f} + \Delta\vec{f}) - D^*(\Delta\vec{f}). \quad (131)$$

No bias arises in the cross spectrum due to additive noise in the image measurement.

b. Cross-spectrum transfer function

The cross-spectrum transfer function can be written in terms of the telescope-pupil function $P(\vec{x})$ and the turbulence-induced phase aberration $\psi(\vec{x})$, as

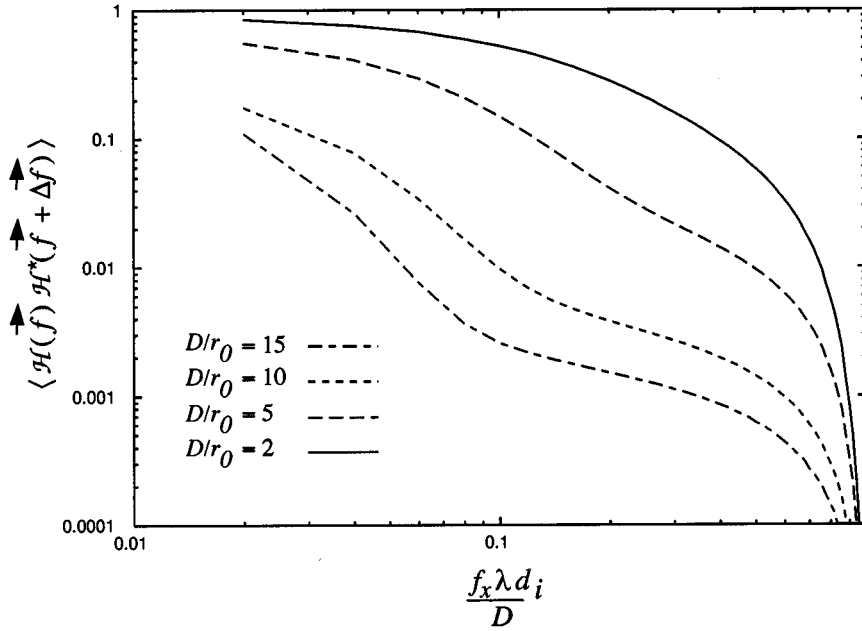


FIG. 38. Cross-spectrum transfer function for $D/r_0=2, 5, 10,$ and 15 . For the $D/r_0=15$ case the offset vector was set at $\Delta\vec{f}=0.033D/(\lambda d_i)$ in the f_x direction. For all other D/r_0 values the offset vector was set at $\Delta\vec{f}=0.05D/(\lambda d_i)$ in the f_x direction. The horizontal axis is normalized to the diffraction-limited cutoff frequency $D/(\lambda d_i)$.

$$\begin{aligned} \mathcal{H}(\vec{f})\mathcal{H}^*(\vec{f}+\Delta\vec{f}) &= N_F^{-2} \int d\vec{x} \int d\vec{x}' P(\vec{x})P(\vec{x}-\vec{f}\lambda d_i)P(\vec{x}')P(\vec{x}'-\vec{f}\lambda d_i-\Delta\vec{f}\lambda d_i) \\ &\quad \times \langle \exp\{i[\psi(\vec{x})-\psi(\vec{x}-\vec{f}\lambda d_i)-\psi(\vec{x}')+\psi(\vec{x}'-\vec{f}\lambda d_i-\Delta\vec{f}\lambda d_i)]\} \rangle. \end{aligned} \quad (132)$$

The expectation inside the integral in Eq. (132) can be simplified analytically. The result of this operation is

$$\begin{aligned} &\langle \exp\{i[\psi(\vec{x})-\psi(\vec{x}-\vec{f}\lambda d_i)-\psi(\vec{x}')+\psi(\vec{x}'-\vec{f}\lambda d_i-\Delta\vec{f}\lambda d_i)]\} \rangle \\ &= \exp\left\{-\frac{1}{2}[D_\psi(|\vec{f}\lambda d_i|)+D_\psi(|\vec{x}-\vec{x}'|)-D_\psi(|\vec{x}-\vec{x}'+\vec{f}\lambda d_i+\Delta\vec{f}\lambda d_i|)-D_\psi(|\vec{x}-\vec{x}'-\vec{f}\lambda d_i|) \right. \\ &\quad \left. +D_\psi(|\vec{x}-\vec{x}'+\Delta\vec{f}\lambda d_i|)+D_\psi(|\vec{f}\lambda d_i+\Delta\vec{f}\lambda d_i|)]\right\}. \end{aligned} \quad (133)$$

The cross-spectrum transfer function can be evaluated numerically. Note that it is necessary to pick a fixed value for the offset frequency $\Delta\vec{f}$ to obtain a two-dimensional expression for the cross-spectrum transfer function. A plot of such an evaluation is shown in Fig. 38. In Fig. 38 an f_x -axis slice of the cross-spectrum transfer function is shown for the cases of $D/r_0=2, 5, 10,$ and 15 . For the $D/r_0=15$ case the offset vector was set at $|\Delta\vec{f}|=0.033D/(\lambda d_i)$ in the f_x direction. For all other D/r_0 values the offset vector was set at $|\Delta\vec{f}|=0.05D/(\lambda d_i)$ in the f_x direction. The horizontal axis in Fig. 38 has been normalized to the diffraction-limited cutoff frequency $D/(\lambda d_i)$. Figure 38 shows that the mean cross spectrum contains high-spatial-frequency information.

Note that in all cases in Fig. 38 the offset spatial frequency $|\Delta\vec{f}|$ was chosen to be small compared to the frequency $r_0/(\lambda d_i)$. It is possible to show analytically that the cross-spectrum transfer function becomes small as $|\Delta\vec{f}|$ increases, though this exercise provides little insight into why this should be. Knox and Thompson (1974) analyzed the autocorrelation of the atmosphere-telescope OTF and found the width of this autocorrelation to be approximately $r_0/(\lambda d_i)$. For offset spatial frequencies less than $r_0/(\lambda d_i)$, the specialized moment of the optical transfer function, $\langle \mathcal{H}(\vec{f})\mathcal{H}^*(\vec{f}+\Delta\vec{f}) \rangle$, is non-zero, as illustrated in Fig. 38. However, if the offset frequency is greater than $r_0/(\lambda d_i)$, the OTF components at \vec{f} and $(\vec{f}+\Delta\vec{f})$ are approximately *uncorrelated*, so that

$$\begin{aligned} \langle \mathcal{H}(\vec{f}) \mathcal{H}^*(\vec{f} + \Delta\vec{f}) \rangle &\approx \langle \mathcal{H}(\vec{f}) \rangle \langle \mathcal{H}^*(\vec{f} + \Delta\vec{f}) \rangle \approx 0, \\ |\Delta\vec{f}| > r_0 / (\lambda d_i), \end{aligned} \quad (134)$$

since, at spatial frequencies $|\vec{f}| > r_0 / (\lambda d_i)$, the average OTF is approximately zero. A similar conclusion was obtained by Ayers *et al.* (1988), using a simulation of the cross-spectrum technique. Thus spatial-frequency offsets in the range $|\Delta\vec{f}| < r_0 / (\lambda d_i)$ are always used in the cross-spectrum method.

As a final comment, we note that the cross-spectrum transfer function is not shift indifferent (Ayers *et al.*, 1988; Roggemann and Welsh, 1996). That is, the cross spectrum is a function of the tilt component of the turbulence-induced aberration. Turbulence-induced random tilt causes the image to move randomly about the image plane but does not affect the image in any other way. Random image motion results in attenuation of the average cross spectrum. To avoid this attenuation the images in a data set are generally shifted to have a common center of mass before the cross spectrum is computed.

c. Phase-spectrum reconstruction from the cross spectrum

The fact that the cross-spectrum transfer function is nonzero at spatial frequencies approaching the diffraction-limited cutoff frequency is the enabling factor in the usefulness of the cross-spectrum technique. A suitable phase reconstruction algorithm is required to obtain the phase spectrum from the cross spectrum. To reconstruct a two-dimensional phase map, two offset vectors in orthogonal directions are required. The need for orthogonal offset vectors can be shown by the following analysis. Let one of the offset vectors be parallel to the f_x axis and denoted by Δf_x and let the other offset vector be parallel to the f_y axis and denoted by Δf_y . The phase differences generated by these offset vectors are

$$\begin{aligned} \Delta\phi_x(f_x, f_y) &= \phi_o(f_x, f_y) - \phi_o(f_x + \Delta f_x, f_y) \\ &\approx \frac{\partial\phi_o(\vec{f})}{\partial f_x} \Delta f_x, \\ \Delta\phi_y(f_x, f_y) &= \phi_o(f_x, f_y) - \phi_o(f_x, f_y + \Delta f_y) \\ &\approx \frac{\partial\phi_o(\vec{f})}{\partial f_y} \Delta f_y, \end{aligned} \quad (135)$$

where the notation $\Delta\phi_x(f_x, f_y)$ and $\Delta\phi_y(f_x, f_y)$ denotes phase differences in the f_x and f_y directions, respectively. The partial derivatives in Eq. (135) form the orthogonal components of the gradient of the object phase spectrum, $\nabla\phi_o(\vec{f})$. In practical applications of the cross-

spectrum method all of the operations leading to Eq. (135) are performed in a sampled space. As a consequence, f_x , f_y , Δf_x , and Δf_y may only take on a discrete set of values. It is assumed that the frequency domain is sampled on a uniform grid with scalar sample spacing given by Δf . Hence f_x , f_y , Δf_x , and Δf_y may only take on values given by integer multiples of Δf .

The phase differences given in Eq. (135) can be used to reconstruct recursively the phase of the object spectrum in the following way. One possible path to obtaining the phase at any point in the sampled frequency space is

$$\begin{aligned} \phi_o(N_x\Delta f_x, N_y\Delta f_y) &= - \sum_{i=0}^{N_x-1} \Delta\phi_x(i\Delta f_x, 0) \\ &\quad - \sum_{j=0}^{N_y-1} \Delta\phi_y(0, j\Delta f_y), \end{aligned} \quad (136)$$

where N_x and N_y are integers. Equation (136) says that the phase at any point that can be written as an integer multiple of $(\Delta f_x, \Delta f_y)$ can be obtained by summing the phase differences from $\vec{f} = (0, 0)$ to the point of interest. It should be noted that Eq. (136) indicates only one path to the point $\vec{f} = (N_x\Delta f_x, N_y\Delta f_y)$. However, a multiplicity of paths from $\vec{f} = (0, 0)$ to any point $(N_x\Delta f_x, N_y\Delta f_y)$ exist. In a noise-free system all of the possible paths to any point in frequency space would sum to the same phase value. However, noise effects can cause the sums of the phase differences along different paths to the same point to have different values. Averaging the sum of the phase differences along nonredundant paths to a given point in frequency space is often used to reduce the effects of noise (Knox, 1976).

2. Bispectrum technique

The bispectrum approach provides another technique for obtaining the phase spectrum of the object from short-exposure images. Like the cross spectrum, the bispectrum uses a specialized moment of the measured image spectrum. The bispectrum of an image is defined as (Lohmann *et al.*, 1983)

$$B(\vec{f}_1, \vec{f}_2) = I(\vec{f}_1) I(\vec{f}_2) I^*(\vec{f}_1 + \vec{f}_2). \quad (137)$$

The bispectrum is a four-dimensional data object since it is a function of four scalar spatial variables. The bispectrum has eightfold symmetry (Lohmann *et al.*, 1983).

The object phase spectrum is encoded in the phases of the bispectrum. The relationship between the bispectrum phase and the object phase spectrum is

$$\begin{aligned} B(\vec{f}_1, \vec{f}_2) &= |O(\vec{f}_1)| |O(\vec{f}_2)| |O(\vec{f}_1 + \vec{f}_2)| |\mathcal{H}(\vec{f}_1)| |\mathcal{H}(\vec{f}_2)| |\mathcal{H}(\vec{f}_1 + \vec{f}_2)| \exp\{i[\phi_o(\vec{f}_1) \\ &\quad + \phi_o(\vec{f}_2) - \phi_o(\vec{f}_1 + \vec{f}_2) + \phi_{\mathcal{H}}(\vec{f}_1) + \phi_{\mathcal{H}}(\vec{f}_2) - \phi_{\mathcal{H}}(\vec{f}_1 + \vec{f}_2)]\}. \end{aligned} \quad (138)$$

The object phase-spectrum information is encoded in the $\exp\{i[\phi_o(\vec{f}_1) + \phi_o(\vec{f}_2) - \phi_o(\vec{f}_1 + \vec{f}_2)]\}$ term of Eq. (138). In a single realization of the bispectrum, the object phase-spectrum information is corrupted by the random phase spectrum of the optical transfer function, present in the $\exp\{i[\phi_H(\vec{f}_1) + \phi_H(\vec{f}_2) - \phi_H(\vec{f}_1 + \vec{f}_2)]\}$ term of Eq. (138). This corruption is overcome by averaging. The expected value of the bispectrum is given by

$$\langle B(\vec{f}_1, \vec{f}_2) \rangle = O(\vec{f}_1) O(\vec{f}_2) O(\vec{f}_1 + \vec{f}_2) \times \langle \mathcal{H}(\vec{f}_1) \mathcal{H}(\vec{f}_2) \mathcal{H}^*(\vec{f}_1 + \vec{f}_2) \rangle. \quad (139)$$

The term $\langle \mathcal{H}(\vec{f}_1) \mathcal{H}(\vec{f}_2) \mathcal{H}^*(\vec{f}_1 + \vec{f}_2) \rangle$ relates the object-spectrum information to the bispectrum and is referred to as the bispectrum transfer function. An argument similar to that leading to Eq. (133) can be used to show that the bispectrum transfer function is real (Lohmann *et al.*, 1983). The key result of these analyses is that the average bispectrum is found to be nonzero out to spatial frequencies approaching the diffraction-limited cutoff frequency, if the range of allowed values of $(\vec{f}_1 + \vec{f}_2)$ is suitably constrained.

Unlike the cross spectrum, the bispectrum is insensitive to random motion of the image centroid. The practical consequence of this insensitivity to turbulence-induced random motion of the image is that, unlike the cross-spectrum case, images do not have to be shifted to a common centroid prior to computing the bispectrum. At low light levels and for extended objects, significant errors can be present in the estimate of the location of the centroid (Yura and Tavis, 1985), leading to an attenuation of the average cross spectrum, which is not present in the average bispectrum.

It is necessary to constrain the range of allowed values of $(\vec{f}_1 + \vec{f}_2)$. This is generally accomplished by letting \vec{f}_1 sweep through the entire range of frequency space of interest and letting \vec{f}_2 be a small offset vector that we shall denote as $\Delta\vec{f}$. Simulation studies (Matson, 1991; Beletic and Goody, 1992) and theoretical investigations (Ayers *et al.*, 1988) have shown that little useful information is obtained from the bispectrum if $|\Delta\vec{f}| > r_0/\lambda d_i$. A heuristic argument can be used to understand the reason for this limitation. Consider the bispectrum transfer function $\langle \mathcal{H}(\vec{f}_1) \mathcal{H}(\vec{f}_2) \mathcal{H}^*(\vec{f}_1 + \vec{f}_2) \rangle$ for the case of $|\vec{f}_1| \gg r_0/\lambda d_i$, $\vec{f}_2 = \Delta\vec{f}$, and $|\Delta\vec{f}| < r_0/\lambda d_i$. In this case the optical transfer function at $\Delta\vec{f}$ is finite and, based on the earlier discussion of the cross-spectrum transfer function, approximately uncorrelated with the OTF at \vec{f}_1 and $\vec{f}_1 + \Delta\vec{f}$, so that

$$\langle \mathcal{H}(\vec{f}_1) \mathcal{H}(\Delta\vec{f}) \mathcal{H}^*(\vec{f}_1 + \Delta\vec{f}) \rangle \approx \langle \mathcal{H}(\Delta\vec{f}) \rangle \langle \mathcal{H}(\vec{f}_1) \mathcal{H}^*(\vec{f}_1 + \Delta\vec{f}) \rangle. \quad (140)$$

The second term on the right side of Eq. (140), $\langle \mathcal{H}(\vec{f}_1) \mathcal{H}^*(\vec{f}_1 + \Delta\vec{f}) \rangle$, is recognized as the cross-spectrum transfer function presented in Eq. (132). As shown in the discussion of Eq. (132), the $\langle \mathcal{H}(\vec{f}_1) \mathcal{H}^*(\vec{f}_1 + \Delta\vec{f}) \rangle$

term has significant value only for $|\Delta\vec{f}| < r_0/\lambda d_i$. Thus the bispectrum has significant value for bispectrum elements in the range $|\Delta\vec{f}| < r_0/\lambda d_i$.

a. Unbiased estimator for the bispectrum

When the bispectrum is computed directly from photon-limited images, a photon-noise bias arises similar to the photon-noise bias present in speckle interferometry and the cross spectrum. The unbiased estimator for the bispectrum $B_U(\vec{f}_1, \vec{f}_2)$ is given by (Lawrence *et al.*, 1992)

$$B_U(\vec{f}_1, \vec{f}_2) = D(\vec{f}_1) D(\vec{f}_2) D^*(\vec{f}_1 + \vec{f}_2) - |D(\vec{f}_1)|^2 - |D(\vec{f}_2)|^2 - |D(\vec{f}_1 + \vec{f}_2)|^2 + 2K. \quad (141)$$

If additive noise is present in the image measurement then an additional term is needed in the unbiased estimator for the bispectrum to remove the bias that arises from the additive noise. In the presence of additive noise the unbiased estimator for the bispectrum is

$$B_U(\vec{f}_1, \vec{f}_2) = D(\vec{f}_1) D(\vec{f}_2) D^*(\vec{f}_1 + \vec{f}_2) - |D(\vec{f}_1)|^2 - |D(\vec{f}_2)|^2 - |D(\vec{f}_1 + \vec{f}_2)|^2 + 2K + 3P\sigma_n^2. \quad (142)$$

b. Phase-spectrum reconstruction from the bispectrum

The most widely used technique for reconstructing the object phase spectrum from the phase of the bispectrum is recursive in nature and is similar to the cross-spectrum reconstruction technique presented in Sec. IV.C.1. The recursive reconstruction process uses the fact that the object phase spectrum at $(\vec{f}_1 + \vec{f}_2)$ can be expressed as

$$\phi_o(\vec{f}_1 + \vec{f}_2) = \phi_o(\vec{f}_1) + \phi_o(\vec{f}_2) - \phi_B(\vec{f}_1, \vec{f}_2), \quad (143)$$

where $\phi_B(\vec{f}_1, \vec{f}_2)$ is the phase of the mean bispectrum. Thus, if the object spectrum at \vec{f}_1 and \vec{f}_2 is known, the object phase spectrum at $(\vec{f}_1 + \vec{f}_2)$ can be computed directly. Of course, two starting points are required for this process—the object phase spectrum at some initial values of \vec{f}_1 and \vec{f}_2 must be determined. The object phase spectrum at $\vec{f} = 0$ is identically zero so that $\phi_o(\vec{f} = 0) = 0$. While this is a sufficient starting point for object phase-spectrum reconstruction from the cross spectrum, an additional known phase is required for phase reconstruction from the bispectrum. The additional starting point typically used is to choose

$$\begin{aligned} \phi_o(\pm \Delta f, 0) &= 0, \\ \phi_o(0, \pm \Delta f) &= 0, \end{aligned} \quad (144)$$

where Δf is the sample spacing in the frequency domain. In words, Eq. (144) says that the phase of the four points closest to $\vec{f} = (0, 0)$ are set equal to zero. It is easy to show that any nonzero choice of $\phi_o(\pm \Delta f, 0)$ or $\phi_o(0, \pm \Delta f)$ causes a term linear in Δf to appear in the reconstructed phase. This linear phase term corresponds

to a shift of the image in space. Since we are typically indifferent to the absolute location of the object within the image, no information of value is lost by making the choice in Eq. (144).

Within the bispectrum there are many possible combinations of \vec{f}_1 and \vec{f}_2 that sum to $(\vec{f}_1 + \vec{f}_2)$. Under noise-free conditions the reconstructed phase at $(\vec{f}_1 + \vec{f}_2)$ would be the same for all paths. However, noise effects corrupt the phase estimation process so that the reconstructed phase at $(\vec{f}_1 + \vec{f}_2)$ is a function of the path taken. To reduce these noise effects the phase estimates from several unique paths to $(\vec{f}_1 + \vec{f}_2)$ are generally averaged (Lawrence *et al.*, 1992).

It should be noted that the bispectrum phases are only known modulo 2π . Hence the recursive reconstructor in Eq. (143) could, and in practice often does, lead to 2π phase mismatches between the phase-spectrum values computed along different paths to the same point in frequency space. Phases from different paths to the same point cannot be averaged to reduce noise under this condition (Northcott *et al.*, 1988). To overcome this problem, a variation of Eq. (143) is often used. In this variation the recursive phase reconstruction is performed using unit-amplitude phasors. Mathematically, the unit-amplitude-phasor recursive reconstructor is given by (Meng *et al.*, 1990)

$$\exp\{i\phi_o(\vec{f}_1 + \vec{f}_2)\} = \exp\{i\phi_o(\vec{f}_1)\} \exp\{i\phi_o(\vec{f}_2)\} \times \exp\{-i\phi_B(\vec{f}_1, \vec{f}_2)\}. \quad (145)$$

The object phase spectrum is obtained by computing the argument of the left-hand side of Eq. (145). Phase-spectrum values obtained using Eq. (145) are indifferent to the 2π phase ambiguities. Hence phase-spectrum values obtained from multiple paths to the same point may be averaged to reduce noise effects. The unit-amplitude-phasor recursive reconstructor has been used successfully in several studies of the bispectrum technique (Ayers *et al.*, 1988; Northcott *et al.*, 1988; Meng *et al.*, 1990; Matson, 1991; Lawrence *et al.*, 1992).

While the present treatment of phase reconstruction from the bispectrum has been limited to recursive phase reconstruction, it should be noted that this problem has received a great deal of attention in the literature. Meng *et al.* (1990) have developed a least-squares formulation of the phase reconstruction problem. Northcott *et al.* (1988) have developed a reconstruction technique based on the projection-slice theorem of tomography and the Radon transform. Matson (1991) and Matson *et al.* (1992) have developed two weighted-least-squares estimation formulations of the phase reconstruction problem. Ayers *et al.* (1988) and Nakajima (1988) have performed extensive studies of the signal-to-noise-ratio behavior of the bispectrum, and Matson *et al.* (1992) have studied phase-spectrum reconstruction errors when using noisy bispectra. These analyses have consistently shown that the bispectrum phase-spectrum reconstruction technique can be used to obtain high-quality phase-spectrum estimates for point-source objects in the mid-

frequency regime of 40–60 % of the diffraction-limited cutoff frequency of the telescope at low light levels. This performance improves as the light level increases (Betic and Goody, 1992).

D. Image reconstruction for speckle imaging

In this section the problem of reconstructing an image from speckle-imaging measurements and computations is discussed. Representative results of speckle imaging are provided to demonstrate the level of imaging performance that can be expected for speckle imaging. All of the results presented were obtained using a simulation of speckle imaging.

The modulus squared of the object spectrum may be obtained using a variation of the Wiener filter (Gonzalez and Woods, 1993), given by

$$|\tilde{O}_n(\vec{f})|^2 = \frac{Q(\vec{f})}{Q_R(\vec{f}) + \alpha/\text{SNR}_Q(\vec{f})}, \quad (146)$$

where $\text{SNR}_Q(\vec{f})$ is the signal-to-noise ratio of $Q(\vec{f})$ computed from sample-based estimates of the mean and standard deviation of $Q(\vec{f})$ and α is a constant selected by the user. The purpose of the term $\alpha/\text{SNR}_Q(\vec{f})$ in Eq. (146) is to reduce the effects of noise at high spatial frequencies similar to the Wiener filter (Gonzalez and Woods, 1993; Roggemann, Caudill *et al.*, 1994).

Next, the square root of $|\tilde{O}_n(\vec{f})|^2$ is computed, and the phase spectrum reconstructed from the bispectrum phase is associated with $|\tilde{O}_n(\vec{f})|$ to obtain $\tilde{O}_n(\vec{f})$. After the average unbiased bispectrum was obtained, the phase spectrum was reconstructed using the recursive technique (Northcott *et al.*, 1988) for all examples shown here. An image can be obtained by applying the inverse-Fourier-transform operation to $\tilde{O}_n(\vec{f})$.

Some examples are now presented to illustrate the level of performance that can be provided by speckle imaging. A one-meter-diameter telescope was simulated for these examples. A binary star was modeled with separation of $1.5 \mu\text{rad}$, with one star twice as bright as the other. The Fried seeing parameter was set at two different levels, $r_0 = 0.1 \text{ m}$ and $r_0 = 0.05 \text{ m}$, at the wavelength of 500 nm to obtain $D/r_0 = 10$ and $D/r_0 = 20$, respectively. Note that the atmospheric-seeing angular-resolution limit λ/r_0 is given by $10 \mu\text{rad}$ for the $r_0 = 0.05 \text{ m}$ case and $5 \mu\text{rad}$ for the $r_0 = 0.1 \text{ m}$ case, while the diffraction-limited angular resolution $\lambda/D = 0.5 \mu\text{rad}$. Hence this binary star could not be resolved using conventional long-exposure imaging, but could be resolved with diffraction-limited telescope performance. The average number of photoevents per image was set at three different levels using the visual magnitudes $m_v = 4, 8, \text{ and } 12$. Exposure time for the image measurements was fixed at 10 ms , and the mean wavelength was chosen to be 500 nm with a bandwidth of 50 nm , centered on the mean wavelength. These choices yield the following average numbers of photoevents per image: for $m_v = 4$, $\bar{K} = 45\,177$; for $m_v = 8$, $\bar{K} = 1\,135$; and for

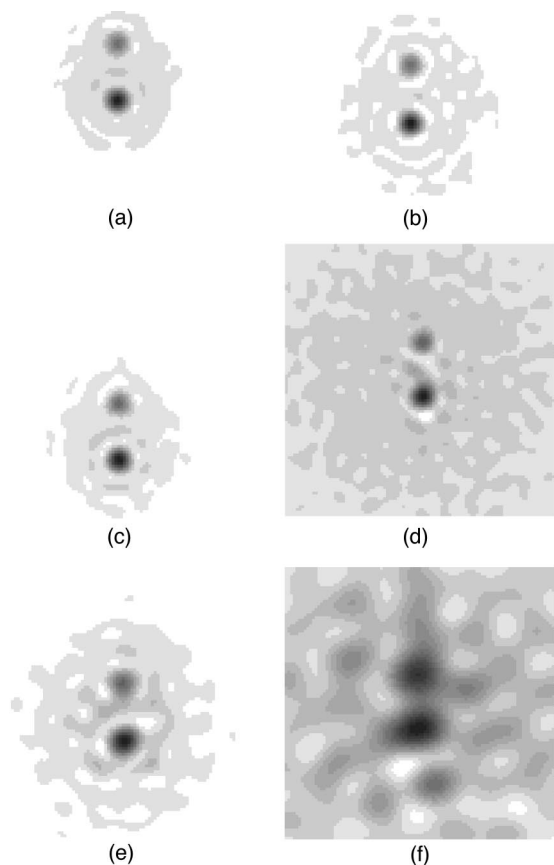


FIG. 39. Reconstructed binary-star images: (a) $D/r_0=10$, $m_v=4$; (b) $D/r_0=20$, $m_v=4$; (c) $D/r_0=10$, $m_v=8$; (d) $D/r_0=20$, $m_v=8$; (e) $D/r_0=10$, $m_v=12$; (f) $D/r_0=20$, $m_v=12$. Angular separation of the binary components is $1.5 \mu\text{rad}$, the telescope diameter is 1.0 m , and the ratio of brightnesses is $2:1$. The central 100×100 pixels of 256×256 pixel images are presented. Negative images are displayed for clarity.

$m_v=12$, $\bar{K}=180$. Two hundred frames were used to obtain all of the results shown. The reconstructed images for the binary star are shown in Fig. 39. The images in the left column are for $D/r_0=10$, and the images in the right column are for $D/r_0=20$. Reconstructed images for $m_v=4$ are in the top row, reconstructed images for $m_v=8$ are in the middle row, and reconstructed images for $m_v=12$ are in the bottom row. Note that for the higher signal levels and better seeing conditions the binary star is easily resolved. However, as r_0 decreases and m_v increases, two effects become apparent: (1) the resolution, as indicated by the width of one of the star images, becomes degraded, and (2) the images become noisier, as indicated by the energy in the “halo” surrounding the reconstructed stars.

E. Conclusion

This section has provided a discussion of pure post-detection image-processing techniques for overcoming the effects of atmospheric turbulence on astronomical imaging systems. While we have attempted to cover all of the relevant topics, it is impossible to give a fully comprehensive review of all of the relevant literature here. Detailed presentations on specific related topics are available in the literature, including the signal-to-noise ratio of $Q(\vec{f})$ (Miller, 1977; Dainty and Greenaway, 1979; Goodman, 1985; Roggemann and Matson, 1992), phase-spectrum reconstruction from the cross spectrum (Knox and Thompson, 1974; Knox, 1976; Ayers *et al.*, 1988), phase-spectrum reconstruction from the bispectrum (Lohmann *et al.*, 1983; Ayers *et al.*, 1988; Matson, 1991), a treatment of photon-noise effects on the bispectrum (Ayers *et al.*, 1988; Nakajima, 1988), and the effects of photon noise on the quality of the phase spectrum reconstructed from the bispectrum (Ayers *et al.*, 1988; Matson, 1991; Matson *et al.*, 1992; Roggemann and Matson, 1992). In addition, an interesting comparison of the cross spectrum and bispectrum techniques is provided by Ayers *et al.* (1988).

Recently, two alternatives to the conventional speckle-imaging techniques presented here have been explored in the literature: (1) blind deconvolution; (Ayers and Dainty, 1988; Davey, Lane, and Bates, 1989; Lane 1992; Jefferies and Christou, 1993); and (2) phase-diverse speckle imaging (Paxman *et al.*, 1992). Blind deconvolution involves jointly processing ensembles of speckled images to estimate the object using a constrained iterative approach. Useful constraints have been shown to be positivity (i.e., pixel values cannot be negative) and object support (i.e., nonzero pixels are not allowed outside some region in the image where the object is known to lie). Recently, a new approach to blind deconvolution of speckled images has been developed that is based on maximum-likelihood estimation of the object using an algorithm that automatically enforces positivity in the images (Schulz, 1993). Phase-diverse speckle imaging is based on the phase-diversity concept initially proposed by Gonsalves (1982), which requires joint processing of a speckled image and a simultaneously recorded image that is slightly out of focus. It is not known at this time how the images reconstructed by either of these algorithms are affected by shot noise and noise in the imagery arising from turbulence-induced randomness.

V. DECONVOLUTION FROM WAVE-FRONT SENSING

Deconvolution from wave-front sensing (DWFS) is a hybrid imaging technique that uses simultaneous measurements of a short-exposure image and a wave-front sensor. A block diagram of the DWFS method is shown in Fig. 40. Light entering the telescope is divided using a beam splitter between a wave-front sensor and an imag-

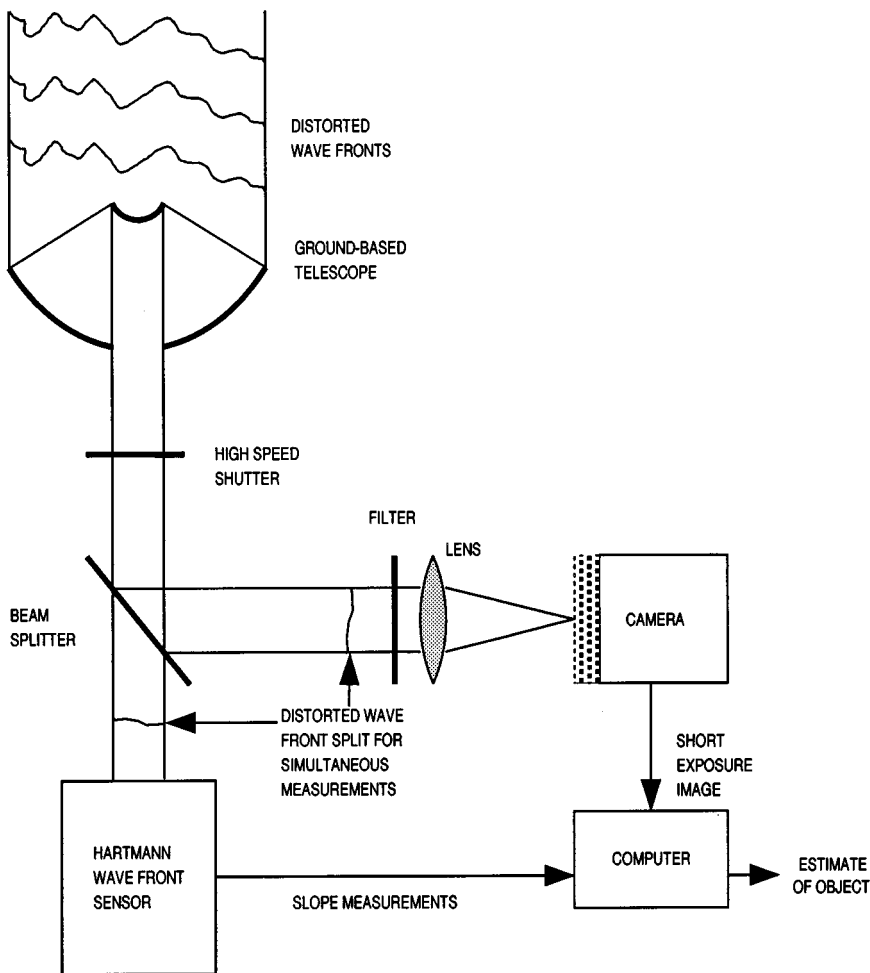


FIG. 40. Block diagram of the deconvolution from wave-front sensing (DWFS) method.

ing camera. An image of the pupil field is presented at the input to the wave-front sensor, which makes a measurement of the turbulence-induced phase aberration $\psi(\vec{x})$. Image and wave-front sensor measurements are made simultaneously and are recorded for later processing. Wave-front sensor measurements are processed in the computer to reconstruct an estimate of $\psi(\vec{x})$, denoted $\tilde{\psi}(\vec{x})$, which is combined with a pupil model to form an estimate of the generalized pupil function given by $W(\vec{x})\exp\{i\tilde{\psi}(\vec{x})\}$, where $W(\vec{x})$ is the pupil function. The estimate of the generalized pupil function is processed to compute an estimate of the optical transfer function, denoted $\tilde{H}(\vec{f})$, and this estimate of the OTF is used in a spatial-frequency-domain deconvolution procedure described below. Averaging of many realizations of the estimator is used to improve the signal-to-noise ratio of the spectral data.

The basic concept for DWFS was first proposed by Fontanella (1985). This concept was later extended by Fried (1987), who used a different estimator from that proposed by Fontanella, and independently by Primot *et al.* (1990), who provided the first laboratory experimental results. Gonglewski *et al.* (1990) provided the first experimental validation of DWFS on real astro-

nomical images. Welsh and Von Niederhausern (1993) provided an analysis of the DWFS method using an optimal estimator for the wave-front phase. Roggemann, Welsh *et al.* (1994) showed that the Primot estimator is biased and proposed an alternative measurement and processing technique that is immune to the effects of this bias. They also devised an expression for the signal-to-noise ratio of DWFS. Their unbiased DWFS technique is analyzed here. It has also been shown that the DWFS estimator proposed by Fried is appropriate for use in conjunction with adaptive-optics compensation (Roggemann and Meinhardt, 1993; Roggemann *et al.*, 1995).

The remainder of this section is organized as follows. In the next subsection we present the estimators used for deconvolution from wave-front sensing. This discussion is followed by a presentation of the wave-front phase reconstructor used for DWFS. Representative results for the DWFS transfer function are provided. Signal-to-noise-ratio considerations are presented in the subsection that follows, and the DWFS signal-to-noise ratio is compared to the signal-to-noise ratio of the speckle-interferometry estimator $Q(\vec{f})$. Examples of DWFS imaging performance are provided in the final subsection.

A. DWFS estimators

In this subsection we examine the estimators used to reconstruct images in the DWFS method. The estimator for the optical transfer function is based on the expression for the OTF given in Eq. (36) and is given by

$$\begin{aligned} \tilde{\mathcal{H}}(\vec{f}) = & N_F^{-1} \int d\vec{x} W(\vec{x}) W(\vec{x} - \vec{f}\lambda d_i) \\ & \times \exp\{i[\tilde{\psi}(\vec{x}) - \tilde{\psi}(\vec{x} - \vec{f}\lambda d_i)]\}. \end{aligned} \quad (147)$$

A single realization of the object-spectrum estimate $\tilde{O}(\vec{f})$ proposed by Primot *et al.* (1990) is given by

$$\tilde{O}(\vec{f}) = \frac{D(\vec{f})\tilde{\mathcal{H}}^*(\vec{f})}{|\tilde{\mathcal{H}}(\vec{f})|^2}. \quad (148)$$

$\tilde{O}(\vec{f})$ is random due to turbulence and measurement-noise effects. Hence averaging is used to boost the signal-to-noise ratio of $\tilde{O}(\vec{f})$. The averaging technique proposed by Primot *et al.* is given by

$$\langle \tilde{O}(\vec{f}) \rangle = \frac{\langle I(\vec{f})\tilde{\mathcal{H}}^*(\vec{f}) \rangle}{\langle |\tilde{\mathcal{H}}(\vec{f})|^2 \rangle} = \frac{O(\vec{f})\langle \mathcal{H}(\vec{f})\tilde{\mathcal{H}}^*(\vec{f}) \rangle}{\langle |\tilde{\mathcal{H}}(\vec{f})|^2 \rangle}, \quad (149)$$

where $\langle D(\vec{f}) \rangle = O(\vec{f})\langle \mathcal{H}(\vec{f}) \rangle$. An estimate of the object irradiance distribution $o(\vec{x})$ is obtained by applying the inverse Fourier transform to $\langle \tilde{O}(\vec{f}) \rangle$. The form of Eq. (149) leads to the definition of the average DWFS transfer function $\langle S(\vec{f}) \rangle$ as

$$\langle S(\vec{f}) \rangle = \frac{\langle \mathcal{H}(\vec{f})\tilde{\mathcal{H}}^*(\vec{f}) \rangle}{\langle |\tilde{\mathcal{H}}(\vec{f})|^2 \rangle}. \quad (150)$$

One motivation for the form of the numerator of Eq. (149) can be seen by comparing the numerator of Eq. (150) to the speckle transfer function $\langle |\mathcal{H}(\vec{f})|^2 \rangle$. In the limit of perfect wave-front estimation, the result

$$\langle \mathcal{H}(\vec{f})\tilde{\mathcal{H}}^*(\vec{f}) \rangle \rightarrow \langle |\mathcal{H}(\vec{f})|^2 \rangle \quad (151)$$

is obtained. The right-hand side of Eq. (151) is exactly the speckle transfer function, which was previously shown to be nonzero out to spatial frequencies approaching the diffraction-limited cutoff frequency. Thus, if excellent wave-front reconstruction is obtained, the numerator of Eq. (149) will contain nearly diffraction-limited object-spectrum information.

Another motivation for the estimator of Eq. (149) is that deconvolution from wave-front sensing provides both the *magnitude* and the *phase* of the object spectrum directly. No intermediate Fourier phase-spectrum reconstruction step, such as computing and processing the cross spectrum or bispectrum, as is required in speckle imaging, is needed in DWFS. Hence DWFS provides a computational advantage over speckle imaging, but at the expense of making wave-front sensor measurements and post-processing wave-front sensor data.

Note that the mid and high spatial frequencies of $O(\vec{f})$ are highly attenuated by multiplication with $\langle \mathcal{H}(\vec{f})\tilde{\mathcal{H}}^*(\vec{f}) \rangle$, and hence an image formed by applying

the inverse Fourier transformation to the numerator of Eq. (149) would be badly blurred. The intended purpose of the denominator of Eq. (149) is to boost the attenuated spatial-frequency components of $O(\vec{f})\langle \mathcal{H}(\vec{f})\tilde{\mathcal{H}}^*(\vec{f}) \rangle$ to their proper values. This goal is accomplished if $\langle \mathcal{H}(\vec{f})\tilde{\mathcal{H}}^*(\vec{f}) \rangle$ and $\langle |\tilde{\mathcal{H}}^*(\vec{f})|^2 \rangle$ have the same value. Unfortunately, detailed analysis has shown that in general

$$\langle |\tilde{\mathcal{H}}^*(\vec{f})|^2 \rangle \neq \langle \mathcal{H}(\vec{f})\tilde{\mathcal{H}}^*(\vec{f}) \rangle, \quad (152)$$

so that the DWFS transfer function given in Eq. (150) does not provide object-spectrum estimates $\tilde{O}(\vec{f})$ with the proper amplitudes (Roggemann, Welsh *et al.*, 1994). The reason for the inequality in Eq. (152) is that the atmospheric phase $\psi(\vec{x})$ and the estimated phase $\tilde{\psi}(\vec{x})$ have different correlation properties, as shown by Roggemann, Welsh *et al.* (1994). Equation (152) implies that undesired results will be obtained when the object-spectrum estimate of Eq. (149) is used. For example, it is possible for $|\langle S(\vec{f}) \rangle| > 1$, which results in undesired *amplification* of some spatial-frequency components (Roggemann, Welsh *et al.*, 1994).

Roggemann, Welsh *et al.* (1994) proposed a remedy to this problem, which is analogous to the reference-source calibration used in speckle interferometry. Rather than use the estimated OTF $\tilde{\mathcal{H}}(\vec{f})$ in the denominator of Eq. (149), one uses measurements obtained from a reference star. Note that the spectrum of the reference-star image, normalized to have the value of unity at $\vec{f}=0$, gives the OTF of the atmosphere-telescope system at any instant, which we denote by $\mathcal{H}^{\text{ref}}(\vec{f})$. A wave-front sensor measurement made simultaneously with the star-image measurement can be used to obtain an estimate of the OTF, denoted by $\tilde{\mathcal{H}}^{\text{ref}}(\vec{f})$. Finally, a new definition of the denominator of Eq. (149), which has the same mean as the numerator of Eq. (149) if atmospheric and light-level conditions are constant, is given by $\langle \mathcal{H}^{\text{ref}}(\vec{f})\tilde{\mathcal{H}}^{\text{ref}}(\vec{f})^* \rangle$. The final form of the DWFS estimator is thus given by

$$\langle \tilde{O}(\vec{f}) \rangle = \frac{\langle D(\vec{f})\tilde{\mathcal{H}}^*(\vec{f}) \rangle}{\langle \mathcal{H}^{\text{ref}}(\vec{f})\tilde{\mathcal{H}}^{\text{ref}}(\vec{f})^* \rangle}. \quad (153)$$

Wave-front sensing and reconstruction for DWFS is based on the principles of wave-front sensing and deformable-mirror control discussed in Sec. III.B. However, in the case of DWFS, considerably more freedom exists for the choice of elementary functions to use in obtaining the phase estimate $\tilde{\psi}(\vec{x})$. Examples of elementary functions that have been used include Zernike polynomials (Gonglewski *et al.*, 1990; Primot *et al.*, 1990; Roggemann and Welsh, 1994; Roggemann, Welsh *et al.*, 1994), two-dimensional Gaussian functions (Welsh and Niederhausern, 1993), and two-dimensional triangle functions (Roggemann *et al.*, 1995).

B. Evaluation of the DWFS transfer function

In this subsection the numerator of the DWFS transfer function $\langle \mathcal{H}(\vec{f})\tilde{\mathcal{H}}^*(\vec{f}) \rangle$ is evaluated. Representative

TABLE II. Input parameters for DWFS transfer-function results.

Parameter	Value
Pupil diameter D	1 m
Subaperture side length d	0.1 m
λ_w	500 nm
λ_l	600 nm
No. of Zernike polynomials	61
r_0	0.5 m, 0.1 m at $\lambda=500$ nm
SNR_w	$\infty, 5, 3, 2$

results are obtained using a simulation described by Roggemann and Welsh (1996). The speckle transfer function $\langle |\mathcal{H}(\vec{f})|^2 \rangle$ for the appropriate seeing condition is also presented for purposes of comparison. The parameters of the system simulated are given in Table II.

Simulation results are presented in Fig. 41 for a variety of wave-front sensor signal-to-noise ratios SNR_w . For a shot-noise-limited detector in a Hartmann sensor $\text{SNR}_w = \bar{K}$ in Eq. (75). Both $\langle \mathcal{H}(\vec{f}) \tilde{\mathcal{H}}^*(\vec{f}) \rangle$ and $\langle |\mathcal{H}(\vec{f})|^2 \rangle$ are plotted in Fig. 41. The variable f_x in Fig. 41 is one of the orthogonal components of the spatial frequency variable \vec{f} , so that with normalization the condition $0 \leq f_x \lambda d_i / D \leq 1$ is obtained. In Fig. 41(a) $\langle \mathcal{H}(\vec{f}) \tilde{\mathcal{H}}^*(\vec{f}) \rangle$ and $\langle |\mathcal{H}(\vec{f})|^2 \rangle$ are shown for $r_0 = 50$ cm at $\lambda = 500$ nm, and $\text{SNR}_w = \infty, 5, 3,$ and 2 . Figure 41(b) shows a similar family of curves for $r_0 = 10$ cm at $\lambda = 500$ nm.

Inspection of Figs. 41(a) and 41(b) provides insight into the limits of performance of DWFS and provides a qualitative comparison of DWFS and speckle imaging. For $r_0 = 50$ cm, which gives $D/r_0 = 2$, and high SNR_w , $\langle \mathcal{H}(\vec{f}) \tilde{\mathcal{H}}^*(\vec{f}) \rangle$ is reasonably close to the speckle transfer function $\langle |\mathcal{H}(\vec{f})|^2 \rangle$. The condition $\langle \{ \mathcal{H}(\vec{f}) \tilde{\mathcal{H}}^*(\vec{f}) \} \rangle \leq E \langle |\mathcal{H}(\vec{f})|^2 \rangle$ exists, since the phase of the optical transfer function is imperfectly estimated in deconvolution from wave-front sensing. As expected, $\langle \mathcal{H}(\vec{f}) \tilde{\mathcal{H}}^*(\vec{f}) \rangle$ decreases with decreasing SNR_w . It must be noted that the $D/r_0 = 2$ case represents extremely good seeing, which would rarely, if ever, be encountered in practice at visible wavelengths on a one-meter-diameter telescope.

The more realistic seeing case of $D/r_0 = 10$ shown in Fig. 41(b) illustrates some of the limits of the DWFS method. Observe that, for $D/r_0 = 10$ at all values of SNR_w , $\langle \mathcal{H}(\vec{f}) \tilde{\mathcal{H}}^*(\vec{f}) \rangle$ is significantly less than $\langle |\mathcal{H}(\vec{f})|^2 \rangle$ for $f_x \lambda d_i / D \geq 0.15$ and is less than 10^{-4} for $f_x \lambda d_i / D \geq 0.55$. By comparison, $\langle |\mathcal{H}(\vec{f})|^2 \rangle$ does not fall below 10^{-4} until $f_x \lambda d_i / D \geq 0.93$. Hence speckle interferometry will on average provide measurements with higher spatial-frequency content, though it must be noted that the speckle-interferometry measurements will not contain any object phase-spectrum information.

While the speckle transfer function $\langle |\mathcal{H}(\vec{f})|^2 \rangle$ has been shown to be greater than $\langle \mathcal{H}(\vec{f}) \tilde{\mathcal{H}}^*(\vec{f}) \rangle$, we cannot

conclude that speckle imaging is in every case superior to DWFS. Such a conclusion must be based on signal-to-noise-ratio considerations, which include the effects of the object spectrum, measurement noise, and randomness in the appropriate transfer function, $|\mathcal{H}(\vec{f})|^2$ in the case of speckle imaging and $\mathcal{H}(\vec{f}) \tilde{\mathcal{H}}^*(\vec{f})$ in the case of DWFS. In the next subsection the DWFS signal-to-noise ratio is derived and compared to the signal-to-noise ratio of the unbiased speckle-interferometry estimator $Q(\vec{f})$.

C. Signal-to-noise-ratio considerations

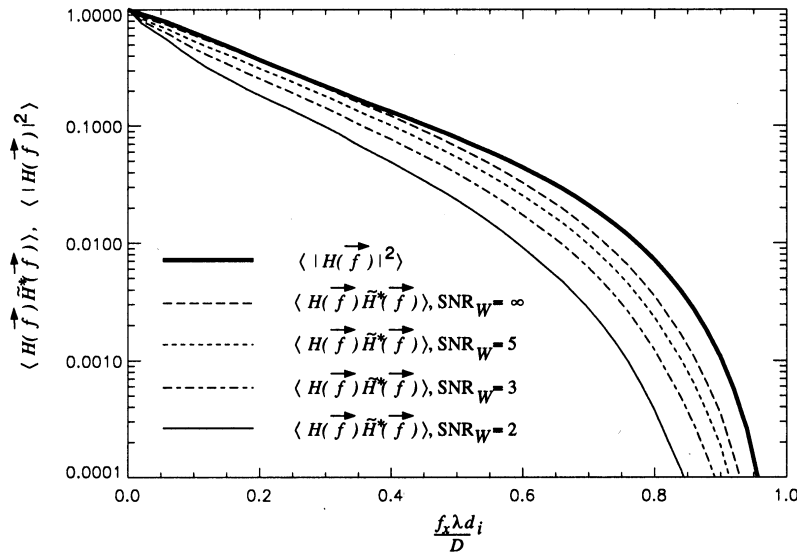
In this subsection the spatial-frequency-domain signal-to-noise ratio of the DWFS method is derived for the case of photon-limited detection. The signal-to-noise-ratio analysis must account for all sources of randomness in the DWFS process. In the DWFS case the sources of randomness include photon noise in the detected image, randomness in the OTF, and randomness in the estimated OTF. We shall see that the DWFS signal-to-noise-ratio expression is similar to the image-spectrum signal-to-noise ratio obtained in Eq. (69) for the photon-limited detection case. However, the DWFS signal-to-noise ratio will be expressed in terms of the mean and variance of $\mathcal{H}(\vec{f}) \tilde{\mathcal{H}}^*(\vec{f})$ and the second moment of $\tilde{\mathcal{H}}(\vec{f})$, rather than just the mean and variance of $\mathcal{H}(\vec{f})$. The signal-to-noise ratio for DWFS is then compared to the signal-to-noise ratio for the unbiased speckle-imaging estimator $Q(\vec{f})$. The relevant signal-to-noise ratio for DWFS, $\text{SNR}_{DW}(\vec{f})$, is the signal-to-noise ratio of the numerator of the object-spectrum estimate $\tilde{O}(\vec{f})$ given by

$$\text{SNR}_{DW}(\vec{f}) = \frac{|\langle D(\vec{f}) \tilde{\mathcal{H}}^*(\vec{f}) \rangle|}{\sqrt{\text{var}\{D(\vec{f}) \tilde{\mathcal{H}}^*(\vec{f})\}}}, \quad (154)$$

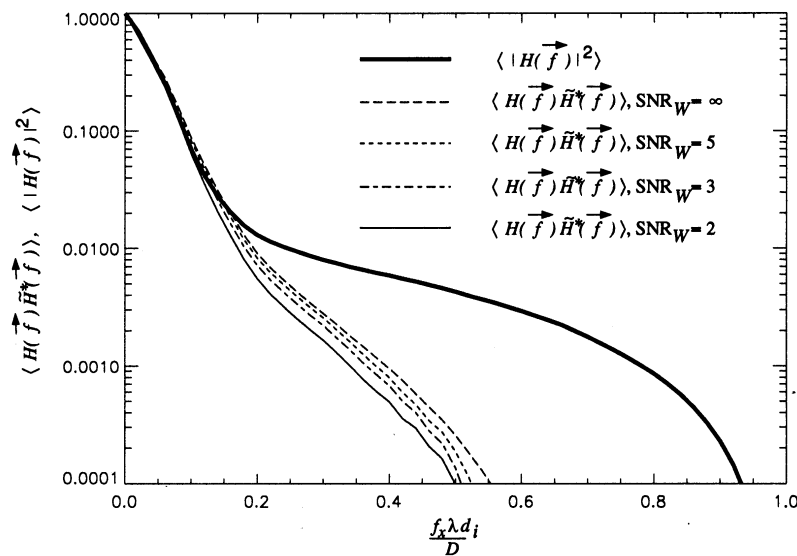
where $D(\vec{f})$ represents the spectrum of the detected photon-limited image and $\text{var}\{\cdot\}$ represents the variance of a random quantity. The analysis of the DWFS signal-to-noise ratio was first presented by Roggemann and Welsh (1994). The result of this analysis is that the signal-to-noise ratio of DWFS is given by

$$\begin{aligned} \text{SNR}_{DW}(\vec{f}) &= \frac{\bar{K} |O_n(\vec{f}) \langle \mathcal{H}(\vec{f}) \tilde{\mathcal{H}}^*(\vec{f}) \rangle|}{(\bar{K} \langle |\tilde{\mathcal{H}}(\vec{f})|^2 \rangle + (\bar{K})^2 |O_n(\vec{f})|^2 \text{var}\{\mathcal{H}(\vec{f}) \tilde{\mathcal{H}}^*(\vec{f})\})^{1/2}}. \end{aligned} \quad (155)$$

Comparing Eq. (155) to the general expression for the signal-to-noise ratio of the unbiased speckle-interferometry estimator $\text{SNR}_Q(\vec{f})$ given in Eq. (125) shows that $\text{SNR}_{DW}(\vec{f})$ is *linear* with respect to the modulus of the normalized object spectrum $|O_n(\vec{f})|$, while $\text{SNR}_Q(\vec{f})$ is a function of $|O_n(\vec{f})|^2$. One consequence of this different dependence on the object spec-



(a)



(b)

FIG. 41. Speckle transfer function and numerator of DWFS transfer function for $\text{SNR}_W = \infty, 5, 3,$ and 2 for (a) $D/r_0 = 2$ and (b) $D/r_0 = 10$.

trum is that DWFS can have a signal-to-noise ratio comparable to speckle interferometry for measuring extended objects. Analytic evaluation of Eq. (155) would require numerical evaluation of an eight-dimensional integral to obtain $\text{var}\{\mathcal{H}(\vec{f})\tilde{\mathcal{H}}^*(\vec{f})\}$. This calculation is impractical on widely available computers. Hence simulations have been used to evaluate Eq. (155) (Roggemann and Welsh, 1994).

Numerical results for $\text{SNR}_{DW}(\vec{f})$ are now presented to illustrate the performance of DWFS. The simulation described by Roggemann and Welsh (1996) was used to obtain numerical values for $\langle \mathcal{H}(\vec{f})\tilde{\mathcal{H}}^*(\vec{f}) \rangle$, $\langle |\tilde{\mathcal{H}}(\vec{f})|^2 \rangle$, and $\text{var}\{\mathcal{H}(\vec{f})\tilde{\mathcal{H}}^*(\vec{f})\}$ for a range of seeing conditions

and wave-front sensor light levels. These statistical quantities were then used to evaluate Eq. (155) for a set of objects and light levels of interest. The simulation was also used to obtain $\langle |\mathcal{H}(\vec{f})|^2 \rangle$, $\langle |\mathcal{H}(2\vec{f})|^2 \rangle$, and $\langle |\mathcal{H}(\vec{f})|^4 \rangle$, so that the signal-to-noise ratio $\text{SNR}_Q(\vec{f})$ of the unbiased speckle-interferometry estimator $Q(\vec{f})$ could be calculated using Eqs. (120) and (121). The optical-system parameters are summarized in Table III.

Photon-limited detection was assumed for both the wave-front sensor and the imaging camera. Integration times in the wave-front sensor and the imaging camera were assumed to be identical. It was further assumed that equal photon-flux densities, specified in units of

TABLE III. Input parameters for DWFS signal-to-noise-ratio results.

Parameter	Value
Pupil diameter D	1 m
Subaperture side length d	0.1 m
Wave-front sensor wavelength λ_w	500 nm
Imaging wavelength λ_I	600 nm
No. of Zernike polynomials	40
r_0	0.5 m, 0.1 m, 0.07 m at $\lambda = 500$ nm
SNR_w	$\infty, 5, 3, 2$
\bar{K}	$\infty, 1963.5, 706.9, 314.2$

photons/(m²s), were present at the telescope pupil at both λ_I and λ_w and that the optical losses and detector quantum efficiencies in the imaging and wave-front sensor legs were identical. Results for four wave-front sensor signal-to-noise-ratio values are presented, $\text{SNR}_w = \infty, 5, 3,$ and 2 , corresponding to wave-front sensor light levels of $\bar{K}_w = \infty, 25, 9,$ and 4 , respectively. With these assumptions the mean number of photoevents per image per integration time \bar{K} can be computed by noting that the telescope aperture is approximately 78.5 times larger than a wave-front sensor subaperture. Hence the appropriate average numbers of photoevents per image per integration time are $\bar{K} = \infty$ for $\text{SNR}_w = \infty$, $\bar{K} = 1963.5$ for $\text{SNR}_w = 5$, $\bar{K} = 706.9$ for $\text{SNR}_w = 3$, and $\bar{K} = 314.2$ for $\text{SNR}_w = 2$. Note that the $\text{SNR}_w = \infty$ case eliminates the effects of measurement noise in the wave-front sensor and image plane, and this provides an upper bound on the performance of both DWFS and speckle interferometry. The Fried seeing parameter r_0 was specified at a wavelength of 500 nm. Specific values of r_0 used to obtain the results that follow are $r_0 = 50$ cm, 10 cm, and 7 cm.

Results are presented for a computer-generated rendering of a simulated satellite object shown in Fig. 42. $\text{SNR}_{DW}(\vec{f})$ for the computer-generated satellite object is shown in Fig. 43, and corresponding results for $\text{SNR}_Q(\vec{f})$ are shown in Fig. 44. The results presented in Figs. 43 and 44 were obtained by computing the full two-dimensional SNR array and then averaging around

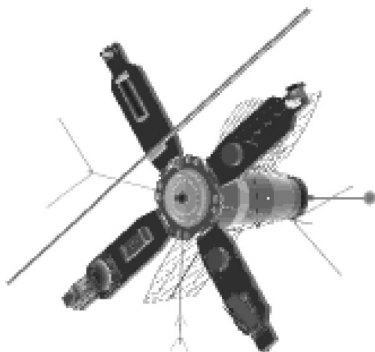


FIG. 42. Computer-generated rendering of a simulated satellite object.

circles of constant radius to express $\text{SNR}_{DW}(\vec{f})$ and $\text{SNR}_Q(\vec{f})$ as functions of a scalar spatial frequency.

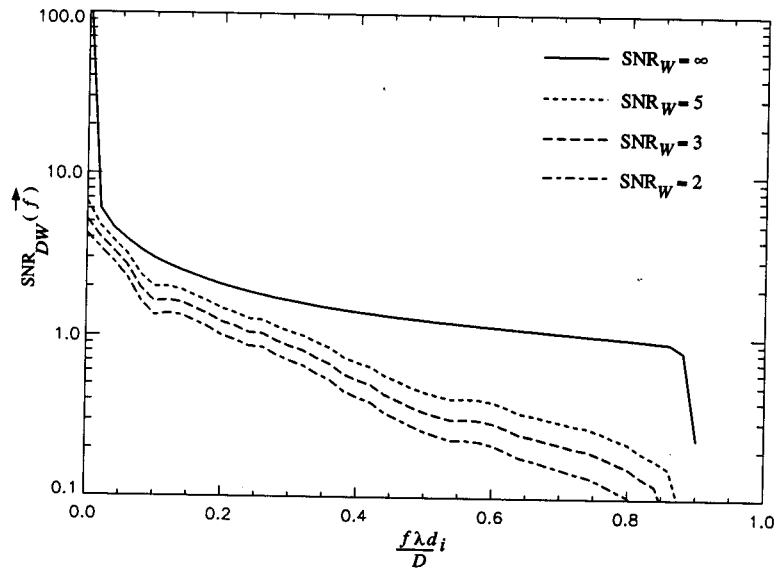
Inspection of Figs. 43 and 44 shows that speckle interferometry has a small signal-to-noise-ratio advantage over DWFS for the *extended-object* case, since $\text{SNR}_{DW}(\vec{f})$ depends upon $|O_n(\vec{f})|$, while $\text{SNR}_Q(\vec{f})$ depends on $|O_n(\vec{f})|^2$, and $|O_n(\vec{f})| < 1$ everywhere except $\vec{f} = 0$ for the extended object. These results allow us to draw the conclusion that speckle interferometry and DWFS can provide competitive performance on extended objects (Welsh and Roggemann, 1994b).

VI. DECONVOLUTION OF COMPENSATED IMAGES

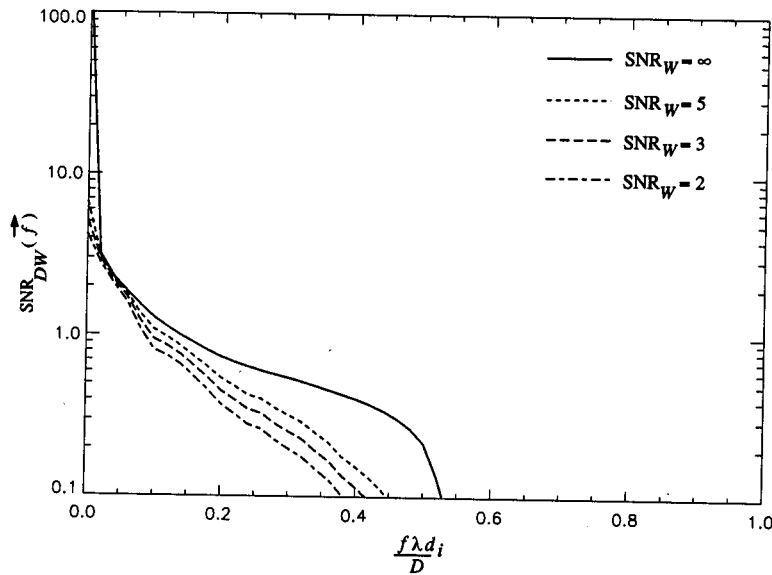
In adaptive-optics imaging systems the optical transfer function varies randomly from instant to instant. Any analysis of adaptive-optics system imaging performance must account for this source of randomness. Both fully and partially compensated adaptive-optics imaging systems provide good signal-to-noise ratio at high spatial frequencies in the measured images (Roggemann, 1991, 1992). However, the average OTF of the atmosphere-telescope system may be highly attenuated in a partially compensated system, which leads to blurred raw-image measurements. Deconvolution of these blurred measured images provides sharper, higher-resolution images. There are, however, limits on deconvolution, imposed by signal-to-noise-ratio effects which must be understood to avoid amplifying noise effects in the deconvolution process. In this subsection we address the spatial-frequency-domain signal-to-noise ratio of the detected image in adaptive-optics imaging systems, present a linear deconvolution measurement and processing algorithm, and discuss the signal-to-noise-ratio-imposed limits on deconvolution of adaptive-optics images.

The theoretical basis for deconvolving compensated images derives from Eq. (69). The key point is that it has been shown that a sufficiently high signal-to-noise ratio exists at sufficiently high frequencies to allow deconvolution of images measured with highly attenuated OTF's (Roggemann, 1991).

Of course, the form of $\text{SNR}_{\mathcal{H}}(\vec{f})$ given in Eq. (70) is critical. Examples of $\langle \mathcal{H}(\vec{f}) \rangle$ and $(\text{var}\{\mathcal{H}(\vec{f})\})^{1/2}$ are



(a)



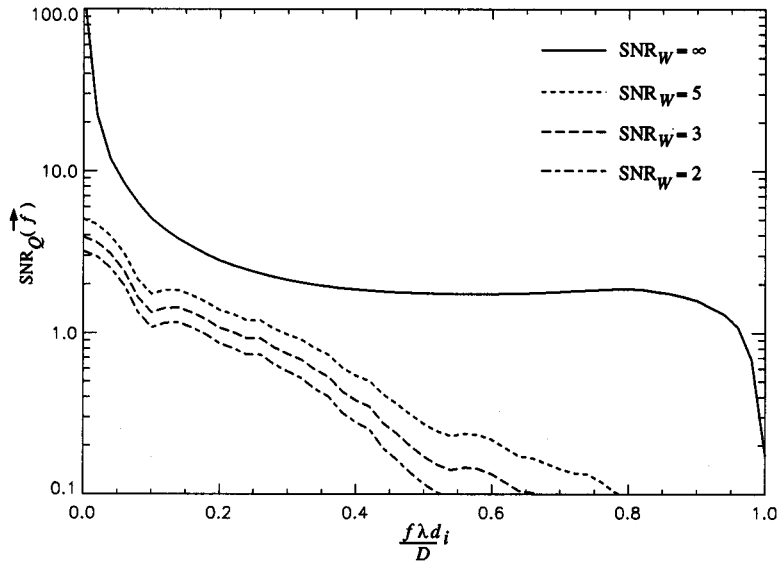
(b)

FIG. 43. $SNR_{DW}(\vec{f})$ for computer-generated satellite object for $SNR_W = \infty, 5, 3,$ and 2 for (a) $r_0 = 50$ cm and (b) $r_0 = 10$ cm.

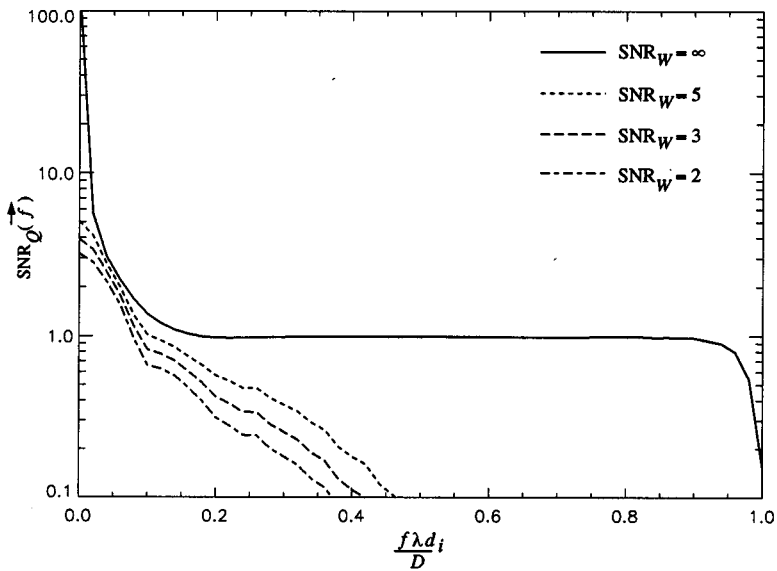
shown in Fig. 45. The associated plot of $SNR_{\mathcal{H}}(\vec{f})$ is shown in Fig. 46. An adaptive-optics simulation described by Roggemann and Welsh (1996) was used to obtain all of the results presented in Fig. 45, using input parameters shown in Table IV. The influence functions of the actuators were modeled as two-dimensional triangle functions (Gaskill, 1978) with base width equal to two times the actuator grid spacing. Least-squares reconstruction was used to map wave-front sensor measurements to actuator commands. It was assumed that no delay between sensing and correcting the turbulence-induced aberration was present in the adaptive-optics system and that the beacon for the wave-front sensor

was infinitely bright, assumptions that make the results presented in Fig. 45 upper bounds on performance. The statistical quantities presented in Fig. 45 were obtained for 200-frame data sets. In all cases the appropriate two-dimensional function was created with the simulation, and the two-dimensional arrays were then averaged around circles of constant radius to obtain results that are a function of a scalar spatial frequency variable.

Observe from Fig. 45 that the $\langle \mathcal{H}(\vec{f}) \rangle$ plots for $r_0 = 7.5$ cm and $r_0 = 5$ cm are significantly lower than for the $r_0 = 20$ cm and $r_0 = 10$ cm cases at all spatial frequencies $|\vec{f}| > 0$. Thus it is expected that the images measured in the $r_0 = 5$ cm, 7.5 cm, and 10 cm cases will be



(a)

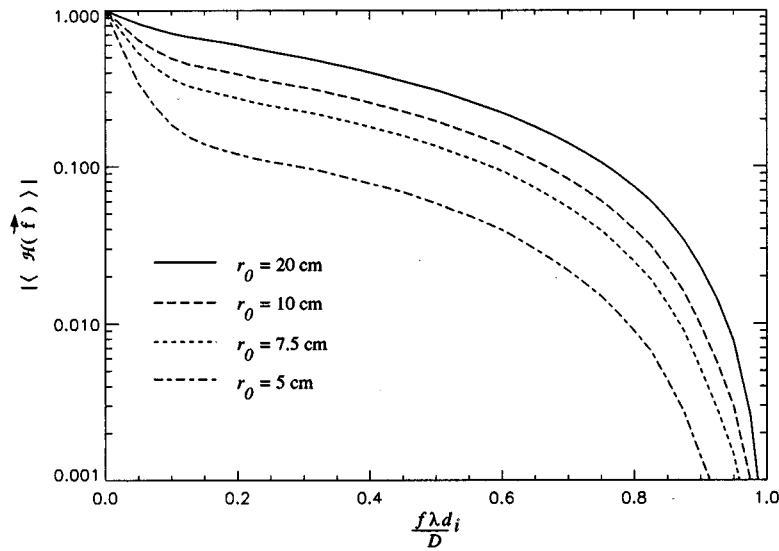


(b)

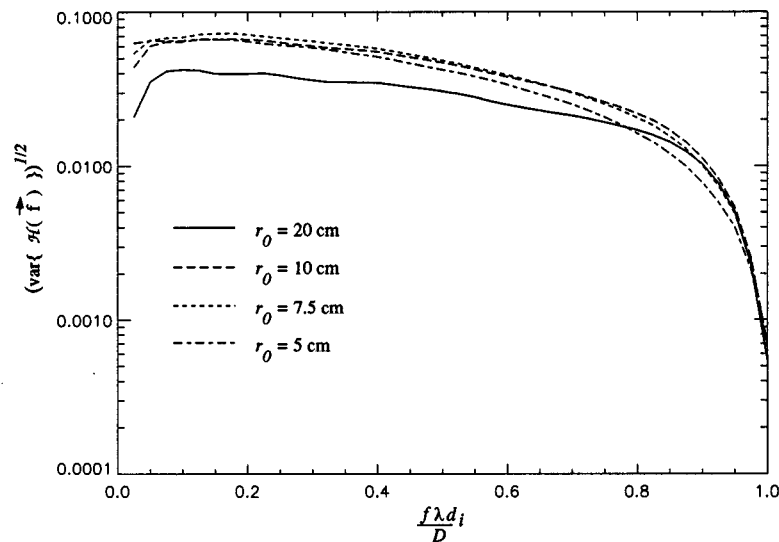
FIG. 44. $SNR_Q(\vec{f})$ for computer-generated satellite object for $SNR_W = \infty, 5, 3,$ and 2 for (a) $r_0 = 50$ cm and (b) $r_0 = 10$ cm.

more blurred than the image measured in the $r_0 = 20$ cm case. Figure 47 shows this expectation to be correct. In Fig. 47 average simulated images of a binary star with components separated by $1.2 \mu\text{rad}$ and brightness ratio of 2:1 are shown for the $r_0 = 20$ cm, 10 cm, 7.5 cm, and 5 cm cases. The adaptive-optics configuration used to generate these figures was identical to the configuration used to generate Fig. 45. However, the images shown in Fig. 47 contain the effects of finite signal levels in the wave-front sensor and in the image plane. The binary star was assumed to have visual magnitude $m_v = 6$ with the same spectral distribution as the sun. The wave-front sensor was assumed to operate in the wavelength range

$\lambda_W = 600 \pm 60$ nm, and the imaging camera was assumed to operate in the wavelength range $\lambda_I = 700 \pm 70$ nm. Integration time of 1 ms was assumed in both the wave-front sensor and the imaging camera, and the transmission efficiency from the top of the atmosphere to the output of both detectors was assumed to be 10%. The result of these assumptions is that the average number of photoevents per integration time per subaperture in the wave-front sensor is $\bar{K}_W = 120$, and the average number of photoevents per image is $\bar{K} = 5358$. Data sets of 200 images were averaged to obtain Fig. 47. Observe that as r_0 decreases the images of the binary-star components become broader and the individual binary-star



(a)



(b)

FIG. 45. Adaptive-optics performance for $r_0=20$ cm, $r_0=10$ cm, $r_0=7.5$ cm, and $r_0=5$ cm: (a) average optical transfer function $\langle \mathcal{H}(\vec{f}) \rangle$ and (b) $(\text{var}\{\mathcal{H}(\vec{f})\})^{1/2}$ for one-meter-diameter telescope.

components become more strongly overlapping, which is consistent with a loss of resolution.

The image-spectrum signal-to-noise ratios $\text{SNR}_D(\vec{f})$ for the binary-star images shown in Fig. 47 are shown in Fig. 48. The plots in Fig. 48 were created by averaging the two-dimensional $\text{SNR}_D(\vec{f})$ arrays along circles of constant radius to create plots that are a function of a scalar spatial frequency. The horizontal axis of Fig. 48 is normalized by the diffraction-limited cutoff frequency for the OTF, $D/(\lambda d_i)$, for the aperture diameter $D=1$ m and the imaging wavelength $\lambda_I=700$ nm. Choosing the threshold of 0.1 on $\text{SNR}_D(\vec{f})$ to define the signal-to-noise-ratio-limited effective cutoff frequency f_{SNR} , which corresponds to $\sqrt{M}\text{SNR}_D(\vec{f}) \approx 1.4$ for the case of

$M=200$ used here, we observe that f_{SNR} lies in the range $0.89 \leq f_{\text{SNR}}\lambda d_i/D \leq 0.97$. Hence, even though the images shown in Fig. 47 are blurred, high signal-to-noise-ratio information is present in the images at high spatial frequencies.

The blurred images shown in Fig. 47 can be sharpened using deconvolution (Biemond *et al.*, 1990; Roggemann, 1992; Roggemann and Matson, 1992; Gonzalez and Woods, 1993). The goal of deconvolution is to remove, or at least reduce, the effects of the average OTF on images. Two simple and widely used deconvolution techniques are the inverse filter and the Wiener filter (Gonzalez and Woods, 1993). In the noise-free case an estimate of the object spectrum $\tilde{O}(\vec{f})$ within the pass-

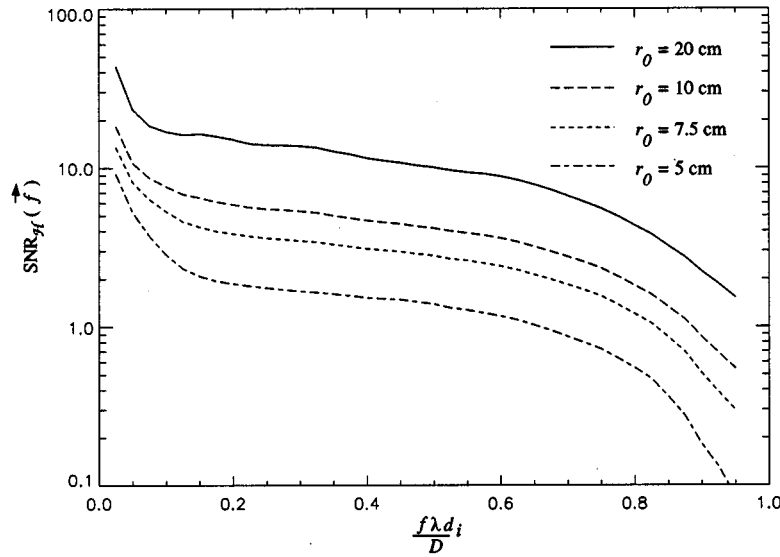


FIG. 46. $SNR_{\mathcal{H}}(\vec{f})$ for $r_0=20$ cm, $r_0=10$ cm, $r_0=7.5$ cm, and $r_0=5$ cm for a one-meter-diameter telescope.

band of $\mathcal{H}(\vec{f})$ can easily be obtained if the OTF $\mathcal{H}(\vec{f})$ is known by using

$$\tilde{O}(\vec{f}) = \frac{I(\vec{f})}{\mathcal{H}(\vec{f})} = \frac{O(\vec{f})\mathcal{H}(\vec{f})}{\mathcal{H}(\vec{f})}, \tag{156}$$

which is the classic inverse filter (Gonzalez and Woods, 1993). In the context of adaptive-optics imaging of space objects it must be noted that both the OTF and the detected image are random. Hence it is necessary to work with the average detected image spectrum $\langle D(\vec{f}) \rangle$ and an estimate of the average OTF obtained from a reference star $\langle \mathcal{H}^{\text{ref}}(\vec{f}) \rangle$. The estimate of the average OTF $\langle \mathcal{H}^{\text{ref}}(\vec{f}) \rangle$ is obtained by measuring images of a nearby reference star $d^{\text{ref}}(\vec{x})$ and then computing the average OTF using

$$\langle \mathcal{H}^{\text{ref}}(\vec{f}) \rangle = \left\langle \frac{D^{\text{ref}}(\vec{f})}{D^{\text{ref}}(0)} \right\rangle, \tag{157}$$

where $D^{\text{ref}}(\vec{f})$ has been used to represent the Fourier transform of $d^{\text{ref}}(\vec{x})$.

The appropriate form of the object-spectrum estimate $\tilde{O}(\vec{f})$ obtained from the detected image spectrum $D(\vec{f})$ using the classic inverse filter is given by

$$\tilde{O}(\vec{f}) = \frac{\langle D(\vec{f}) \rangle}{\langle \mathcal{H}^{\text{ref}}(\vec{f}) \rangle} \tag{158}$$

for $\langle \mathcal{H}^{\text{ref}}(\vec{f}) \rangle \neq 0$, and

$$\tilde{O}(\vec{f}) = 0 \tag{159}$$

for $\langle \mathcal{H}^{\text{ref}}(\vec{f}) \rangle = 0$.

Unfortunately, the classic inverse filter cannot be directly applied to realistic astronomical imaging problems because it neglects measurement-noise effects. To see how the object-spectrum estimate $\tilde{O}(\vec{f})$ obtained from the classic inverse filter is affected by noise, consider the simplified case of an image spectrum $I_C(\vec{f})$ corrupted with additive noise $N(\vec{f})$, given by

$$I_C(\vec{f}) = O(\vec{f})\mathcal{H}(\vec{f}) + N(\vec{f}), \tag{160}$$

TABLE IV. Input parameters for adaptive-optics imaging results.

Parameter	Value
Pupil diameter D	1 m
Subaperture side length d	0.1 m
Actuator spacing	0.12 m
Wave-front sensor wavelength λ_w	600 nm
Imaging wavelength λ_I	700 nm
Number of independent frames	200
r_0	0.2 m, 0.1 m, 0.07 m, 0.05 m at $\lambda=500$ nm
\bar{K}_w	120
\bar{K}	5 358

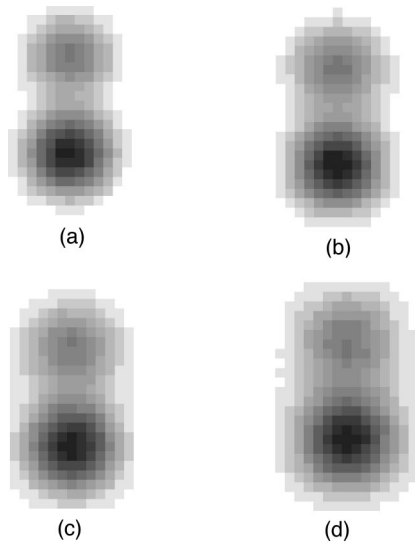


FIG. 47. Average simulated binary-star images using adaptive optics: (a) $r_0=20$ cm; (b) $r_0=10$ cm; (c) $r_0=7.5$ cm; (d) $r_0=5$ cm. Angular separation of the binary components is $1.2 \mu\text{rad}$, the telescope diameter is 1.0 m, and the ratio of brightnesses is $2:1$. Negative images are displayed for clarity.

where we shall assume that the OTF $\mathcal{H}(\vec{f})$ is perfectly known. Let us now apply the classic inverse filter to $I_C(\vec{f})$ to obtain an estimate of the object spectrum $\tilde{O}_c(\vec{f})$, given by

$$\tilde{O}_c(\vec{f}) = \frac{I_C(\vec{f})}{\mathcal{H}(\vec{f})} = \frac{O(\vec{f})\mathcal{H}(\vec{f})}{\mathcal{H}(\vec{f})} + \frac{N(\vec{f})}{\mathcal{H}(\vec{f})}. \quad (161)$$

The first term of Eq. (161) is the desired result. The second term of Eq. (161) is not desired, since it contains the effects of additive noise. Recall that $\mathcal{H}(\vec{f})$ takes its maximum value of unity at $\vec{f}=0$ and is less than unity

everywhere else. Hence we conclude from Eq. (161) that the effect of inverse filtering on images corrupted with additive noise is both to sharpen the image and to *amplify the noise*. Photon-noise effects in $\langle D(\vec{f}) \rangle$ are also amplified by the classic inverse filter, even though this noise cannot be modeled as additive in nature.

Noise amplification by the classic inverse filter is not a serious problem in spatial frequency regions where $\langle \mathcal{H}^{\text{ref}}(\vec{f}) \rangle$ and $\text{SNR}_D(\vec{f})$ are significantly greater than zero. However, when $\langle \mathcal{H}^{\text{ref}}(\vec{f}) \rangle$ or $\text{SNR}_D(\vec{f})$ are small, noise amplification effects can dominate the object irradiance distribution estimate $\tilde{o}(\vec{x})$ (Biamond *et al.*, 1990; Gonzalez and Woods, 1993). The general character of $\tilde{o}(\vec{x})$ obtained using the classic inverse filter directly on noisy images is that $\tilde{o}(\vec{x})$ is also very noisy, such that in some cases the actual object irradiance distribution may be completely obscured by the noise effects (Biamond *et al.*, 1990).

One technique for overcoming some of the noise effects associated with the classic inverse filter is to pass the $\tilde{O}(\vec{f})$ obtained from the inverse filter through an additional filtering step. A new object-spectrum estimate $\tilde{O}_1(\vec{f})$ is obtained from this additional filtering step given by

$$\tilde{O}_1(\vec{f}) = \tilde{O}(\vec{f})H(\vec{f}), \quad (162)$$

where $H(\vec{f})$ represents the filter applied to $\tilde{O}(\vec{f})$ (Roggemann *et al.*, 1992).

The results of reconstructing the images shown in Fig. 47 using Eq. (162) are shown in Fig. 49. Comparison of Figs. 47 and 49 shows that the outcome of the deconvolution process is a sharper image, that is, an image in which the components of the binary star are more clearly defined and the halo surrounding the binary-star components has been reduced. However, consistent with the earlier discussion of noise effects in inverse filtering, the deconvolved images are somewhat noisier than the

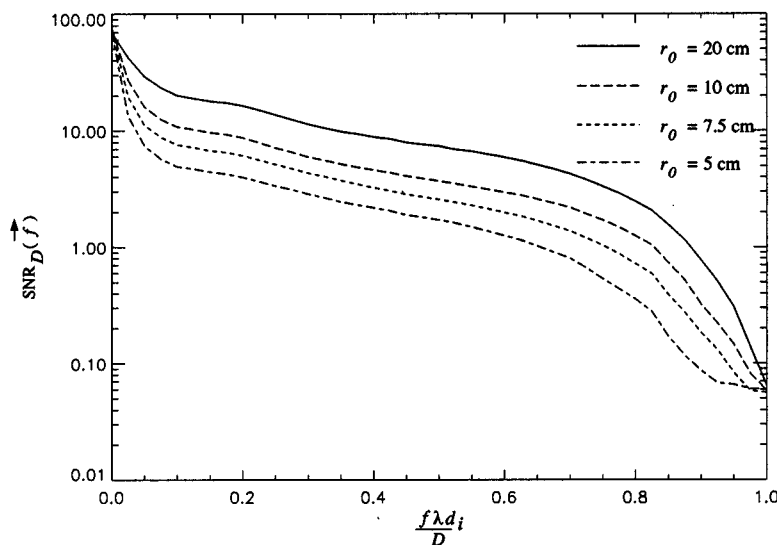


FIG. 48. Image-spectrum signal-to-noise ratio $\text{SNR}_D(\vec{f})$ for the binary-star images shown in Fig. 47.

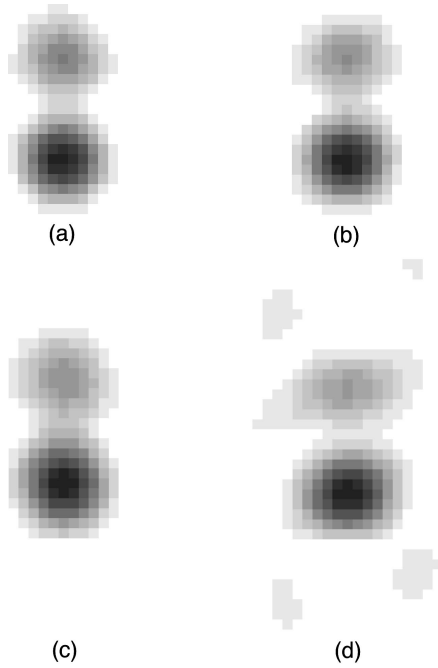


FIG. 49. Simulated binary-star images measured using adaptive optics and reconstructed using the classic inverse filter followed by the cone filter: (a) $r_0=20$ cm; (b) $r_0=10$ cm; (c) $r_0=7.5$ cm; (d) $r_0=5$ cm. Angular separation of the binary components is $1.2 \mu\text{rad}$, the telescope diameter is 1.0 m, and the ratio of brightnesses is $2:1$. Negative images are displayed for clarity.

measured images. Noise effects are particularly evident in Fig. 49(d), where some noise-induced artifacts in the reconstructed image are present.

Another technique for overcoming noise effects in deconvolution is the so-called Wiener filter (Biemond *et al.*, 1990; Gonzalez and Woods, 1993). The appropriate form of the Wiener filter $H_W(\vec{f})$ in the present context is

$$H_W(\vec{f}) = \frac{\langle \mathcal{H}^{\text{ref}}(\vec{f}) \rangle^*}{|\langle \mathcal{H}^{\text{ref}}(\vec{f}) \rangle|^2 + E_N(\vec{f})/E_O(\vec{f})}, \quad (163)$$

where $E_N(\vec{f})$ is the power spectral density of the noise and $E_O(\vec{f})$ is the power spectral density of the object-irradiance distribution. The object-spectrum estimate obtained using the Wiener filter is given by

$$\tilde{O}(\vec{f}) = \langle D(\vec{f}) \rangle H_W(\vec{f}). \quad (164)$$

While the Wiener filter is a minimum-error filter, the form of the Wiener filter given in Eq. (163) is rarely used in practice because one must know the power spectral density of the object irradiance distribution $\mathcal{E}_O(\vec{f})$ (Biemond *et al.*, 1990). Rather, modified, suboptimal versions of the Wiener filter are used. One useful form is given by

$$H_W^{\text{mod}}(\vec{f}) = \frac{\langle \mathcal{H}^{\text{ref}}(\vec{f}) \rangle^*}{|\langle \mathcal{H}^{\text{ref}}(\vec{f}) \rangle|^2 + \alpha/\text{SNR}_D(\vec{f})}, \quad (165)$$

where $0 \leq \alpha \leq 1$ is a user-selected parameter. The motivation for the second term in the denominator of Eq. (165) derives from the interpretation of the $E_N(\vec{f})/E_O(\vec{f})$ term in Eq. (163) as a “noise-to-signal” ratio. Qualitatively, the purpose of the $\alpha/\text{SNR}_D(\vec{f})$ term in Eq. (165) is to reduce the response of $H_W^{\text{mod}}(\vec{f})$ in regions where $\text{SNR}_D(\vec{f})$ is small, thereby mitigating some of the noise-amplification effects that would be present in the classic inverse filter. The parameter α can be varied in Eq. (165) to obtain a visually pleasing $\tilde{O}(\vec{x})$. As a final comment, we note that, while the Wiener filter defined in Eq. (163) minimizes a measure of mean-squared error in image space, the reconstructions obtained with the Wiener filter have been criticized as “overly smooth” for human visual-system interpretation (Biemond *et al.*, 1990).

While we have only presented reconstructed images that are based on linear filtering ideas, it must be noted that several nonlinear image reconstruction algorithms have been explored, which may be appropriate for use on adaptive-optics imagery. There are currently at least five classes of nonlinear algorithms: (1) those based on maximum-likelihood estimation (Richardson, 1972; Lucy, 1974; Schulz, 1993); (2) the blind deconvolution algorithm (Ayers and Dainty, 1988; Davey *et al.*, 1989; Jefferies and Christou, 1993); (3) the CLEAN algorithm (Thompson *et al.*, 1986; Fried, 1995); (4) the maximum-entropy algorithm (Frieden, 1972; Frieden and Burke, 1972; Gull and Daniell, 1978; Cornwell and Evans, 1985); and (5) super-resolution algorithms (Sementilli *et al.*, 1993). The Richardson-Lucy algorithm is based on treating the image and the object as probability density functions and estimating the most likely object to have caused the measured image. Blind deconvolution is a constrained iterative approach to image reconstruction, which allows joint estimation of both the object and the associated point-spread function. The CLEAN algorithm is an iterative algorithm that uses successive subtraction of properly weighted and located “dirty point-spread functions” (i.e., the point-spread function associated with a very sparse array) located at the brightest point in the image. A properly weighted and located “desired” point-spread function, often chosen to be a Gaussian function, is simultaneously placed in a “clean” image array. This process is repeated until the residual image in the original array reaches the rms noise level of the data. The CLEAN algorithm is widely used to reconstruct images obtained in radio astronomy. The maximum-entropy algorithm is based on maximizing a specialized measure of error, which is based on the concept of entropy used in information theory, between the measured data and a model of the solution. Finally, super-resolution algorithms attempt both to obtain an accurate estimate of the object spectrum within the measured passband of the telescope, and to reconstruct the object spectrum *outside* the measured passband. The most recently proposed super-resolution algorithm is based on a maximum *a posteriori* estimation scheme using a Poisson model for the detected image. While these

algorithms hold promise for reconstructing adaptive-optics images, the effects of measurement noise and turbulence-induced randomness on the various estimators and the associated reconstructed images have not been fully evaluated.

VII. COMPENSATED SPECKLE IMAGING

Compensated speckle imaging is the term used to describe the application of speckle-imaging techniques, introduced in Sec. IV, to images measured with adaptive optical imaging systems. The compensated-speckle-imaging paradigm is as follows. An adaptive optical imaging system is used to measure a data set of short-exposure images of the object of interest. A similar data set is obtained for a nearby reference star. The object spectrum is then estimated from the measurements using speckle-imaging algorithms, and an estimate of the object irradiance distribution is obtained by applying an inverse Fourier transform to the estimated spectral data. Motivation for compensated speckle imaging arises from the fact that it has been shown that limited or partial wave-front phase correction improves the residual wave-front phase statistics, improving the statistical performance of the speckle-imaging estimators (Roggemann and Matson, 1992).

Historically, Nisenson and Barakat (1987) were the first to note that limited wave-front correction significantly improves the performance of speckle-imaging estimators. Roggemann and Matson (1992) later extended this idea by deriving a rigorous expression for the signal-to-noise ratio of the unbiased speckle-interferometry estimator $Q(\vec{f})$. Roggemann and Matson also showed that even very limited predetection wave-front correction results in improvements in both the signal-to-noise ratio of $Q(\vec{f})$, $\text{SNR}_Q(\vec{f})$ and the phase-spectrum estimate. One key result of their analysis is that, when adaptive-optics correction is applied, $\text{SNR}_Q(\vec{f})$ is not bounded from above by unity for spatial frequencies in the range $|\vec{f}| > r_0/(\lambda d_i)$, as is the case when no adaptive-optics compensation is present (Dainty and Greenaway, 1979). Subsequent experimental results confirmed the key predictions of earlier theoretical work in compensated speckle imaging (Roggemann, Caudill *et al.*, 1994).

Compensated speckle imaging is most easily studied using a simulation. The simulation used to obtain the results that follow implements predetection wave-front correction as described by Roggemann and Welsh (1996). Speckle-imaging post processing was then applied to the simulated images. Labeyrie's speckle-interferometry technique, presented in Sec. IV.B, was used to estimate the modulus squared of the object spectrum $|\tilde{O}_n(\vec{f})|^2$. The bispectrum phase reconstruction technique, which was presented in Sec. IV.C.2, was used to obtain an estimate of the phase of the object spectrum $\tilde{\phi}(\vec{f})$. The telescope was modeled as a one-meter-diameter unobscured aperture. A Hartmann-type wave-front sensor was modeled with square subapertures having a side length of 10 cm. The influence functions of

the deformable-mirror actuators were modeled as two-dimensional triangle functions (Gaskill, 1978) with base width equal to two times the actuator grid spacing. The deformable-mirror actuators were placed on a Cartesian grid with grid spacing of 12 cm. Least-squares reconstruction, described in Sec. III.B.3, was used to map wave-front sensor measurements to actuator commands. It was assumed that no delay between sensing and correcting for the turbulence-induced aberration was present in the adaptive-optics system.

To illustrate the effects of adaptive-optics compensation on $\text{SNR}_Q(\vec{f})$, adaptive-optics imaging of a single star was simulated. These input parameters are summarized in Table IV. The star was assumed to have visual magnitude $m_v=6$ with the same spectral distribution as the sun. The wave-front sensor was assumed to operate in the wavelength range $\lambda_w=600\pm 60$ nm, and the imaging camera was assumed to operate in the wavelength range $\lambda_I=700\pm 70$ nm. The Fried seeing parameter r_0 was specified at the wavelength of 500 nm, and four different values of r_0 were used: $r_0=20$ cm, 10 cm, 7.5 cm, and 5 cm. Integration times of 1 ms were assumed in both the wave-front sensor and the imaging camera, and the transmission efficiency from the top of the atmosphere to the output of both detectors was assumed to be 10%. The result of these assumptions is that the average number of photoevents per integration time per subaperture in the wave-front sensor is $\bar{K}_w=120$, and the average number of photoevents per image is $K=5358$. Data sets of 200 images were used to obtain sample-based estimates of $\langle Q(\vec{f}) \rangle$, $\text{SNR}_Q(\vec{f})$, and the average bispectrum $\langle B(\vec{f}_1, \vec{f}_2) \rangle$.

$\text{SNR}_Q(\vec{f})$ results for the single-star images are presented in Fig. 50. The plots in Fig. 50 were created by averaging the two-dimensional $\text{SNR}_Q(\vec{f})$ arrays along circles of constant radius to create plots that are a function of a scalar spatial frequency. The horizontal axis of Fig. 50 is normalized by the diffraction-limited cutoff frequency of the OTF, $D/(\lambda d_i)$, for the aperture diameter $D=1$ m and the imaging wavelength $\lambda_I=700$ nm. In contrast to the uncompensated-speckle-imaging case, illustrated in Fig. 37, $\text{SNR}_Q(\vec{f})$ is not bounded from above by unity for spatial frequencies in the range $|\vec{f}| \geq r_0/(\lambda d_i)$, when adaptive optics are used. Hence in compensated speckle imaging fewer frames must be averaged to obtain a desired level of $\text{SNR}_Q(\vec{f})$, or, conversely, a higher value of $\text{SNR}_Q(\vec{f})$ is obtained from a fixed number of compensated frames.

VIII. CONCLUSION

In this paper we have reviewed the effects of atmospheric turbulence on imaging systems and emerging technologies for overcoming the effects of turbulence.

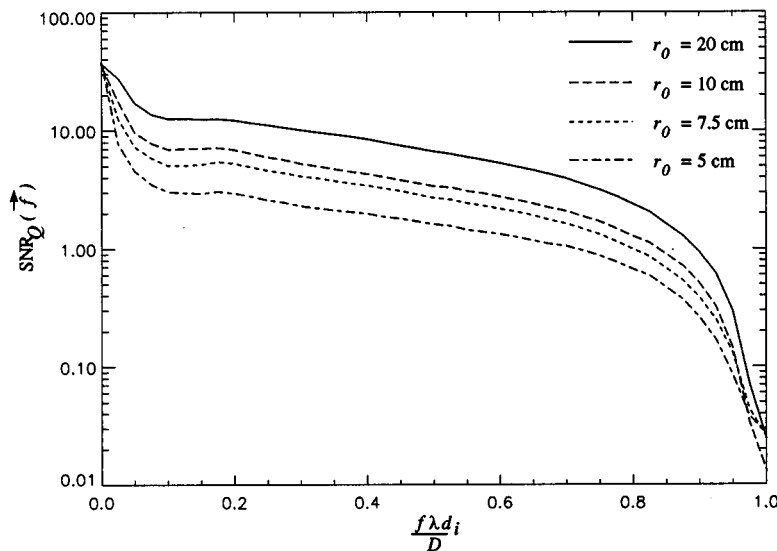


FIG. 50. $\text{SNR}_Q(\vec{f})$ for adaptive-optics-imaging case of a single star with $m_v=6$ and $r_0=20$ cm, 10 cm, 7.5 cm, and 5.0 cm.

As these technologies mature and come into more widespread use, we will certainly be presented with clearer pictures of the sky and deepening knowledge of the universe. We expect that, even in the age of the space telescope, ground-based astronomy will continue to play a large and important role in the continuing effort to understand the universe, due to the complexity and expense of space systems and limitations on the diameter of a primary mirror that can be boosted into space. However, many challenges remain to fully exploit adaptive optics and image reconstruction technologies. In this final section we comment on the direction of present research and possibilities for future research.

One of the most fundamental unresolved issues in atmospheric and adaptive optics is the small correctable field of view, or isoplanatic angle, provided by adaptive-optics systems, which is limited to a few tens of micro-radians at visible wavelengths. The small isoplanatic angle imposes a severe barrier to performing high-resolution sky surveys. Efforts to overcome the isoplanatic-angle limitation will receive a great deal of attention in the future. Promising efforts include use of multiple artificial guide stars (Sasiela, 1994) and use of multiple wave-front sensors and multiple deformable mirrors that correct for the effects of various layers in the atmosphere (Beckers, 1988; Johnston and Welsh, 1994).

Another area for future research is the development of control algorithms for deformable mirrors. It has been shown that minimum-variance controllers, which use information about measurement noise of the wave-front sensor and the correlations present in the turbulence-induced phases, provide superior performance to least-squares approaches to controlling the deformable mirror (Roggemann, 1992). However, implementing a minimum-variance controller requires knowledge of the signal and noise levels in the wave-front sensor, and the current seeing conditions. These quantities can change significantly over the course of a

night's observation, implying that the controller will need to be updated in near real time. Hence, to make a truly optimal deformable-mirror controller, steps must be taken to monitor the local seeing conditions and the wave-front sensor's signal-to-noise ratio, and this information must be used to update the deformable-mirror controller to maintain optimal performance.

Given the complexity and expense of adaptive-optics systems and the push toward making telescopes on the order of eight to ten meters in diameter, it is safe to assume that so-called partially compensated adaptive-optics systems will continue to be of interest in astronomy. Use of partial compensation provides dramatic improvements in resolution over uncompensated imaging, and post-detection image processing has been shown to further improve resolution for partially compensated imaging systems. Hence we expect that the application of advanced image reconstruction algorithms and the evaluation of the performance of these algorithms on dim objects will continue to be an area of active research interest.

Finally, the desire to measure higher-resolution images of the sky than could be obtained with any present or envisioned monolithic aperture remains strong. Hence optical interferometric systems, which extend long-baseline radio-astronomy concepts to optical wavelengths will likely be an active research area. These interferometers will consist of large, physically separated telescopes connected by optical fibers or optical relays based on mirrors. Measurements made by these interferometers, when processed by appropriate reconstruction algorithms, will measure the finest details of the sky ever seen. However, the challenges to optical interferometry are large. For example, the individual apertures must be compensated for atmospheric turbulence effects, and the path-length differences between the telescopes and the beam-combining and fringe-measurement system must be carefully controlled. While these problems are difficult, the promise of interferometric imaging will moti-

vate an active research community to continue developing the required technology.

REFERENCES

- Acton, D. S., and R. C. Smithson, 1992, "Solar imaging with a segmented adaptive mirror," *Appl. Opt.* **31**, 3161–3169.
- Aleksoff, C. C., C. Dainty, J. R. Fienup, R. Q. Fugate, J.-M. Mariotti, P. Nisenson, F. Roddier, and A. M. Tai, 1993, "Unconventional imaging systems," in *The Infrared and Electro-Optical Systems Handbook*, edited by S. R. Robinson (SPIE, Bellingham, WA), Vol. 8, pp. 1–164.
- Ayers, G. R. and J. C. Dainty, 1988, "Iterative blind deconvolution method and its applications," *Opt. Lett.* **13**, 547–549.
- Ayers, G. R., M. J. Northcott, and J. C. Dainty, 1988, "Knox-Thompson and triple correlation imaging through atmospheric turbulence," *J. Opt. Soc. Am. A* **5**, 963–985.
- Babcock, H. W., 1953, "The possibility of compensating astronomical seeing," *Publ. Astron. Soc. Pac.* **65**, 229–236.
- Bates, R. H. T., 1982, "Astronomical speckle imaging," *Phys. Rep.* **90**, 203–297.
- Beckers, J. M., 1988, "Increasing the size of the isoplanatic patch with multiconjugate adaptive optics," in *Proceedings of the ESO Conference on Very Large Telescopes and their Instruments*, edited by M. H. Ulrich (European Southern Observatory, Garching, Germany), pp. 693–703.
- Beckers, J. M., 1993, "Adaptive optics for astronomy: principles, performance, and applications," *Annu. Rev. Astron. Astrophys.* **31**, 13–62.
- Beletic, J. W., 1989, "Deterministic photon bias in speckle imaging," *Opt. Commun.* **71**, 130–133.
- Beletic, J. W., and R. M. Goody, 1992, "Recovery of planetary images by speckle imaging," *Appl. Opt.* **31**, 6909–6921.
- Bertolotti, M., L. Musii, and D. Sette, 1970, "Correlation measurements on partially coherent beams by means of an integration technique," *J. Opt. Soc. Am.* **60**, 1603–1607.
- Biemond, J., R. L. Lagendijk, and R. M. Mersereau, 1990, "Iterative methods for image deblurring," *Proc. IEEE* **78**, 856–883.
- Born, M. and E. Wolf, 1964, *Principles of Optics* (Pergamon, New York).
- Cannon, R. C., 1995, "Global wave-front reconstruction using Shack-Hartmann sensor," *J. Opt. Soc. Am. A* **12**, 2031–2039.
- Cao, G., and X. Yu, 1994, "Accuracy analysis of a Hartmann-Shack wavefront sensor operated with a faint source," *Opt. Eng.* **33**, 2331–2335.
- Cochran, G. M., B. L. Ellerbroek, and D. L. Fried, 1988, "Spectral and temporal windows in Knox-Thompson imaging," Technical Report TR-819R, the Optical Sciences Company.
- Colavita, M. M., 1990, "Design considerations for very long baseline fringe-tracking interferometers," in *Amplitude and Intensity Interferometry*, edited by J. Breckinridge (SPIE, Bellingham, WA), Proceedings of SPIE Vol. 1237, pp. 80–86.
- Collins, G. P., 1992, "Making stars to see stars: DoD adaptive optics work in declassified," *Phys. Today* **45** (2), 17–21.
- Conan, J. M., G. Rousset, and P. Y. Madec, 1995, "Wave-front temporal spectra in high-resolution imaging through turbulence," *J. Opt. Soc. Am. A* **12**, 1559–1570.
- Cornwell, T. J., and K. F. Evans, 1985, "A simple maximum entropy deconvolution algorithm," *Astron. Astrophys.* **143**, 77–83.
- Dai, G., 1995, "Modal compensation of atmospheric turbulence with the use of Zernike polynomials and Karhunen-Loève functions," *J. Opt. Soc. Am. A* **12**, 2182–2193.
- Dainty, J. C., 1975, "Stellar speckle interferometry," in *Topics in Applied Physics: Laser Speckle and Related Phenomena*, edited by J. C. Dainty (Springer, Berlin), Vol. 9, pp. 255–280.
- Dainty, J. C., and A. H. Greenaway, 1979, "Estimation of spatial power spectra in speckle interferometry," *J. Opt. Soc. Am.* **5**, 786–790.
- Davey, B. L. K., R. G. Lane, and R. H. T. Bates, 1989, "Blind deconvolution of noisy complex-valued image," *Opt. Commun.* **69**, 353–356.
- Dayton, D., B. Pierson, B. Spielbusch, and J. Gonglewski, 1992, "Atmospheric structure function measurements with a Shack-Hartmann wave-front sensor," *Opt. Lett.* **17**, 1737–1739.
- Demerlé, M., P. Y. Madec, and G. Rousset, 1994, "Servo-loop analysis for adaptive optics," in *Adaptive Optics for Astronomy*, edited by D. Alloin and J.-M. Mariotti (Kluwer Academic, Boston), NATO Advanced Study Institute Series Vol. C423 pp. 73–88.
- Downie, J. D., and J. W. Goodman, 1989, "Optimal wavefront control for adaptive segmented mirrors," *Appl. Opt.* **28**, 5326–5332.
- Ealey, M. A., and J. F. Washeba, 1990, "Continuous facesheet low voltage deformable mirrors," *Opt. Eng.* **29**, 1191–1198.
- Ealey, M. A., and J. A. Wellman, 1991, "Deformable mirrors: design fundamentals, key performance specifications, and parametric trades," in *Active and Adaptive Optical Components*, edited by M. A. Ealey (SPIE, Bellingham, WA), Proceedings of SPIE Vol. 1543, pp. 36–51.
- Ellerbroek, B. L., 1994, "First-order performance evaluation of adaptive optics systems for atmospheric turbulence compensation in extended field-of-view astronomical telescopes," *J. Opt. Soc. Am. A* **11**, 783–805.
- Ellerbroek, B. L., C. V. Loan, N. P. Pitsianis, and R. J. Plemmons, 1994, "Optimizing closed-loop adaptive-optics performance with use of multiple control bandwidths," *J. Opt. Soc. Am. A* **11**, 2871–2886.
- Fontanella, J., 1985, "Analyse de surface d'onde, deconvolution et optique active," *J. Opt. (France)* **16**, 257–268.
- Foy, R., and A. Labeyrie, 1985, "Feasibility of adaptive telescopes with laser probe," *Astron. Astrophys.* **152**, 129–131.
- Fried, D. L., 1965, "Statistics of a geometric representation of wavefront distortion," *J. Opt. Soc. Am.* **55**, 1427–1435.
- Fried, D. L., 1966a, "Limiting resolution looking down through the atmosphere," *J. Opt. Soc. Am.* **56**, 1380–1384.
- Fried, D. L., 1966b, "Optical resolution through a randomly inhomogeneous medium for very long and very short exposures," *J. Opt. Soc. Am.* **56**, 1372–1379.
- Fried, D. L., 1977, "Least-square fitting a wave front distortion estimate to an array of phase-difference measurements," *J. Opt. Soc. Am.* **67**, 370–375.
- Fried, D. L., 1982, "Anisoplanatism in adaptive optics," *J. Opt. Soc. Am.* **72**, 52–61.
- Fried, D. L., 1987, "Post detection wave front compensation," in *Digital Image Recovery and Synthesis*, edited by P. S. Idell (SPIE, Bellingham, WA), Proceedings of SPIE Vol. 828, pp. 127–133.
- Fried, D. L., 1990, "Time-delay-induced mean-square error in adaptive optics," *J. Opt. Soc. Am. A* **7**, 1224–1225.

- Fried, D. L., 1994a, "Analysis of fundamental limits to artificial guide star adaptive optics system performance for astronomical imaging," *J. Opt. Soc. Am. A* **11**, 277–287.
- Fried, D. L., 1994b, "Atmospheric turbulence optical effects: understanding the adaptive-optics implications, in *Adaptive Optics for Astronomy*, edited by D. Alloin and J.-M. Mariotti (Kluwer Academic, Boston), NATO Advanced Study Institute Series Vol. C423, pp. 25–57.
- Fried, D. L., 1995, "Analysis of the CLEAN algorithm and implications for superresolution," *J. Opt. Soc. Am. A* **12**, 853–860.
- Fried, D. L., and D. L. Hench, 1990, "Spectral bandwidth and adaptive optics considerations for white light speckle imagery," Technical Report TR-1033, the Optical Sciences Company.
- Frieden, B. R., 1972, "Restoring with maximum likelihood and maximum entropy," *J. Opt. Soc. Am.* **62**, 511–518.
- Frieden, B. R., and J. J. Burke, 1972, "Restoring with maximum entropy, II: superresolution of photographs of diffraction-blurred images," *J. Opt. Soc. Am.* **62**, 1202–1210.
- Fugate, R. Q., 1993, "Laser beacon adaptive optics," *Opt. Photonics News* **4**, 14–19.
- Fugate, R. Q., 1994, "Observations of faint objects with laser beacon adaptive optics," in *Adaptive Optics in Astronomy*, edited by M. A. Ealey and F. Merkle (SPIE, Bellingham, WA), Proceedings of SPIE Vol. 2201, pp. 10–21.
- Fugate, R. Q., B. L. Ellerbroek, C. H. Higgins, M. P. Jelonek, W. J. Lange, A. C. Slavin, W. J. Wild, D. M. Winker, J. M. Wynia, J. M. Spinhirne, B. R. Boeke, R. E. Ruane, J. F. Moroney, M. D. Olikier, D. W. Sindle, and R. A. Cleis, 1994, "Two generations of laser-guide-star adaptive-optics experiments at the starfire optical range," *J. Opt. Soc. Am. A* **11**, 301–314.
- Fugate, R. Q., C. H. Higgins, J. M. Spinhirne, B. R. Boeke, R. A. Cleis, D. W. Swindle, and M. D. Olikier, 1993, "Laser beacon adaptive optics with an unintensified CCD wave-front sensor and fiber optic synthesized array of silicon avalanche photodiodes for fast guiding," in *ESO Conference and Workshop. Proceedings on Active and Adaptive Optics*, edited by F. Merkle (European Southern Observatory, Garching Germany), Vol. 48, pp. 487–492.
- Fugate, R. Q., J. F. Riker, J. T. Roark, S. Stogsdill, and B. D. O'Neil, 1996, "Laser beacon compensated images of Saturn using a high-speed, near-infrared correlation tracker," in *ESO Conference and Workshop Proceedings on Active and Adaptive Optics*, edited by M. Cullum (European Southern Observatory, Garching, Germany), Vol. 54, pp. 287–290.
- Gaffard, J. P., and Boyer, C., 1987, "Adaptive optics for optimization of image resolution," *Appl. Opt.* **26**, 3772–3777.
- Gardner, C. S., 1989, "Sodium resonance fluorescence lidar applications in atmospheric science and astronomy," *Proc. IEEE* **77**, 408–418.
- Gardner, C. S., B. M. Welsh, and L. A. Thompson, 1990, "Design and performance analysis of adaptive optical telescopes using laser guide stars," *Proc. IEEE* **78**, 1721–1743.
- Gaskill, J. D., 1978, *Linear Systems, Fourier Transforms, and Optics* (Wiley, New York).
- Gavel, D. T., J. R. Morris, and R. G. Vernon, 1994, "Systematic design and analysis of laser-guide-star adaptive-optics systems for large telescopes," *J. Opt. Soc. Am. A* **11**, 914–924.
- Gendron, E., and P. Lena, 1994, "Astronomical adaptive optics. I. modal control optimization," *Astron. Astrophys.* **291**, 337–347.
- Gonglewski, J. D., D. G. Voelz, J. S. Fender, D. C. Dayton, B. K. Spielbusch, and R. E. Pierson, 1990, "First astronomical application of postdetection turbulence compensation: images of α Aurigae, ν Ursae Majoris, and α Geminorum using self-referenced speckle holography," *Appl. Opt.* **29**, 4527–4529.
- Gonsalves, R. A., 1982, "Phase retrieval and diversity in adaptive optics," *Opt. Eng.* **21**, 829–832.
- Gonzalez, R. C., and R. E. Woods, 1993, *Digital Image Processing* (Addison-Wesley, Reading, MA).
- Goodman, J. W., 1968, *Introduction to Fourier Optics* (McGraw-Hill, New York).
- Goodman, J. W., 1985, *Statistical Optics* (Wiley, New York).
- Goodman, J. W., and J. F. Belsher, 1977, "Photon limitations in imaging and image restoration," Contract RADC-TR-77-175, Rome Air Development Center, Griffiss AFB, NY.
- Greenwood, D. P., 1977, "Bandwidth specifications for adaptive optics systems," *J. Opt. Soc. Am.* **67**, 390–392.
- Greenwood, D. P., 1979, "Mutual coherence function of a wave front corrected by zonal adaptive optics," *J. Opt. Soc. Am.* **69**, 549–554.
- Greenwood, D. P., and D. L. Fried, 1976, "Power spectra requirements for wave-front-compensation systems," *J. Opt. Soc. Am.* **66**, 193–206.
- Gull, S. F., and G. J. Daniell, 1978, "Image reconstruction from incomplete and noisy data," *Nature* **272**, 686–690.
- Halevi, P., 1983, "Bimorph piezoelectric flexible mirror: graphical solution and comparison with experiment," *J. Opt. Soc. Am. A* **73**, 110–113.
- Haniff, C. A., J. E. Baldwin, P. J. Warner, and T. R. Scott, 1994, "Atmospheric phase fluctuation measurement: interferometric results from the wht and coast telescopes," in *Amplitude and Spatial Interferometry II*, edited by J. Breckinridge (SPIE, Bellingham, WA), Proceedings of SPIE Vol. 2200, pp. 407–417.
- Happer, W., G. MacDonald, C. Max, and F. J. Dyson, 1994, "Atmospheric-turbulence compensation by resonant optical backscattering from the sodium layer in the upper atmosphere," *J. Opt. Soc. Am. A* **11**, 263–275.
- Hardy, J. W., 1978, "Active optics: a new technology for the control of light," *Proc. IEEE* **66**, 651–697.
- Hardy, J. W., and A. J. MacGovern, 1987, "Shearing interferometry: a flexible technique for wavefront measurement," in *Interferometric Metrology*, edited by N. A. Massey (SPIE, Bellingham, WA), Proceedings of SPIE Vol. 816, pp. 180–195.
- Harrington, P. M., and B. M. Welsh, 1994, "A frequency domain analysis of an adaptive optical system's temporal response," *Opt. Eng.* **33**, 2336–2342.
- Heidbreder, G. R., 1967, "Image degradation with random wavefront tilt compensation," *IEEE Trans. Antennas Propag.* **15**, 90–98.
- Herrmann, J., 1981, "Cross coupling and aliasing in modal wave-front estimation," *J. Opt. Soc. Am.* **71**, 989–992.
- Herrmann, J., 1992, "Phase variance and Strehl ratio in adaptive optics," *J. Opt. Soc. Am. A* **9**, 2257–2258.
- Horwitz, B. A., 1990, "Multiplex techniques for real-time shearing interferometry," *Opt. Eng.* **29**, 1223–1232.
- Hudgin, R. H., 1977a, "Wave front compensation error due to finite corrector-element size," *J. Opt. Soc. Am.* **67**, 393–395.
- Hudgin, R. H., 1977b, "Wave front reconstruction for compensated imaging," *J. Opt. Soc. Am.* **67**, 375–377.

- Hufnagel, R. E., 1974, "Variations of atmospheric turbulence," in *Digest of Technical Papers, Topical Meeting on Optical Propagation through Turbulence* (Optical Society of America, Washington, DC).
- Hulburd, B., and D. Sandler, 1990, "Segmented mirrors for atmospheric compensation," *Opt. Eng.* **29**, 1186–1190.
- Idell, P. S., and A. Webster, 1992, "Resolution limits for coherent optical imaging: signal-to-noise analysis in the spatial-frequency domain," *J. Opt. Soc. Am. A* **9**, 43–56.
- Ishimaru, A., 1978, *Wave Propagation and Scattering in Random Media* (Academic, New York), Vol. 2.
- Jefferies, S. M., and J. C. Christou, 1993, "Restoration of astronomical images by iterative blind deconvolution," *Astrophys. J.* **415**, 862–874.
- Johnston, D. C., and B. M. Welsh, 1992, "Estimating the contribution of different parts of the atmosphere to optical wave-front aberration," *Comput. Electr. Eng.* **18**, 467–484.
- Johnston, D. C., and B. M. Welsh, 1994, "Analysis of multi-conjugate adaptive optics," *J. Opt. Soc. Am. A* **11**, 394–408.
- Kane, T. J., B. M. Welsh, C. S. Gardner, and L. A. Thompson, 1989, "Wave front detector optimization for laser guided adaptive telescopes," in *Active Telescope Systems*, edited by F. Roddier (SPIE, Bellingham, WA), Proceedings of SPIE Vol. 1114, pp. 160–171.
- Karr, T. J., 1991, "Temporal response of atmospheric turbulence compensation," *Appl. Opt.* **30**, 363–364.
- Kingston, R. H., 1978, *Detection of Optical and Infrared Radiation* (Springer, Berlin).
- Knox, K. T., 1976, "Image retrieval from astronomical speckle patterns," *J. Opt. Soc. Am.* **66**, 1236–1239.
- Knox, K. T., and B. J. Thompson, 1974, "Recovery of images from atmospherically degraded short exposure images," *Astrophys. J.* **193**, L45–L48.
- Kokorowski, S. A., 1979, "Analysis of adaptive optical elements made from piezoelectric bimorphs," *J. Opt. Soc. Am.* **69**, 181–187.
- Kolmogorov, A. N., 1961, "The local structure of turbulence in incompressible viscous fluids for very large Reynolds' numbers," in *Turbulence, Classic Papers on Statistical Theory*, edited by S. K. Friedlander and L. Topper (Wiley-Interscience, New York), pp. 151–155.
- Korff, D., 1973, "Analysis of a method for obtaining near-diffraction-limited information in the presence of atmospheric turbulence," *J. Opt. Soc. Am.* **63**, 971–980.
- Labeyrie, A., 1970, "Attainment of diffraction limited resolution in large telescopes by Fourier analyzing speckle patterns in star images," *Astron. Astrophys.* **6**, 85.
- Labeyrie, A., 1976, "High-resolution techniques in optical astronomy," in *Progress in Optics*, edited by E. Wolf (North-Holland, Amsterdam), Vol. 14.
- Labeyrie, A., 1978, "Stellar interferometry methods," *Annu. Rev. Astron. Astrophys.* **16**, 77–102.
- Lane, R. G., 1992, "Blind deconvolution of speckled images," *J. Opt. Soc. Am. A* **9**, 1508–1514.
- Lawrence, T. W., D. M. Goodman, E. M. Johansson, and J. P. Fitch, 1992, "Speckle imaging of satellites at the U.S. Air Force Maui optical station," *Appl. Opt.* **31**, 6307–6321.
- Lee, R. W., and J. C. Harp, 1969, "Weak scattering in random media, with applications to remote probing," *Proc. IEEE* **57**, 375–406.
- Lohmann, A. W., G. Weigelt, and B. Wirtzner, 1983, "Speckle masking in astronomy: triple correlation theory and applications," *Appl. Opt.* **22**, 4028–4037.
- Lucy, L. B., 1974, "An iterative technique for the rectification of observed distributions," *Astron. J.* **79**, 745–754.
- Lutomirski, R. F., and R. G. Buser, 1973, "Mutual coherence function of a finite optical beam and application to coherent detection," *Appl. Opt.* **12**, 2153–2160.
- Mandel, L., 1958, "Fluctuations of photon beams: the distribution of the photo-electrons," *Proc. Phys. Soc.* **74**, 233–243.
- Matson, C. L., 1991, "Weighted-least-squares phase reconstruction from the bispectrum," *J. Opt. Soc. Am. A* **8**, 1905–1913.
- Matson, C. L., I. A. DeLarue, T. M. Gray, and I. E. Drunzer, 1992, "Optimal Fourier spectrum estimation from the bispectrum," *Comput. Electr. Eng.* **18**, 485–497.
- McCullough, P. R., R. Q. Fugate, J. C. Christou, B. L. Ellerbroek, C. H. Higgins, J. M. Spinhirne, R. A. Cleis, and J. F. Moroney, 1995, "Photoevaporating stellar envelopes observed with Rayleigh beacon adaptive optics," *Astrophys. J.* **438**, 394–403.
- Melsa, J. L., and D. L. Cohn, 1978, *Decision and Estimation Theory* (McGraw-Hill, New York).
- Meng, J., G. J. M. Aitken, E. K. Hege, and J. S. Morgan, 1990, "Triple-correlation subplane reconstruction of photon-address images," *J. Opt. Soc. Am. A* **7**, 1243–1250.
- Miller, M. G., 1977, "Noise considerations in stellar speckle interferometry," *J. Opt. Soc. Am.* **67**, 1176–1184.
- Moore, K. E., and G. N. Lawrence, 1990, "Zonal model of an adaptive mirror," *Appl. Opt.* **29**, 4622–4628.
- Nakajima, T., 1988, "Signal-to-noise ratio of the bispectral analysis of speckle interferometry," *J. Opt. Soc. Am. A* **5**, 1477–1491.
- Newton, I., 1952, "Optics," in *Great Books of the Western World*, edited by R. M. Hutchins (Encyclopaedia Britannica, Chicago), Vol. 34.
- Nisenson, P., and R. Barakat, 1987, "Partial atmospheric correction with adaptive optics," *J. Opt. Soc. Am. A* **4**, 2249–2253.
- Noll, R. J., 1976, "Zernike polynomials and atmospheric turbulence," *J. Opt. Soc. Am.* **66**, 207–211.
- Northcott, M. J., G. R. Ayers, and J. C. Dainty, 1988, "Algorithms for image reconstruction from photon-limited data using the triple correlation," *J. Opt. Soc. Am. A* **5**, 986–992.
- O'Donnell, K. A., and J. C. Dainty, 1980, "A space-time analysis of photon-limited stellar speckle interferometry," *J. Opt. Soc. Am.* **70**, 1354–1361.
- Papoulis, A., 1991, *Probability, Random Variables, and Stochastic Processes*, 3rd Ed. (McGraw-Hill, New York).
- Parenti, R. R., and R. J. Sasiela, 1994, "Laser-guide-star systems for astronomical applications," *J. Opt. Soc. Am. A* **11**, 288–309.
- Paxman, R. G., T. J. Schulz, and J. R. Fienup, 1992, "Joint estimation of object and aberrations by using phase diversity," *J. Opt. Soc. Am. A* **9**, 1072–1085.
- Petersen, D. P., and K. H. Cho, 1986, "Sampling and reconstruction of a turbulence-distorted wave front," *J. Opt. Soc. Am. A* **3**, 818–825.
- Primot, J., G. Rousset, and J. C. Fontanella, 1990, "Deconvolution from wave-front sensing: a new technique for compensating turbulence-degraded images," *J. Opt. Soc. Am. A* **7**, 1589–1608.
- Ribak, E. N., 1994, "Deformable mirrors," in *Adaptive Optics for Astronomy*, edited by D. Alloin and J.-M. Mariotti (Kluwer Academic, Boston), NATO Advanced Study Institute Series Vol. C423, pp. 149–161.

- Richardson, W. H., 1972, "Bayesian-based iterative method of image restoration," *J. Opt. Soc. Am.* **62**, 55–59.
- Rigaut, F., and E. Gendron, 1993, "Laser guide star adaptive optics: the tilt determination problem," *Astron. Astrophys.* **261**, 677–684.
- Roddier, C., and F. Roddier, 1973, "Correlation measurements on the complex amplitude of stellar plane wave perturbed by atmospheric turbulence," *J. Opt. Soc. Am.* **63**, 661–663.
- Roddier, F., 1981, "The effects of atmospheric turbulence in optical astronomy," *Progress in Optics*, edited by E. Wolf (North-Holland, New York), Vol. XIX, pp. 281–376.
- Roddier, F., 1988a, "Curvature sensing and compensation: a new concept in adaptive optics," *Appl. Opt.* **27**, 1223–1225.
- Roddier, F., 1988b, "Interferometric imaging in optical astronomy," *Phys. Rep.* **170**, 97–166.
- Roddier, F., 1991, "Wavefront curvature sensing and compensation methods in adaptive optics," in *Propagation Engineering: Fourth in a Series*, edited by L. R. Bissonnette and W. B. Miller (SPIE, Bellingham, WA), Vol. 1487, pp. 123–128.
- Roddier, F., 1994, "Adaptive optics at the University of Hawaii I: current performance at the telescope," in *Adaptive Optics in Astronomy*, edited by M. A. Ealey and F. Merkle (SPIE, Bellingham, WA), Proceedings of SPIE Vol. 2201, pp. 2–9.
- Roddier, F., M. Northcott, and J. E. Graves, 1991, "A simple low-order adaptive optics system for near-infrared applications," *Publ. Astron. Soc. Pac.* **103**, 131–149.
- Roddier, F., M. J. Northcott, J. E. Graves, and D. L. McKenna, 1993, "One-dimensional spectra of turbulence-induced Zernike aberrations: time-delay and isoplanicity error in partial adaptive compensation," *J. Opt. Soc. Am. A* **10**, 957–965.
- Roddier, F., C. Roddier, and N. Roddier, 1988, "Curvature sensing: a new wavefront sensing method," in *Statistical Optics*, edited by G. M. Morris (SPIE, Bellingham, WA), Proceedings of SPIE Vol. 976, pp. 203–209.
- Roddier, N., 1990, "Atmospheric wavefront simulation using Zernike polynomials," *Opt. Eng.* **29**, 1174–1180.
- Roggemann, M. C., 1991, "Limited degree-of-freedom adaptive optics and image reconstruction," *Appl. Opt.* **30**, 4227–4233.
- Roggemann, M. C., 1992, "Optical performance of fully and partially compensated adaptive optics systems using least-squares and minimum variance phase reconstruction," *Comput. Electr. Eng.* **18**, 451–466.
- Roggemann, M. C., E. L. Caudill, D. W. Tyler, M. J. Fox, M. A. V. Bokern, and C. L. Matson, 1994, "Compensated speckle imaging: theory and experimental results," *Appl. Opt.* **33**, 3099–3110.
- Roggemann, M. C., B. L. Ellerbroek, and T. A. Rhoadarmer, 1995, "Widening the effective field-of-view of adaptive optics telescopes using deconvolution from wavefront sensing: average and signal-to-noise ratio performance," *Appl. Opt.* **34**, 1432–1444.
- Roggemann, M. C., and C. L. Matson, 1992, "Power spectrum and Fourier phase spectrum estimation by using fully and partially compensating adaptive optics and bispectrum post-processing," *J. Opt. Soc. Am. A* **9**, 1525–1535.
- Roggemann, M. C., and J. A. Meinhardt, 1993, "Image reconstruction by means of wave-front sensor measurements in closed-loop adaptive-optics systems," *J. Opt. Soc. Am. A* **10**, 1996–2007.
- Roggemann, M. C., D. W. Tyler, and M. F. Bilmont, 1992, "Linear reconstruction of compensated images: theory and experimental results," *Appl. Opt.* **31**, 7429–7441.
- Roggemann, M. C., and B. M. Welsh, 1994, "Signal-to-noise ratio for astronomical imaging by deconvolution from wavefront sensing," *Appl. Opt.* **33**, 5400–5414.
- Roggemann, M. C., and B. M. Welsh, 1996, *Imaging through the Atmosphere* (CRC, Boca Raton, FL).
- Roggemann, M. C., B. M. Welsh, and J. Devey, 1994, "Biased estimators and object-spectrum estimation in the method of deconvolution from wavefront sensing," *Appl. Opt.* **33**, 5754–5763.
- Rousset, G., 1994, "Wavefront sensing," in *Adaptive Optics for Astronomy*, edited by D. Alloin and J.-M. Mariotti (Kluwer Academic, Boston), NATO Advanced Study Institute Series Vol. C423, pp. 115–137.
- Sandler, D., L. Cuellar, M. Lefebvre, T. Barrett, R. Arnold, P. Johnson, A. Rego, G. Smith, G. Taylor, and B. Spivey, 1994, "Shearing interferometry for laser-guide-star atmospheric correction at large d/r_o ," *J. Opt. Soc. Am. A* **11**, 858–873.
- Sasiela, R. J., 1994, "Wave-front correction by one or more synthetic beacons," *J. Opt. Soc. Am. A* **11**, 379–393.
- Sasiela, R. J., and J. G. Mooney, 1985, "An optical phase reconstructor based on using a multiplier-accumulator approach," in *Adaptive Optics*, edited by J. E. Ludman (SPIE, Bellingham, WA), Proceedings of SPIE Vol. 551, pp. 170–176.
- Schulz, T. J., 1993, "Multiframe blind deconvolution of astronomical images," *J. Opt. Soc. Am. A* **10**, 1064–1073.
- Schwartz, C., E. Ribak, and S. G. Lipson, 1994, "Bimorph adaptive mirrors and curvature sensing," *J. Opt. Soc. Am. A* **11**, 895–902.
- Sementilli, P. J., B. R. Hunt, and M. S. Nadar, 1993, "Analysis of the limit to superresolution in incoherent imaging," *J. Opt. Soc. Am. A* **10**, 2265–2276.
- Smithson, R. C., and M. L. Peri, 1989a, "Partial correction of astronomical images with active mirrors," *J. Opt. Soc. Am. A* **6**, 92–97.
- Smithson, R. C., *et al.*, 1988, "Quantitative simulation of image correction for astronomy with a segmented active mirror," *Appl. Opt.* **27**, 1615–1620.
- Southwell, W. H., 1980, "Wave-front estimation from wavefront slope measurements," *J. Opt. Soc. Am.* **70**, 998–1006.
- Steinhaus, E., and S. G. Lipson, 1979, "Bimorph piezoelectric flexible mirror," *J. Opt. Soc. Am.* **69**, 478–481.
- Tatarski, V. I., 1967, *Wave Propagation in a Turbulent Medium* (Dover, New York).
- Tatarskii, V. I., and V. U. Zavorotny, 1993, "Atmospheric turbulence and the resolution limits of large ground-based telescopes: comment," *J. Opt. Soc. Am. A* **10**, 2410–2414.
- Thompson, A. R., J. M. Moran, and J. G. W. Swenson, 1986, *Interferometry and synthesis in radio astronomy* (Wiley, New York).
- Thompson, L. A., 1994, "Adaptive optics in astronomy," *Phys. Today* **47** (12), 24–31.
- Troxel, S. E., B. M. Welsh, and M. C. Roggemann, 1994, "Off-axis optical transfer function calculations in an adaptive-optics system by means of a diffraction calculation for weak index fluctuations," *J. Opt. Soc. Am. A* **11**, 2100–2111.
- Troxel, S. E., B. M. Welsh, and M. C. Roggemann, 1995, "Anisoplanatism effects on signal-to-noise ratio performance of adaptive optical systems," *J. Opt. Soc. Am. A* **12**, 570–577.

- Tyler, D. W., and C. L. Matson, 1993, "Speckle imaging detector optimization and comparison," *Opt. Eng.* **32**, 864–869.
- Tyler, G. A., 1984, "Turbulence-induced adaptive-optics performance degradation: evaluation in the time domain," *J. Opt. Soc. Am. A* **1**, 251–262.
- Tyler, G. A., 1993, "Merging: a new method for tomography through random media," *J. Opt. Soc. Am. A* **10**, 409–425.
- Tyler, G. A., 1994a, "Bandwidth considerations for tracking through turbulence," *J. Opt. Soc. Am. A* **11**, 358–367.
- Tyler, G. A., 1994b, "Wave-front compensation for imaging with off-axis guide stars," *J. Opt. Soc. Am. A* **11**, 339–346.
- Tyler, G. A., and D. L. Fried, 1982, "Image position error associated with a quadrant detector," *J. Opt. Soc. Am.* **72**, 804–808.
- Tyson, R. K., 1991, *Principles of Adaptive Optics* (Academic, San Diego, CA).
- Tyson, R. K., and P. B. Ulrich, 1993, "Adaptive optics," in *The Infrared and Electro-Optical Systems Handbook*, edited by S. R. Robinson, Vol. 8 (SPIE, Bellingham, WA).
- Walker, J. G., 1978, "Optimum exposure time and filter bandwidth in speckle interferometry," in *High Angular Resolution Stellar Interferometry, Proceedings of Colloquium #50, International Astronomical Union* (University of Maryland, College Park, MD), Vol. 5, pp. 25-1 to 25-24.
- Wallner, E. P., 1983, "Optimal wave front correction using slope measurements," *J. Opt. Soc. Am.* **73**, 1771–1776.
- Wang, J. Y., and J. K. Markey, 1978, "Modal compensation of atmospheric turbulence phase distortion," *J. Opt. Soc. Am.* **68**, 78–87.
- Welsh, B. M., 1991, "Imaging performance analysis of adaptive telescopes using laser guide stars," *Appl. Opt.* **30**, 5021–5030.
- Welsh, B. M., 1992, "Effect of an adaptive optical system's temporal response on imaging performance," in *Atmospheric Propagation and Remote Sensing*, edited by A. Kohnle and W. B. Miller (SPIE, Bellingham, WA), Proceedings of SPIE Vol. 1688, pp. 536–547.
- Welsh, B. M., 1995, "Speckle imaging signal-to-noise performance as a function of frame integration time," *J. Opt. Soc. Am. A* **12**, 1364–1374.
- Welsh, B. M., B. L. Ellerbroek, M. C. Roggemann, and T. L. Pennington, 1995, "Fundamental performance limitations and comparison of the Hartmann and shearing interferometer wavefront sensors," *Appl. Opt.* **34**, 4186–4195.
- Welsh, B. M., and C. S. Gardner, 1989, "Performance analysis of adaptive optics systems using slope sensors," *J. Opt. Soc. Am. A* **6**, 1913–1923.
- Welsh, B. M., and C. S. Gardner, 1991, "Effects of turbulence induced anisoplanatism on the imaging performance of adaptive astronomical telescopes using laser guide stars," *J. Opt. Soc. Am. A* **8**, 69–80.
- Welsh, B. M., and R. N. V. Niederhausern, 1993, "Performance analysis of the self-referenced speckle holography image reconstruction technique," *Appl. Opt.* **32**, 5071–5078.
- Welsh, B. M., and M. C. Roggemann, 1994a, "Evaluating the performance of adaptive optical telescopes," in *Adaptive Optics for Astronomy*, edited by D. Alloin and J.-M. Mariotti (Kluwer Academic, Boston), *NATO Advanced Study Institute Series*, Vol. C423, p. 211–225.
- Welsh, B. M., and M. C. Roggemann, 1994b, "Signal-to-noise comparison of deconvolution from wave front sensing and speckle imaging," in *Image Reconstruction and Restoration*, edited by T. J. Schulz and D. L. Snyder (SPIE, Bellingham, WA), Proceedings of SPIE Vol. 2302, pp. 281–292.
- Wessely, H. W., and J. O. Bolstad, 1970, "Interferometric technique for measuring the spatial-correlation function of optical radiation fields," *J. Opt. Soc. Am.* **60**, 678–682.
- Wild, W. J., E. J. Kibblewhite, and R. Vuilleumier, 1995, "Sparse matrix wave-front estimators for adaptive-optics systems for large ground-based telescopes," *Opt. Lett.* **20**, 955–957.
- Winnick, K. A., 1986, "Cramer-Rao lower bounds on the performance of charge-coupled-device optical position estimators," *J. Opt. Soc. Am. A* **3**, 1809–1815.
- Witthoft, C., 1990, "Wavefront sensor noise reduction and dynamic range expansion by means of optical image intensification," *Opt. Eng.* **29**, 1233–1238.
- Wyant, J. C., 1974, "White light extended source shearing interferometer," *Appl. Opt.* **13**, 200–202.
- Wyant, J. C., 1975, "Use of an AC heterodyne lateral shear interferometer with real-time wavefront correction systems," *Appl. Opt.* **14**, 2622–2626.
- Young, A. T., 1974, "Seeing: Its cause and cure," *Astrophys. J.* **189**, 587–604.
- Yura, H. T., and M. T. Tavis, 1985, "Centroid anisoplanatism," *J. Opt. Soc. Am. A* **2**, 765–773.